



UNIVERSITAT DE
BARCELONA

Enhancing electrochemical performances of supercapacitors

Hemesh Avireddy

ADVERTIMENT. La consulta d'aquesta tesi queda condicionada a l'acceptació de les següents condicions d'ús: La difusió d'aquesta tesi per mitjà del servei TDX (www.tdx.cat) i a través del Dipòsit Digital de la UB (diposit.ub.edu) ha estat autoritzada pels titulars dels drets de propietat intel·lectual únicament per a usos privats emmarcats en activitats d'investigació i docència. No s'autoritza la seva reproducció amb finalitats de lucre ni la seva difusió i posada a disposició des d'un lloc aliè al servei TDX ni al Dipòsit Digital de la UB. No s'autoritza la presentació del seu contingut en una finestra o marc aliè a TDX o al Dipòsit Digital de la UB (framing). Aquesta reserva de drets afecta tant al resum de presentació de la tesi com als seus continguts. En la utilització o cita de parts de la tesi és obligat indicar el nom de la persona autora.

ADVERTENCIA. La consulta de esta tesis queda condicionada a la aceptación de las siguientes condiciones de uso: La difusión de esta tesis por medio del servicio TDR (www.tdx.cat) y a través del Repositorio Digital de la UB (diposit.ub.edu) ha sido autorizada por los titulares de los derechos de propiedad intelectual únicamente para usos privados enmarcados en actividades de investigación y docencia. No se autoriza su reproducción con finalidades de lucro ni su difusión y puesta a disposición desde un sitio ajeno al servicio TDR o al Repositorio Digital de la UB. No se autoriza la presentación de su contenido en una ventana o marco ajeno a TDR o al Repositorio Digital de la UB (framing). Esta reserva de derechos afecta tanto al resumen de presentación de la tesis como a sus contenidos. En la utilización o cita de partes de la tesis es obligado indicar el nombre de la persona autora.

WARNING. On having consulted this thesis you're accepting the following use conditions: Spreading this thesis by the TDX (www.tdx.cat) service and by the UB Digital Repository (diposit.ub.edu) has been authorized by the titular of the intellectual property rights only for private uses placed in investigation and teaching activities. Reproduction with lucrative aims is not authorized nor its spreading and availability from a site foreign to the TDX service or to the UB Digital Repository. Introducing its content in a window or frame foreign to the TDX service or to the UB Digital Repository is not authorized (framing). Those rights affect to the presentation summary of the thesis as well as to its contents. In the using or citation of parts of the thesis it's obliged to indicate the name of the author.

Tesi doctoral

Enhancing electrochemical performances of supercapacitors

Autor: Hemesh Avireddy

Directors: Prof. Dr. Joan Ramon
Morante Leonart i Dra. Cristina Flox



UNIVERSITAT DE
BARCELONA

Enhancing electrochemical performances of supercapacitors

Memoria presentada per optar al grau de doctor per la
Universitat de Barcelona

Programa de doctorat en
NANOCIÈNCIES

Autor: Hemesh AVIREDDY

Directors: Prof. Dr. Joan Ramon Morante
Leonart i Dra. Cristina Flox

Tutor: Prof. Dr. Joan Ramon Morante
Leonart

Lloc on s'ha dut a terme la tesi

Institut de Recerca en Energia de Catalunya (IREC)



UNIVERSITAT DE
BARCELONA

Outline

The work presented in this thesis is developed by the Ph.D. candidate Hemesh Avireddy at the Energy Storage and Harvesting group belonging to the Catalonia Institute for Energy Research (IREC) during the period of 2016-2019. This work was carried under the supervision of Prof. Joan Ramon Morante Leonart and Dr. Cristina Flox. This work also includes the investigation carried out during the visiting stay at Institut des Matériaux Jean Rouxel, Polytech Nantes (France) and at the A.J. Drexel Nanomaterials Institute (DNI) in Drexel University (USA) in the period of May-Jun (2017) and Feb-May (2018), respectively.

The thesis is focused on the knowledge development oriented and driven to the improvement of the electrochemical behavior of the supercapacitors. The thesis is divided into five chapters: **Chapter 1** introduces supercapacitor as an energy storage device with high power density but suffering from low values of energy density. This drawback limits them in the applications where both high power and energy density are necessary. Therefore, improving the energy density of supercapacitors is considered one of the general focus of this thesis. As technology of the supercapacitor is sub-divided into carbon-based electric double layer capacitor and pseudocapacitor. So, in this scenario, two main significant problems were identified in each of these sub fields and were tackled in this thesis:

(a) the supercapacitor performance limitations due to the condition of fast charging,

(b) the low cell voltage of pseudocapacitors in aqueous electrolytes in comparison to the use of other electrolytes.

For these problems *reasonable approaches were underscored to tackle them and specific objectives were detailed in chapter 1*, which were achieved in the subsequent chapters. *Chapter 2* briefly explains the equipment and characterization techniques taken into account for validating the investigation. Following this, *Chapter 3* deals with the first problem related to the supercapacitor performance limitations due to the condition of fast charging. To overcome these performance limitations, an original alternative proposed by us, the electrospinning is highlighted as a promising technique to design a metal-oxide embedded porous carbon nanofibers with a 3-D electrode architecture that contribute to reduce the electrode resistance increasing, at the same time, the associated capacitance value. The investigation *via* several materials and electrochemical characterization techniques indicate an essential role in the concentration of the metal-oxide precursor towards the electrochemical behavior of the electrodes. This correlation could be useful to design better electrodes for supercapacitor, functioning with better energy and power density capabilities. In *chapter 4*, the problem related to the low cell voltages in aqueous pseudocapacitor is tackled by exploring the improvement based on the electrode material properties instead the more standard carbon based materials. So, new materials from the family of MXenes are introduced, to achieve higher cell voltages. Under this frame, a new 2-D MXene based on Molybdenum Vanadium Carbide is proposed and its electrochemical characteristics have been investigated. According to its characteristics, its coupling with 2-D Titanium Carbide MXene exhibits a higher voltage in an all-MXene pseudocapacitive cell.

Chapter 5 also deals the low cell voltage problem but applying another approach based on the electrolyte modification. The proposed approach is based on the use of water-based super-concentrated salt solutions which are promising electrolytes to contribute to widen the cell voltage of aqueous pseudocapacitors. Likewise, besides this, it is also proposed that the coupling of 2-D Titanium Carbide MXene with the tunnel structures of Manganese Oxide using this super-concentrated electrolyte water in salt allows achieving a high voltage aqueous pseudocapacitive energy storage device. Furthermore, the strategy for cell assembly and its electrochemical performances are also detailed in this chapter.

In the above-mentioned chapters, the conclusion of the investigation presented in the chapter is detailed in the end. Moreover, the overall thesis closes with the general conclusion of this thesis and as well as with the further work related to it.

Abstract

Electrochemical energy storage devices like supercapacitors are classified as high power devices, as they deliver energy in a short interval of time. Because of this property, supercapacitors are widely used for application which requires burst mode power delivery. Cranes, cars, trains, hand drillers, and elevators are some of the examples of these applications. However, the energy densities in supercapacitors are nearly an order magnitude lower than batteries. This limits the use of supercapacitors in the applications where high energy densities are desirable along with high power. Solving this problem and knowledge development orientation is the general focus of this thesis. This thesis highlights that energy is correlated with the capacitance and voltage of a supercapacitor. Therefore, improving the electrochemical performances in terms of increasing the values of capacitance and/or extending the voltage is a favorable route to improve the energy density of supercapacitors. The introduction of this thesis highlights the technology of supercapacitors into carbon-based electric double layer capacitors and pseudocapacitors. In which, the carbon-based supercapacitors suffer from low values of capacitance at the condition of fast charging. To overcome these performance limitations, an original alternative proposed, the electrospinning is highlighted as a promising technique to design a metal-oxide embedded porous carbon nanofiber with a 3-D electrode architecture that contributes to reducing the electrode resistance increasing, at the same time, the associated capacitance value. The investigation via several materials and electrochemical characterization techniques indicate an essential role in the concentration of the metal

oxide precursor towards the electrochemical behavior of the electrodes. This correlation could be useful to design better electrodes for supercapacitor, functioning with better energy and power density capabilities.

Whereas, in the case of the water-based pseudocapacitors, it is shown that they suffer from low voltages. Two strategies were used to overcome this issue.

- (i) the problem related to the low cell voltages in aqueous pseudocapacitor is tackled by exploring the improvement based on the electrode material properties instead of the more standard carbon-based materials. So, new materials from the family of MXenes are introduced, to achieve higher cell voltages. Under this frame, a new 2-D MXene based on Molybdenum Vanadium Carbide is proposed and its electrochemical characteristics have been investigated. According to its characteristics, its coupling with 2-D Titanium Carbide MXene exhibits a higher voltage in an all-MXene pseudocapacitive cell. The investigation reveals that the charge storage in 2-D molybdenum vanadium carbide MXene has the dependence on the type of electrolyte cations. For the case in point, small size monovalent cations, such as lithium and sodium ions, demonstrate lower hindrance to the charge storage, while large size monovalent potassium ions and bivalent magnesium ions suffer from hindrance effect, causing them to have lower charge storage than lithium and sodium ions. Therefore, the selection of appropriate electrolyte ions especially in the case of MXene based materials appears to be important, which is here found to be with the protonic and sodium ion based electrolytes. Moreover, using

these electrolytes to couple 2-D molybdenum vanadium carbide with other MXenes, like titanium carbide, has allowed for us to enable a reliable full MXenes based pseudocapacitor with high volumetric capacitances.

- (ii) the proposed approach is based on the use of water-based super-concentrated salt solutions which are promising electrolytes to contribute to widening the cell voltage of aqueous pseudocapacitors. Likewise, besides this, it is also proposed that the coupling of 2-D Titanium Carbide MXene with the tunnel structures of Manganese Oxide using this super-concentrated electrolyte water in salt can enable a high voltage aqueous pseudocapacitive energy storage device. The investigation using this approach reveals that the concentration of the salt electrolyte plays a significant role in the values of charge storage in 2-D titanium carbides. Although an extremely high concentration of salt electrolytes widens the potential window, the electrolyte ions in such high concentration face difficulty to insert within the 2-D layers of titanium carbide MXene. On the contrary, the use of low concentrated salt solutions is not recommended, as they provide narrow potential windows. Consequently, during the cell assembling using super-concentrated electrolytes, a moderate concentration of salt electrolyte needs to be taken into attention. On this way, both, wider potential window and high charge storage, can be achieved with pseudocapacitive materials like 2-D titanium carbides MXenes. The crystallographic tunnel size of manganese oxide plays a vital role in the charge storage. For instance, tunnel structures, both smaller and larger than the size of the electrolyte ions store fewer charges. As both of these tunnel phases of

manganese oxide face difficulty for the insertion of the electrolyte ions. Therefore, manganese oxide with adequate tunnel size needs to be taken into account. Besides this, it is also essential to consider the electronic conductivity of the manganese oxide phase, as high electronic conductivity allows it to store more charges during the condition of fast charging. In regards of the cell assembly, after considering the above-mentioned understanding the practice of applying the voltage-hold test to determine the realistic cell voltage is helpful, as the cell assembled with such realistic voltages permits the cell to have long cycle life.

Besides these understanding, remarkable performances were witnesses with the technologies developed in this thesis. For example, the carbon-based electric double layer supercapacitor shows faster responses than the existing carbon-based supercapacitors, (ii) the pseudocapacitors shows high volumetric capacitances ($> 35 \text{ F cm}^{-3}$) than carbon-based supercapacitors. Besides this, pseudocapacitors also exhibit higher cells voltages than the existing pseudocapacitors. The pseudocapacitor cells developed in this exhibits high electrochemical stability ($> 95 \%$) over thousands of cycles. Furthermore, the pseudocapacitor is more favorable than EDLCs in applications where cell volume is critical, as pseudocapacitors provide lower cell volume and slower self-discharges than EDLCs. In addition to all these, the thesis also outlines several important methodologies, such as the selection of the electrode, electrode processing and the cell assembly towards the development of the supercapacitor technology is a powerful tool for the community.

Resumen

Los dispositivos de almacenamiento de energía electroquímicos, como los supercapacitores, se clasifican como dispositivos de alta potencia, ya que suministran energía en un corto intervalo de tiempo. Debido a esta propiedad, los supercapacitores se utilizan ampliamente para aplicaciones que requieren la entrega de un alto nivel de energía durante un corto intervalo temporal tal como sucede por ejemplo en grúas, carros, trenes, perforadoras o ascensores que son algunos de los ejemplos de estas aplicaciones. Sin embargo, las densidades de energía en los supercapacitores son casi una magnitud de orden inferior a las baterías. Esto limita el uso de supercapacitores en las aplicaciones donde son deseables tanto altas densidades de potencia como de energía que equivale a ser capaz de mantener la potencia facilitada durante más tiempo. En este contexto, el enfoque general de esta tesis es contribuir a resolver este problema contribuyendo con diversas propuestas y alternativas a la vez que se implementa un mejor conocimiento sobre los materiales y mecanismos involucrados en estos dispositivos electroquímicos.

Dado que la energía está correlacionada con la capacidad y el voltaje de un supercapacitador, el objetivo principal de esta tesis ha sido tanto incrementar la capacidad como aumentar el voltaje.

Asimismo hay que destacar que los supercapacitores producidos en base a la actual tecnología de carbono sufren además de bajos valores de capacitancia en condiciones de carga rápida a causa de sus constantes de tiempo de respuesta. Para superar estas limitaciones, una se ha propuesto una alternativa, basada en la fabricación de nanofibras de carbono por

electrospinning permitiendo esta técnica incorporar metales o sus óxidos obteniéndose con el proceso y metodología propuesta una arquitectura de electrodos 3-D que contribuye a reducir el valor de la resistencia del electrodo al mismo tiempo que ello permite incrementar la densidad de poros incrementando su distribución lo que implica un considerable aumento del valor de la capacidad. La investigación a través de varios materiales y técnicas de caracterización electroquímica indican un papel esencial en la concentración del precursor metálico hacia el comportamiento electroquímico de los electrodos. Esta correlación es útil para diseñar mejores electrodos para supercapacitores, para obtener mejores capacidades de densidad de energía y potencia.

Para mejorar el rango de voltajes existentes en las supercapacidades que utilizan electrolitos de base acuosa se han utilizado dos estrategias para superar este problema:

- (i) Por una parte se ha explorado la mejora basada en mejorar las propiedades del material del electrodo en lugar de utilizar los materiales más estándar basados en carbono. Así, se han empleado nuevos materiales de la familia de MXenes, para lograr voltajes de celda más altos debido a sus propiedades electroquímicas., Así se ha propuesto un nuevo MXene 2-D basado en carburo de vanadio y molibdeno y se han investigado con detalle sus características electroquímicas. De acuerdo con sus características, su acoplamiento con carburo de titanio 2-D MXene nos ha permitido obtener un voltaje más alto en una celda pseudocapacitiva con MXene en ambos electrodos. La investigación revela que el almacenamiento de carga en carburo de vanadio-vanadio 2-D MXene depende del tipo de cationes de electrólito. Para el caso en

cuestión, los cationes monovalentes de tamaño pequeño, como los iones de litio y sodio, muestran un menor dificultad para el almacenamiento de carga, mientras que los iones de potasio monovalentes de tamaño grande y los iones de magnesio bivalentes tienen un mayor efecto de impedimento, lo que hace que tengan un almacenamiento de carga más bajo que el litio y los iones de sodio. Por lo tanto, la selección de los iones de electrólitos apropiados, especialmente en el caso de los materiales basados en MXene, parece ser importante. Además, el uso de estos electrolitos para combinar el carburo de vanadio y vanadio 2-D con otros MXenes, como el carburo de titanio, nos ha permitido habilitar un pseudocapacitador basado en MXenes completo de alta fiabilidad con altas capacidades volumétricas.

- (ii) Por otro lado, el enfoque propuesto se ha basado en el uso de soluciones salinas superconcentradas que son prometedores electrolitos para contribuir a ampliar el voltaje celular de los pseudocapacitores de base acuosa. Del mismo modo, además de esto, también se ha propuesto combinar el carburo de titanio 2-D MXene con las estructuras del túnel de óxido de manganeso usando como electrolito esta solución superconcentrada para obtener un dispositivo de almacenamiento de energía pseudocapacitivo de base acuosa con alto voltaje. La investigación nos ha permitido concluir que la concentración del electrolito salino desempeña un papel importante en los valores de almacenamiento de carga en carburos de titanio 2-D. Aunque una concentración extremadamente alta de estos electrolitos salinos ensancha la ventana potencial, los iones de electrólitos en tal concentración alta tienen dificultades para insertarse dentro de las capas 2D del carburo de titanio MXene. Por el contrario, el uso de soluciones de sal en baja concentración tampoco es recomendable, ya que proporcionan ventanas de potencial

más pequeñas. En consecuencia, durante el ensamblaje de la celda utilizando electrolitos superconcentrados, se debe tener en cuenta una concentración moderada de electrolito salino. De esta manera, tanto la ventana de potencial más amplio como el almacenamiento de alta carga se pueden lograr con materiales pseudocapacitivos como los carburos de titanio 2-D MXenes. Por su parte, las características a escala manométrica del óxido de manganeso desempeña un papel vital en el almacenamiento de la carga. Estas estructuras, tanto más pequeñas como más grandes que el tamaño de los iones electrolíticos almacenan menos cargado que tienen dificultades para la inserción de los iones del electrolitos. Por tanto, se debe tener en cuenta en la síntesis del material sus características nanométricas para asegurar la adecuada inserción. Además, también es esencial considerar la conductividad electrónica de la fase de óxido de manganeso, ya que al tener una alta conductividad electrónica tendrá una más grande capacidad de almacenar más cargas durante la condición de carga rápida.

Finalmente, reseñar que los trabajos desarrollados han permitido implementar supercapacitors eléctricos de doble capa basado en carbono con respuestas más rápidas que los supercapacitores basados en carbono existentes. Asimismo los pseudocapacitores fabricados muestran altas capacitancias volumétricas ($> 35 \text{ F cm}^{-3}$) exhibiendo voltajes de células más altos que los pseudocapacitores existentes. Además, las células pseudocapacitoras desarrolladas tienen una alta estabilidad electroquímica ($> 95\%$) durante miles de ciclos.

Chapter 1:

Introduction to Electrochemical Supercapacitors

1.1. A brief history of supercapacitors

Origin of the electrochemical supercapacitor dates back to the year of 1853 when Helmholtz discovered the concept of *double layer* electrical charging (Helmholtz, 1853). Around a century later (1954-66), a paradigm shift occurred with the new inventions. In 1954, H. I. Becker applied the concept of double layer charging with high surface area carbons (U.S. Patent 2,800,616, from General Electric (GE)). But, the field of supercapacitors become exciting when Robert Rightmire used the concept of Becker's work to invent the first device based on electrochemical supercapacitor (1966, U.S. Patent 3,288,641, from Standard Oil Co. of Ohio (SOHIO)). This device showed capacitance with a six order of magnitude higher than conventional ceramic capacitors. However, no commercial applications were seen in the market until SOHIO licensed its technology to Nippon Electric Corp. (NEC) in the year 1977. Due to this license agreement, NEC was allowed to apply supercapacitors in several commercial products. Back-up power devices for metal-oxide-semiconductor (CMOS) computer memories and volatile clock chips were some of the applications. During the late 1980s, Research Institute (PRI) developed an Ultracapacitor, which was based on ruthenium/tantalum oxide. Investigators consider this as the beginning of a new era in the field of supercapacitors and started to term this rivalry as competition towards non-carbon based supercapacitors or *pseudo* or *pseudocapacitors*. Nevertheless, the high cost of noble metals like ruthenium limited the use of PRI Ultracapacitor to military applications. In 1989, another paradigm shift occurred when Maxwell Technologies Inc. contracted U.S. Department of Energy to developed supercapacitors for braking and releasing application in electric and hybrid vehicles. Since then, numerous leading companies joined the competition to develop micro to grid-scale devices. Some examples of these companies are ELTON (Russia), Nesscap (Korea), Nippon Chemicon (Japan) and CAP-XX (Australia), Loxus (U.S.),

Murata (Japan) and LS Mtron (Korea). Besides this, recently, several new ventures like Skeletontech (Germany), C2C New Cap (Portugal) and NAWA technologies (France) also joined the battle to develop better supercapacitors.

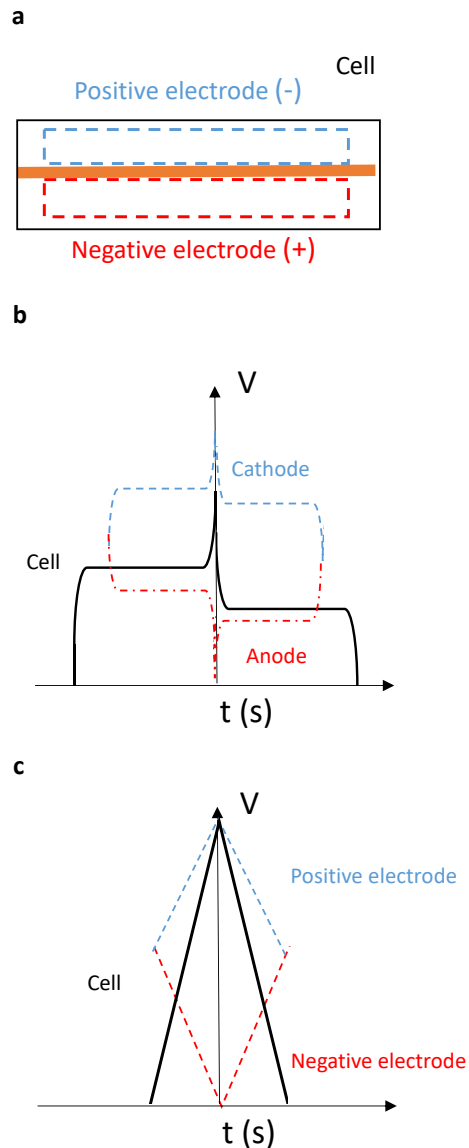


Figure 1.1. Schematic illustration showing (a) a typical configuration of an electrochemical supercapacitor cell, galvanostatic charge and discharge curve of a (b) battery and (c) supercapacitor.

1.2. Supercapacitor vs Battery: Basic differences

An electrochemical cell of a supercapacitor is usually composed of a positive and negative electrode, which is either separated by an ion-permeable membrane or by a liquid electrolyte (*figure 1.1a*). The origin of rapid charging in an electrochemical supercapacitor is a result of the quick physical and chemical interactions between the electrolyte ions and the electrode materials. Unlike battery materials (*figure 1.1b*), capacitive materials show a linear increase of voltage during a constant applied current (*figure 1.1c*). Because of which, their capacitance, C in Farad (F), is a constant value between charge and applied driving force (in here, voltage) (Simon, Gogotsi and Dunn, 2014). This can be given by Eq. (1.1)

$$C = \frac{\Delta Q}{\Delta U} \quad (1.1)$$

in which, ΔQ is stored charge when ΔV is the applied voltage. Whereas, in batteries, the charge is based on Faradaic reactions, which is usually accounted as Coulomb (c) or with a unit as Ah.

General problem in the field:

Both batteries and supercapacitors play an important role in our daily life. They are usually either used as macro-or micro-size devices depending upon their scale of the demand. Grid and mobility scale storage are examples for the macro-size devices, whereas electronic circuit for micro-size devices. Although batteries based on lithium-ion chemistries provide energy densities $>100 \text{ Wh kg}^{-1}$ (Lukatskaya, Dunn and Gogotsi, 2016), batteries suffer from resistive losses, sluggish ion transports, and dendrite formations. These are some of the factors which makes the batteries to suffer from low power density, and short cycle life (< 1000 cycles). Whereas, supercapacitor store charges at a rapid rate with extensive cycle life (>1000 cycles). Because of which, the supercapacitor is used

in applications which require burst mode power delivery (Gogotsi and Simon, 2011; Lukatskaya, Dunn and Gogotsi, 2016). Cars, cranes, trains and elevators are some of the examples of these applications. **Figure 1.2** shows the Ragone plot of some commercially available supercapacitors. The data in this figure indicates that the energy densities in the supercapacitors are in between 1 and 15 Wh kg⁻¹. When compared to energy densities of lithium-ion based batteries (>100 Wh kg⁻¹), the energy density in supercapacitors is low. This limitation in supercapacitors restraint them in applications where high energy densities are desirable, along with high power ratings. Generally, the energy, E in a supercapacitor is represented as (Laheäär *et al.*, 2015):

$$E = \frac{1}{2} CV^2, \quad (1.2)$$

where C is the capacitance (F) and V is the voltage. Considering the Eq. (1.2), the energy of a supercapacitor can be improved by increasing the capacitance and extending its nominal voltages. Therefore, intensive research and development are being carried out in this direction.

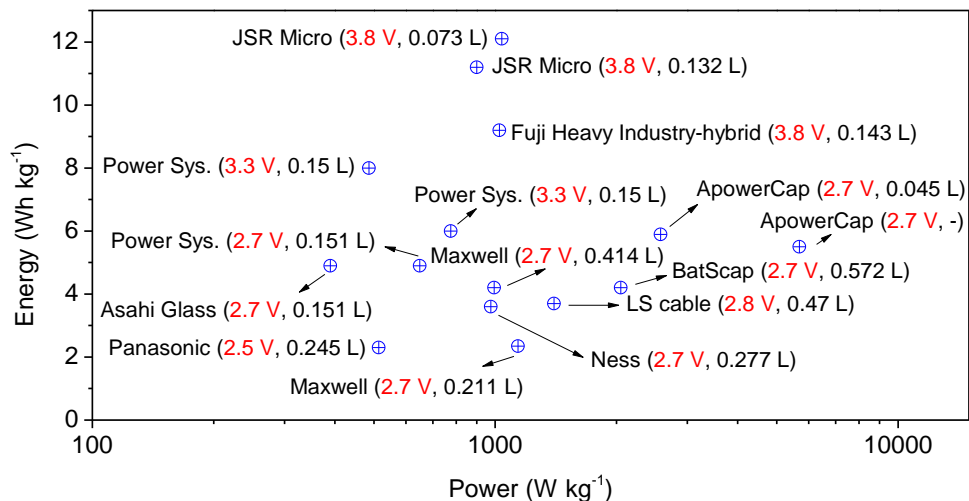


Figure 1. 2. Ragone plot of commercially available supercapacitor devices, figure plotted from the data shown in the reference of (Conte, 2010)

1.3. Classification of supercapacitors

As, an origin of the capacitive behavior in supercapacitors is influenced by the electrode material used (Lukatskaya, Dunn and Gogotsi, 2016; Brousse *et al.*, 2017), supercapacitors are generally classified into (i) Electric double layer capacitors (EDLCs) and (ii) Pseudocapacitors.

1.3.1 Carbon-based Electric double layer capacitors:

Carbon-based EDCL store charges by the physical adsorption and desorption of electrolyte ions in the carbon electrode. In this case, charge storage can be indicated by Helmholtz's double layer charging models (Helmholtz, 1853), as shown by Eq. (1.2) (Salanne *et al.*, 2016):

$$C = \frac{\epsilon_r \epsilon_0 A}{d} \quad (1.3).$$

Where ϵ_0 is the relative permittivity of the electrolyte, ϵ_r is the permittivity of vacuum, A is the effective surface area of the electrode materials and d is the effective thickness of the double layer (also known as *Debye length*). Helmholtz's double layer model indicates that capacitance can be increased by tuning the material to its high effective surface area. Therefore, extensive strategies were carried in fine-tuning the carbon material in terms of surface functionalities, sp^2 hybridization, pores size and volume and as well as its orientation (Béguin *et al.*, 2014). For example, the specific surface area of carbon materials like graphite is increased from $20 \text{ m}^2 \text{ g}^{-1}$ to $> 1,500 \text{ m}^2 \text{ g}^{-1}$ by exfoliating them into layer carbon sheets, like Graphene (Gogotsi and Simon, 2011). Such an increase in the effective surface area provides high accessibility to the surface sites, which results in capacitance rise from $< 15 \text{ F g}^{-1}$ to $> 200 \text{ F g}^{-1}$. Besides increasing the effective surface area, Eq. (1.3) also indicates that the Debye length can be also narrowed to raise the capacitance. For example, removal of the metal element in metal carbides, like Titanium or Silicon

carbide, results in sub-nanometer carbon pores (pores < 1 nm) or pores size nearly to the size of electrolyte ions (Largeot *et al.*, 2008; Jäckel *et al.*, 2016). This narrow pore size makes the Debye length to decrease ($\sim 5 - 10$ Å) (Salanne *et al.*, 2016) and escalates the value of capacitance up to a value of 140 Fg^{-1} (Largeot *et al.*, 2008). Such values of capacitance were previously lower than 90 Fg^{-1} in porous activated carbon materials like Yp-50 with pores sizes $> \sim 2$ nm (Merlet *et al.*, 2012). Nevertheless, (Salanne *et al.*, 2016) clarifies that the Helmholtz's model of double layer charging is limited in understanding the role of capacitance and its charging dynamics, as it fails to quantify the interface effect of many porous carbons. Because, most porous carbon materials show highly disordered properties. Besides this, as indicated by (Forse *et al.*, 2016, 2017), theories like Gouy-Chapman-Stern which predicts the decay of ionic charge distribution along with the applied potential, also fails to explain the thermodynamics and interfacial structural effect under the dynamic conditions.

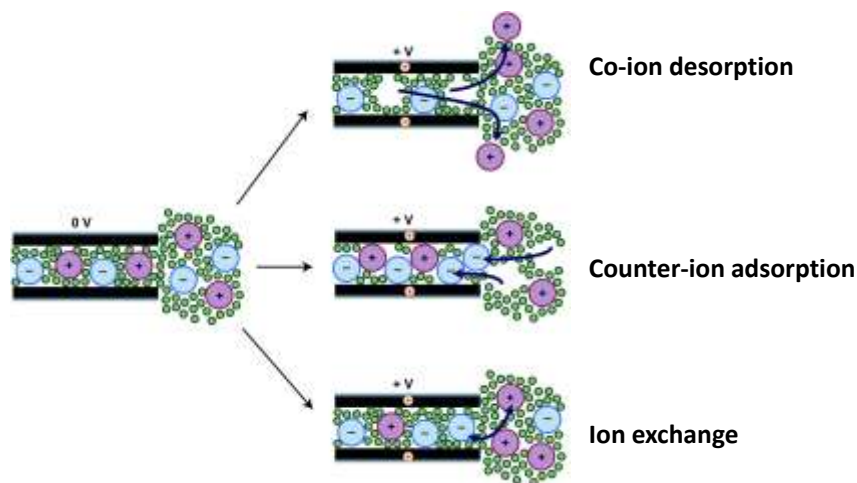


Figure 1. 3. Different ion recombination mechanisms. Figure reproduced from (Griffin, Forse, Wang, Trease, P. L. Taberna, et al., 2014) with permission of FARADAY DIVISION, ROYAL CHEMICAL SOCIETY). Schematic showing ion recombination (left) at null potential and (right) their recombination mechanisms

In recent years, several spectroscopy techniques offered a new understanding in the mechanism of charge storage. Some of them are in-situ EQCM (Levi *et al.*, 2010; Wu *et al.*, 2017), NMR (Forse *et al.*, 2017), IR spectroscopy (Richey *et al.*, 2014), and other scattering methods (Prehal *et al.*, 2015), and as well as MD simulations (Kondrat and Kornyshev, 2013; Merlet *et al.*, 2013; Kondrat *et al.*, 2014). With the new understanding (Griffin, Forse, Wang, Trease, P. L. Taberna, *et al.*, 2014), it is considered that the carbon-based EDLCs store charges at the interface, which is present between the liquid electrolyte solution and the solid porous carbon electrode. This boundary is known as Fluid-Solid Interface (FSI). In this understanding, the capacitive storage is fundamentally influenced by the mode of interaction between the carbon and electrolyte ions at the FSI. In the view of several authors (Griffin, Forse, Wang, Trease, P.-L. Taberna, *et al.*, 2014; Forse *et al.*, 2016; Kondrat *et al.*, 2016), when a cell is assembled with porous carbon materials, which is a condition of zero or null potential (0 V), as shown by **Figure 1.3**, the carbon pore may be either filled or empty with the electrolyte ions. If the ions are filled, the time frame of the ion filling occurs at ~ 1 ns (Pean *et al.*, 2015). And, when positive or negative polarization of potentials are applied, the surface of the carbon gets electrically charged. Due to this charged surface, the population of electrolyte ions in the pore recombines with the ions of the bulk liquid electrolyte. Such recombination occurs within a short time (< 4 ns) (Pean *et al.*, 2015), in order to counter-balance the electronic charges of the carbon surface. This recombination of ions has been identified to occur through three possible mechanisms (i) Counter-ion adsorption, where insertions of new oppositely charged ions occur inside the carbon pore (ii) Ion-exchange, where swapping of ions occurs and (iii) Co-ion desorption, expelling of same charge ions without no counter-ion

adsorption. **Table 1.1.**, summaries the charging mechanisms observed so far during the dynamic conditions.

Carbon material	Salt (Electrolyte media)	Mechanism in positive electrode	Mechanism in negative electrode
YP-80 F (Prehal <i>et al.</i> , 2015)	1 M KCl (aq.) 1 M CsCl (aq.) 1 M NaCl (aq.)	Ion-exchange	Ion-exchange
YP-17 D (Levi <i>et al.</i> , 2010)	0.1 M NEt ₄ -BF ₄ (ACN) 0.2 0.1 M NOC ₄ -BF ₄ (ACN) 0.3 (ACN)	Ion-exchange (<i>low voltages</i>) Counter-ion adsorption (<i>high voltages</i>)	Ion-exchange (<i>low voltages</i>) Counter-ion adsorption (<i>high voltages</i>) Ion-exchange (in wider voltages)
CDC (Wu <i>et al.</i> , 2017)	1.5 M EMI-TFSI (ACN) EMI-TFSI (pure IL)	Ion-exchange (<i>low voltages</i>) Counter-ion adsorption (<i>high voltages</i>)	Counter-ion adsorption
CNFs (Richey <i>et al.</i> , 2014)	EMI-TFSI (pure IL)	Counter-ion adsorption	<i>No data available</i>
CNFs activated (Richey <i>et al.</i> , 2014)	EMI-TFSI (pure IL)	Ion-exchange	<i>No data available</i>

*Table 1. 1. Examples of Ion-recombination mechanisms in the dynamic charging conditions using in-situ EQCM (Levi *et al.*, 2010) (Wu *et al.*, 2017)/ XRT (Prehal *et al.*, 2015)/IR (Richey *et al.*, 2014) techniques.*

The above-mentioned ion recombination mechanisms play a vital role in the performance of supercapacitors. Considering the thermodynamic conditions of charging, free energy related to charging is required in achieving high values of capacitance. For example, (Kondrat *et al.*, 2016) points out that the adsorption mechanism faces electrostatic blockade with the same charge ions present in the pores, which makes less fellow ions to go inside the carbon pore. Such blockade increases the price tag of charging and contributes to lower values of capacitance. Whereas, lack of electrostatic blockage with swapping and desorption lowers thermodynamic cost of charging and results in higher capacitance. Besides, as swapping keeps the same quantity of ions in the pore, a higher magnitude of capacitance is observed with swapping. As pointed by (Forse *et al.*, 2016; Kondrat *et al.*, 2016), the possibility of having ion recombination such as swapping, adsorption, and desorption depends upon various factors. Some includes (i) the electrolyte ion population in the carbon pore at zero potential, (ii) polarization sign of carbon electrode (either positive or negative potentials), and (iii) the type of electrolyte ions and as well as the carbon.

1.3.2. Pseudocapacitors

Pseudocapacitive materials store charges through a quick change in the valence state of the electrode material (Simon, Gogotsi and Dunn, 2014; Brousse, Bélanger and Long, 2015; Gogotsi and Penner, 2018). There are three possible types of pseudocapacitance: (i) Underpotential decomposition, in which the electrolyte ions are placed at the interface of a metal-electrolyte during the positive potentials of their redox reactions; (ii) redox pseudocapacitance, redox reactions related to surface of the electrode material; and (iii) Intercalation pseudocapacitance, where ion inserts into the layered materials with no change of crystallographic phase. **Table 1.2**, summaries the types of pseudocapacitance reaction observed so far.

Pseudocapacitance type	Process	Examples:
Under-potential decomposition	$M + xA^{\delta+} + x\delta e^- \leftrightarrow A.M$ <p>Where M is metal (e.g. Au or Pt), A is the adsorbed atoms (e.g., Pd or H), x is the number of the adsorbed atoms, δ is the valence of the adsorbed atoms and $x\delta$ is the number of electrons transferred.</p>	<p>H^+ ion adsorbents on Pt; Pd^{2+} on Au (Herrero, Buller and Abruña, 2001; Sudha and Sangaranarayanan, 2002)</p>
Redox	<p>Cation type insertion: $Oxidized + \delta A + \delta e^- \leftrightarrow Reduced A_{\delta}$</p> <p>Anion type redox: $Reduced B_{\delta} \leftrightarrow Oxidized + \delta B + \delta e^-$</p> <p>Where, A is the electrolyte cation adsorbed on the surface (e.g. $A = Li^+, H^+, Na^+, K^+, Mg^{2+}...$) and B is the electrolyte anion (e.g. $B = OH^-, O^{2-}...$) and δ is the number of electrons transferred.</p>	<p>Ruthenium Oxide (Long <i>et al.</i>, 2002): $RuO_x(OH)_y + \delta H^+ + \delta e^- \leftrightarrow RuO_{x-\delta}(OH)_{y+\delta}$ ($Max(\delta) = 2$)</p> <p>Manganese Oxide (Toupin, Brousse and Bélanger, 2004): $MnO_2 + \delta A^+ + \delta e^- \leftrightarrow MnOOC_{\delta}$</p> <p>Molybdenum Oxide (Mendoza-Sánchez <i>et al.</i>, 2013): $MoO_3 + \delta A^+ + \delta e^- \leftrightarrow M_{\delta}MoO_3$ ($Max(\delta) = 1$)</p> <p>Vanadium Nitride (Choi, Blomgren and Kumta, 2006): $VN_xO_y + OH^- \leftrightarrow VN_xO_y OH^- + VN_xO_y-OH + e^-$</p>

Intercalation	$MO_y + \delta A + \delta e^- \leftrightarrow A_\delta MO_y$ <i>Where MO_y is the lattice layer host material</i>	2-D Titanium Carbide MXene (Ghidiu <i>et al.</i> , 2015): $Ti_3C_2O_x(OH)_yF_z + \delta e^- + \delta H^+ \leftrightarrow Ti_3C_2O_{x-\delta}(OH)_{y+\delta}F_z$ Niobium Oxide (Griffith <i>et al.</i> , 2016): $Nb_2O_5 + \delta Li^+ + \delta e^- \leftrightarrow Li_\delta Nb_2O_5$ ($Max(\delta) = 2$)
---------------	---	---

Table 1.2. Elaborates some examples of the pseudocapacitance type of mechanism.

Some examples of underpotential pseudocapacitance are the deposition of the H^+ ion on Pt surfaces and the Pd^{2+} on Au surfaces (Herrero, Buller and Abruña, 2001; Sudha and Sangaranarayanan, 2002). Redox type of pseudocapacitive materials takes advantage of the redox electron transfer between oxidized and reduced species at the surface of the electrode materials (Crosnier *et al.*, 2018). Some examples of the redox pseudocapacitive oxides materials are RuO_2 (Zheng, 1995; Conway, 2013), IrO_2 (Crosnier *et al.*, 2018), MnO_2 polymorphs (Ghodbane, Pascal and Favier, 2009), Fe_3O_4 (Wu, 2002), $FeWO_4$ (Goubard-Bretesché *et al.*, 2015) and $MnFe_2O_4$ (Kuo and Wu, 2005), $ZnMn_2O_4$ (Abdollahifar *et al.*, 2018), $Ba_{0.5}Sr_{0.5}Co_{0.8}Fe_{0.2}O_{3-\delta}$ (Lannelongue, Le Vot, *et al.*, 2018), $La_{1-x}Sr_xMnO_3$ (Crosnier *et al.*, 2018). Whereas, with intercalation pseudocapacitance mechanism, the electrolyte ions intercalate into the layered material or crystal structure, which accompanies with the change of valance state of metal or expansion and/or compression of the material's interlayers. Importantly, in such cases pseudocapacitive charge is largely dependent upon various factors, such as the Faradaic reactions attributed to diffusion of the electrolyte ions in the material's bulk-solid, fast surface ion dynamics and as well as the non-Faradaic reactions such as electric double layer capacitance (Augustyn, Simon and Dunn, 2014; Perez *et al.*, 2018). In general, the response of any electrode materials can be shown by their I-V curves, which can be represented as (John Wang *et al.*, 2007):

$$i = av^b \quad (1.4)$$

Where i (mA) is the current observed at a scan rate of v (mVs⁻¹), with adjustable parameters of a and b . In pseudocapacitive materials, the b value in Eq. (1.4) is ~ 1 (John Wang *et al.*, 2007; Simon, Gogotsi and Dunn, 2014), which indicates a linear dependence in the increase of current over increasing charging or discharging rates, eventually resembling the behavior of an electric double layer capacitance. Taking this into account, pseudocapacitive materials also show linear response with the increase of voltage during a constant applied current. Whereas, in bulk solid-state diffusion process (like batteries), which satisfies the Cottrell's equation, the value of b is ~ 0.5 (Simon, Gogotsi and Dunn, 2014), which indicates the occurrence of semi-infinite diffusion dominated charge storage. This is typically seen with battery materials like LiCoO₂ (Simon, Gogotsi and Dunn, 2014). However, decreasing the grain size of the materials below 10 nm can also give signatures of pseudocapacitance behavior. In such cases, decreasing grain size increases the active sites, which are usually near the surface of the material with a distance (Gogotsi and Penner, 2018):

$$\ll (2Dt)^{1/2}, \quad (1.5)$$

In this case, t is the diffusion time range (s) and D is the diffusion coefficient for charge-compensating ions (cm² s⁻¹). In this scenario, materials are forced to have pseudocapacitive-like behavior. Such type of charge storage behavior is termed as *extrinsic-pseudocapacitance* (Simon, Gogotsi and Dunn, 2014). Nano-TiO₂ with an average grain size of 7 nm is one such example (John Wang *et al.*, 2007). Though some materials like T-phase of Nb₂O₅ (Griffith *et al.*, 2016) and 2-D MXenes like Ti₃C₂ (Lukatskaya, Mashtalir, Ren, Dall'Agnesse, Rozier, Taberna, Naguib, Simon, Barsoum, Gogotsi, *et al.*, 2013; Ghidui *et al.*, 2015)

show pseudocapacitive behavior profile even when the materials are in their bulk state. Such behavior is termed as *intrinsic pseudocapacitance*.

1.3.3. Why pseudocapacitors are interesting than carbon-based double layer capacitors?

The electrode made up of porous carbon materials exhibit packing densities lower than 1 g cm^{-3} , as porous carbons exhibit surface areas greater than ($> 1000 \text{ m}^2 \text{ g}^{-1}$) (Gogotsi and Simon, 2011). Besides this, the charge stored in porous carbon electrodes is relevant to the recombination of the electrolyte ions within the carbon pore and the bulk liquid electrolyte, carbon-based double layer capacitors show charge polarizations lower than $12 \text{ } \mu\text{F cm}^{-2}$ (Charge polarization is carried out by normalizing the value of charge with BET-specific surface area of the material). Both of these factors make the volumetric capacitance in porous carbon electrodes between 15 and 25 F cm^{-3} (Largeot *et al.*, 2008; Jäckel *et al.*, 2016). Such values of volumetric capacitance are low, which limits the use of EDLCs in applications where the size or volume of the energy storage device is critical (Gogotsi and Simon, 2011). Pseudocapacitor offers an alternative to this issue. As mentioned in the above section, the materials of pseudocapacitor store charges either by fast redox reactions or by ion intercalation process, which allows the pseudocapacitive materials to exhibit charge polarization $> 50 \text{ } \mu\text{F cm}^{-2}$ (Brousse *et al.*, 2017). These values are generally higher than carbon-based electrode materials (Simon, Gogotsi and Dunn, 2014; Lukatskaya, Dunn and Gogotsi, 2016). Apart from this, interestingly, pseudocapacitive materials also exhibit higher material densities ($> 2.0 \text{ g cm}^{-3}$ (Goubard-Bretesché, Crosnier, Favier, *et al.*, 2016)). Therefore, the electrode materials made up of the pseudocapacitive materials display packing densities $> 1 \text{ g cm}^{-3}$. Both of these factors contribute to the value of volumetric capacitance greater than 50 F cm^{-3} in the electrochemical devices made up of pseudocapacitive materials (Goubard-Bretesché, Crosnier, Favier, *et al.*, 2016).

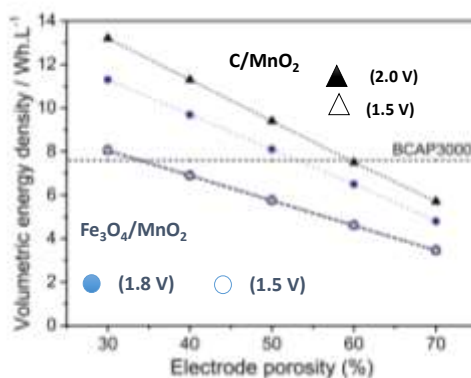


Figure 1. 4. Correlation between the electrode porosity and the volumetric energy density of pseudocapacitors and hybrid devices. Figure adapted from (Goubard-Bretesché, Crosnier, Favier, *et al.*, 2016) with permission from Elsevier. The data in the figure is compared with the porous carbon electrodes (BCAP₃₀₀₀ from Maxwell Technologies. Inc. The nominal voltage in this cell is 2.7 V). Closed legends in the figure indicate that the possible operational cell voltages. Whereas, open legends indicate the safe operational cell voltage.

Thanks to the proportional relationship between capacitance and energy, as previously shown by Eq. 1.2, such high values of volumetric capacitances could provide high volumetric energy densities. This way pseudocapacitors are useful in the applications where the volume of the device is crucial. **Figure 1.4** shows a comparison scenario between pseudocapacitors (like Fe₃O₄//MnO₂) and activated carbon-based supercapacitors (BCAP₃₀₀₀).

1.4. Problems tackled in this thesis

1.4.1. Low capacitive response of EDLCs at high-rates

Although, supercapacitor community has been improving the capacitance by highly charging the carbon surface present at the FSI (Chmiola, 2006; Merlet *et al.*, 2012, 2013), growing interest has also been focused towards moving, delivering or retaining these charges at high charging and discharging rates (Kondrat and Kornyshev, 2013; Kondrat *et al.*, 2014, 2016; Péan *et al.*, 2014). The

agenda behind this strategy is to have both high energy and power capabilities in a supercapacitor device. The reduction of capacitance values is understood to be caused by the hindrance in the electrolyte ion movement within the carbon pore and as well as its diffusion throughout the binder based electrode (Merlet *et al.*, 2012, 2013; Dyatkin *et al.*, 2016). The issue of ion accessibility in traditional binder based electrodes is shown in **Figure 1.5a**. To resolve this issue, fine-tuning of the electrode structure, as well as pore distribution in the microporous range, are needed.

Unlike micro-supercapacitors (Gogotsi and Simon, 2011), the commercial macro-size supercapacitors use binder composite electrodes with thicknesses exceeding a few hundred micrometers. This decreases the electrolyte utilization of an electrode and gives rise to low values of capacitance ($5\text{-}12\ \mu\text{F cm}^{-2}$ or $65\text{-}140\ \text{F g}^{-1}$ (Bloom, 1975; Chmiola, 2006; Gao *et al.*, 2015)). Additionally, as in general, binders are poorly conducting, the overall intrinsic conductivity of the electrode also reduces. Besides, the hydrophobicity of most binders make electrodes to have high ionic resistance (*e.g.* polyvinylidene fluoride, contact angle $85\text{-}114^\circ$ in water (Avireddy *et al.*, 2016)). These aspects lead to electrodes with low-rate capability (Zhang *et al.*, 2016). Another possibility is to use 2-D carbons based electrodes. Some examples of 2-D carbons are Graphene sheets or Graphene hybrids. However, even in the architecture of 2-D sheet, there is an occurrence of restriction in electrolyte ion accessibility (as shown by **Figure 1.5b**), as also highlighted by (Xu *et al.*, 2014) in their studies. Therefore, it is essential to work towards other electrode architectures.

Approach for this problem

As highlighted in the review of (Lukatskaya, Dunn and Gogotsi, 2016), free-standing three-dimensional (3-D) porous carbons could offer an alternative solution to the low rate capability in binder based electrodes. As free-standing 3-D architecture based electrodes provide better accessibility of the electrolyte

ions throughout the electrode. This concept is also illustrated in **Figure 1.5c**. Thanks of this, the free-standing 3-D architecture based carbon electrodes exhibit higher specific surface charge or charge polarization than traditional binder composite electrodes (Bloom, 1975; Qie *et al.*, 2013; Luan *et al.*, 2015; Wang *et al.*, 2016; Yang *et al.*, 2017). **Figure 1.6** shows the data of charge polarization of several binder based carbon electrodes (black legends) and as well as a free-standing 3-D electrode architecture in an aqueous 6 M of potassium hydroxide electrolyte solution. This figure indicates that the binder based electrodes (which also includes new hybrids carbon electrodes), shows lower charge polarization than ($< 25 \mu\text{F cm}^{-2}$) than free-standing 3-D carbons

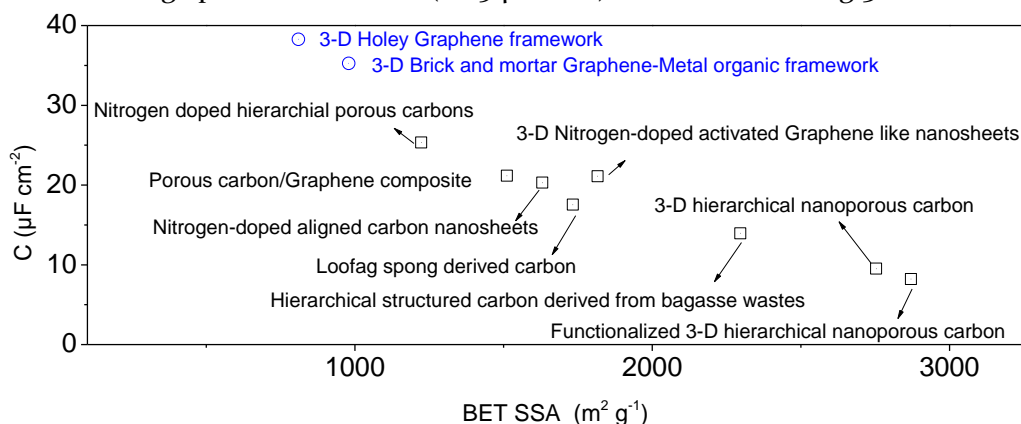


*Figure 1. 5. Charge polarization of various carbon electrodes in aqueous 6 M KOH electrolyte solution. Charge polarization is calculated by normalizing the capacitance with the BET-SSA of the carbon material. The carbons electrodes in the plot are 3-D holey Graphene framework (Xu *et al.*, 2014), 3-D brick and mortar Graphene-Metal organic framework (Wang *et al.*, 2016), Nitrogen-doped hierarchical porous carbons (Yang *et al.*, 2017), Porous carbon-Graphene composite (Sun *et al.*, 2015), Nitrogen-doped aligned carbon nanosheets (Zhou *et al.*, 2017), Loofag sponge derived carbon (Luan *et al.*, 2015), hierarchical structured carbon derived from bagasse wastes (Feng *et al.*, 2016), 3-D doped activated Graphene like nanosheets (Li *et al.*, 2016), Functionalized 3-D hierarchical nanoporous carbon and 3-D hierarchial nanoporous carbon (Qie *et al.*, 2013). Black color circle represents binder based electrodes. Whereas, Blue color box represents binder free electrodes*

($\sim 35 \mu\text{F cm}^{-2}$, (Wang *et al.*, 2016)). So, the use of free-standing 3-D electrode architecture seems to be promising to achieve both high energy and power capabilities in carbon-based supercapacitors. Therefore, **chapter 3** of this thesis is dedicated to fabricating binder free and self-standing electrodes based on the 3-D architecture for supercapacitors.

1.4.2. Low cell voltages in aqueous pseudocapacitors

As mentioned in section 1.3.3, pseudocapacitive materials show rapid redox reactions leading to high charge polarizations ($> 35 \mu\text{F cm}^{-2}$) and higher electrode densities ($> 2.0 \text{ g cm}^{-3}$). These factors contribute to high volumetric capacitances in devices. Nonetheless, remarkable electrochemical properties of pseudocapacitive materials are often seen when they are analyzed in aqueous electrolytes. Such behavior is attributed to high dielectric constants ($\epsilon = 78$ at $25 \text{ }^\circ\text{C}$), ionic conductivities ($> 50 \text{ mS cm}^{-1}$), low viscosities ($< 5 \text{ mPa s}$) and rapid ion diffusions in aqueous electrolytes when compared to non-aqueous based electrolytes (Borodin *et al.*, 2017). An example of a non-aqueous electrolyte can organic liquids like acetonitrile ($\epsilon = 36.8$ at $25 \text{ }^\circ\text{C}$, ionic conductivities $< 10 \text{ mS cm}^{-1}$, low viscosities $> 30 \text{ mPa s}$, (Borodin *et al.*, 2017)).

Before pointing out the issues in using aqueous electrolytes, it is noteworthy that the pseudocapacitive materials have their own standard electrode potentials. And, this according to (Li *et al.*, 2018), is related to the Fermi energies of their electron band. In this scenario, for redox reactions to happen, energies of the Fermi level must be matched with the suitable occupied (Highest Occupied Molecular Orbitals, HOMO) or vacant orbitals (Lowest Unoccupied Molecular Orbitals, LUMO) in the reactant. Besides this, an external force, such as an applied potential is required to make the transfer of electron for the redox reaction to happen. This applied potential is the standard electrode potential. Considering this, the following section explains the issue related to the use of aqueous solutions as electrolyte media.

Generally, the electrochemical potential window of an electrolyte solution depends upon its thermodynamic stability, which is defined as the energy separation between its LUMO and HOMO (Goodenough and Park, 2013), as shown by **Figure 1.7**. According to (Goodenough and Kim, 2010), if the negative electrode material has a Fermi level lower than LUMO, the electrolyte reduces. Whereas, if the positive electrode has a Fermi level higher than HOMO, the electrolyte solution oxidizes. Therefore, it is important to match the Fermi levels of the electrodes with the LUMO and HOMO of the electrolytes to have a stable cell voltage. Now, taking this into account, though, the theoretical voltage limit for the water decomposition is 1.23 V (Demarconnay, Raymundo-Piñero and Béguin, 2010), as shown in **Figure 1.8**, wider windows (1.6 – 1.9 V) can be reached with neutral aqueous electrolytes (pH 7.0)(Fic *et al.*, 2012). This is acknowledged to the high over-potentials for hydroxide ion generation and hydrogen evolution in near neutral pH electrolytes (Gao *et al.*, 2012).

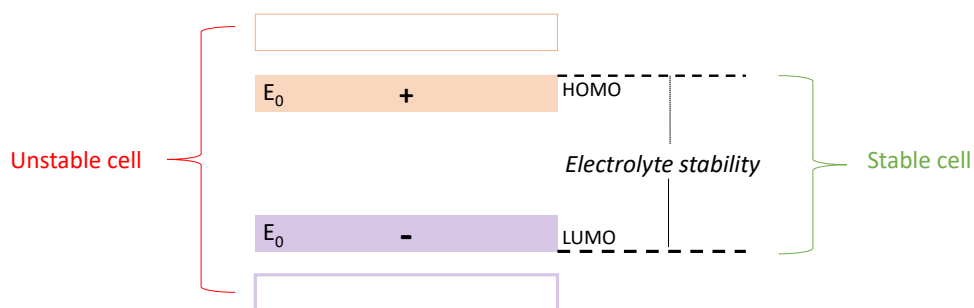
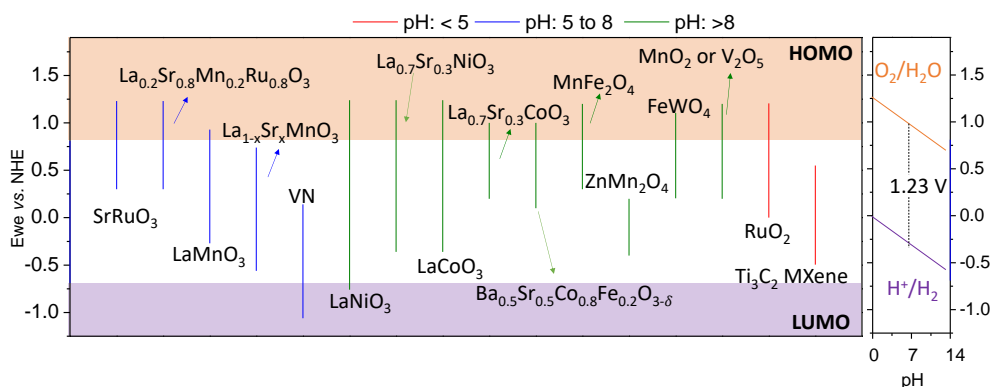


Figure 1. 6. Schematic illustrates the association between the electrolyte electron energies (HOMO and LUMO) and the standard electrode potentials of the electrode (E_0)

Considering the list of some pseudocapacitive materials, as also shown in **Figure 1.8**, the cells made with pseudocapacitive materials can be operated between 0.6 and 1.9 V (Max.). A good example would be an asymmetric cell configuration of $\text{FeWO}_4//\text{MnO}_2$ which can be operated between 1.2 and 1.4V in 5 M LiNO_3 (Goubard-Bretesché, Crosnier, Buvat, *et al.*, 2016). Nevertheless, when compared to the cell voltages of organic electrolyte based supercapacitors (2.3 to 3.0 V, e.g. in Acetonitrile (Goubard-Bretesché, Crosnier, Favier, *et al.*, 2016)), the voltages in aqueous pseudocapacitors are still narrow. These narrow cell voltages make the aqueous pseudocapacitors to suffer from limited energy densities. This drawback restrains them in applications when high volumetric energy densities are predominately requisite, along with high power ratings.



*Figure 1. 8. Schematic illustrates the relationship between the electrochemical potential window of various pseudocapacitive electrode materials with the electrochemical stability range of water (between the electrolyte electron energies, HOMO and LUMO). The data related to the electrochemical potential windows of the pseudocapacitive materials were obtained from various reviews (Anasori, Lukatskaya and Gogotsi, 2017; Crosnier *et al.*, 2018; Li *et al.*, 2018)*

Approach for this problem

Strategy – I: Using a new family of pseudocapacitive MXenes as electrode materials

Nanomaterials like 2-D metal carbides and nitrides, called MXenes, also shown intercalation type of pseudocapacitance mechanism (Lukatskaya, Dunn and Gogotsi, 2016; Anasori, Lukatskaya and Gogotsi, 2017). Generally, MXenes can be synthesized by selective etching of a layered ternary carbide ceramic, $M_{n+1}AX_n$ ($1 \leq n \leq 3$) in hydrofluoric acid (Naguib *et al.*, 2011). Where, M refers to a transition metal such as Molybdenum, Titanium, Vanadium, Tantalum, Niobium or Chromium and A as an element from groups 13 and 14 (Aluminum, Gallium, Silicon, Iridium or Germanium). And X characteristics to Nitrogen and/or Carbon (Barsoum, 2000, 2013). Among the family of MXenes, Titanium Carbide (Ti_3C_2) was the first one to be discovered and an intensive effort of research on its synthesis and processing has led the Ti_3C_2 MXene to exhibit a

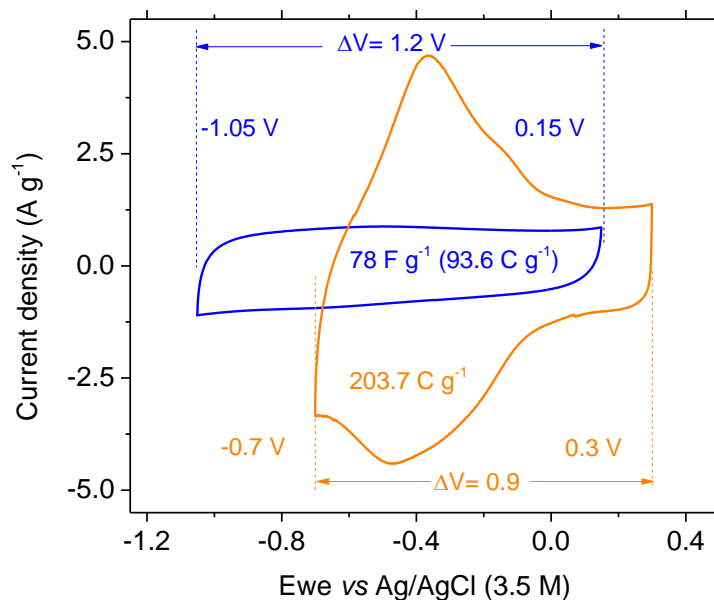
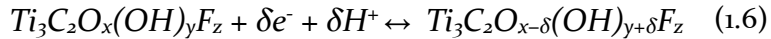


Figure 1. 9. Shows the cyclic voltammogram of the 2-D Ti_3C_2 MXene in non-acidic electrolyte (blue color curve, 1 M of aqueous lithium sulfate solution, pH = 9.7) and acidic electrolyte (red color curve, 1 M aqueous sulfuric acid solution, pH = 0.0)

high metallic conductivities ($>1,000 \text{ S cm}^{-1}$) and volumetric capacitances ($900\text{--}1,500 \text{ F cm}^{-3}$) (Naguib *et al.*, 2011; Naguib and Gogotsi, 2015; Alhabeab *et al.*, 2017). However, high values of volumetric capacitances are generally observed only in acidic electrolyte solutions. The charge storage of 2-D MXenes in acidic and neutral electrolytes is explained in the following section. According to (Lukatskaya, Mashtalir, Ren, Dall'Agnesse, Rozier, Taberna, Naguib, Simon, Barsoum and Gogotsi, 2013), in neutral electrolytes (where pH is near to 7), several cations such as Li^+ , Na^+ , K^+ , and Mg^{2+} can insert within the interlayer of Ti_3C_2 MXene, giving rise to a capacitive-like response of charge. While, high quantity of protons in acidic electrolytes, where pH is often close to that of 0.0, intercalates within the interlayers of MXene and as well as interacts with the surface terminal groups of Ti_3C_2 . Which, according to (Hope *et al.*, 2016) is $\text{Ti}_3\text{C}_2\text{T}_x$, in which T_x represents the terminal groups like $-\text{OH}$, $-\text{F}$, $=\text{O}$. The proton interacts with these terminal groups via a redox reaction, as $\text{Ti}-\text{O}$ to $\text{Ti}-\text{OH}$ (Hu *et al.*, 2016), which according to (Lukatskaya *et al.*, 2017) can also be represented by:



As, charge storage in acidic electrolytes is attributed to these dual processes (intercalation, and redox reactions), an extra charge value of the charge is observed in acidic electrolytes, which is almost 2-fold higher than the values witnessed in the neutral electrolytes. Nevertheless, narrow electrochemical potential windows are observed in acidic electrolytes. This limitation is mainly due to the shift of the electrochemical potential towards the higher vertexes, which according to the Nernst equation can be given as (Li *et al.*, 2018):

$$E_{\text{negative}} = -0.059 \text{ pH} \quad (1.7)$$

This negative vertex potential, in the case of Ti_3C_2 MXene, is about -0.7 V vs Ag/AgCl , which gives an electrochemical potential window of 0.9 V (total

potential window: 0.3 to -0.7 V vs Ag/AgCl, in an aqueous solution of 1 M sulfuric acid, *see figure 1. 9*). Whereas, the vertex negative potential is -1.05 V vs Ag/AgCl in near neutral solutions like aqueous of 1 M lithium sulfate, giving a potential window of 1.2 V (total potential window: 0.15 to -1.05 V vs Ag/AgCl, *see figure 1. 9*). Since the electrochemical potential window is in the negative region (vs Ag/AgCl), Ti_3C_2 MXene is considered as a negative electrode. As narrow electrochemical windows are observed in acidic electrolytes, the cells composed of Ti_3C_2 MXene (as $\text{Ti}_3\text{C}_2//\text{Ti}_3\text{C}_2$) also exhibits a low cell voltage (0.6 V). And, as energy in an electrochemical supercapacitor has a proportionality to the voltage (according to Eq. (1.1)). The supercapacitor devices composed of Ti_3C_2 MXene suffers from low values of energy densities. These limitations restraint the use of Ti_3C_2 MXene in the applications where high energy densities are desirable. Based on this discussion, one strategy to tackle this problem is to look into the MXene phases which can be used as a positive electrode. Many MXenes can exist with different transition metal layer, such as Molybdenum, Titanium, Vanadium, Tantalum, Niobium or Chromium (Barsoum, 2000, 2013). Among these, very recently, (Tao *et al.*, 2017; Meshkian *et al.*, 2018) showed new MXenes like Mo_2C store charges in the positive electrochemical potential window (-0.3 V to 0.3 V vs Ag/AgCl, in 1 M H_2SO_4), when compared to the potential windows of Ti_3C_2 MXene electrode (0.3 to -0.7 V vs Ag/AgCl). And, therefore MXenes like Mo_2C are considered to be as a positive electrode material. However, (Tao *et al.*, 2017; Meshkian *et al.*, 2018) also showed that the electrochemical and electrical properties new MXenes like Mo_2C MXene can be further improved with the atomic row engineering of the metal layered in MXenes phase. For example, (Tao *et al.*, 2017; Meshkian *et al.*, 2018) showed that by varying the etching process, atomic vacancies can be achieved in Mo_2C MXene, forming $\text{Mo}_{1.33}\text{C}$ MXene. In such a case, $\text{Mo}_{1.33}\text{C}$ MXene showed a magnitude of difference in conductivity when compared to Mo_2C MXene. Besides, $\text{Mo}_{1.33}\text{C}$ also showed 65 % higher electrochemical charge

storage than Mo_2C MXene. Although the method of atomic row engineering could result in MXenes with better electrochemical and electrical properties, atomic row engineering requires tremendous control during the etching and delamination process. Another strategy could be to use MAX phases with different atomic arrangements (like that's of solid-state solution). And, etching of such MAX phases could results MXenes with different atomic arrangements. Towards this strategy, double transition MXenes based on Molybdenum and Vanadium carbides, $(\text{Mo},\text{V})_4\text{C}_3$ are promising. $(\text{Mo},\text{V})_4\text{C}_3$ MXene is different than the traditional double transition MXenes, such as ordered structures of $\text{Mo}_2\text{Ti}_2\text{C}_3$ and Mo_2TiC_2 (Anasori *et al.*, 2015). (Anasori *et al.*, 2015) predicts that the lower energy difference between the different phases of $(\text{Mo},\text{V})_4\text{C}_3$ MXenes, makes the $(\text{Mo},\text{V})_4\text{C}_3$ MXenes to exhibit atomic disordering (like solid-solution, $\text{Mo}_x\text{V}_{4-x}\text{C}_3$, **figure 1. 10**). Therefore, the use of MXenes like $(\text{Mo},\text{V})_4\text{C}_3$ could provide enhanced electrochemical properties. Besides this, since the composition of the $(\text{Mo},\text{V})_4\text{C}_3$ MXenes combines high electronegative transition metals like (Mo; 2.16) and low (V; 1.63), which is a beneficial factor in regards with the electrical properties. Therefore, in 2018 David *et al* (*unpublished work*) synthesized $\text{Mo}_x\text{V}_{4-x}\text{C}_3$ MXenes, with $x = 1, 2$ and 2.7 . Among

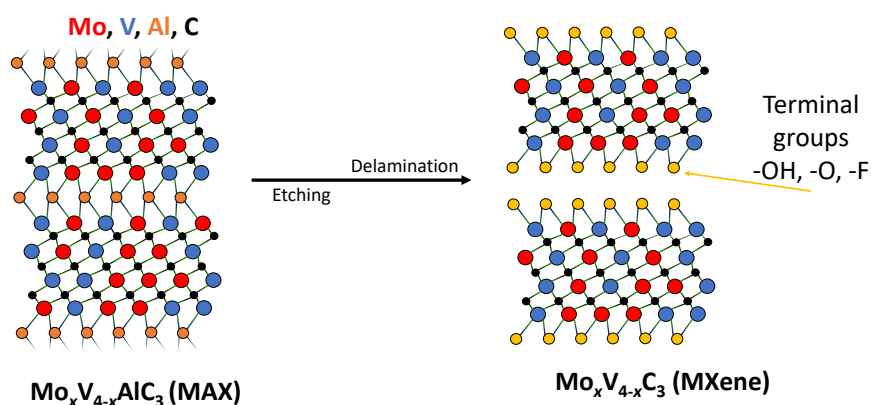


Figure 1. 10. Schematic illustration of the crystallographic structure of the $\text{Mo}_x\text{V}_{4-x}\text{AlC}_3$ MAX and corresponding $\text{Mo}_x\text{V}_{4-x}\text{C}_3$ MXene, obtained by the etching and delamination of the $\text{Mo}_x\text{V}_{4-x}\text{AlC}_3$ MAX.

all these phases, it was found that the MXene with $x=2.7$, $\text{Mo}_{2.7}\text{V}_{1.3}\text{C}_3$ is the most efficient composition with a maximum volumetric capacitance of 860 F cm^{-3} in 1 M sulfuric acid, followed by $\text{Mo}_2\text{V}_2\text{C}_3$ (680 F cm^{-3}), while MoV_3C_3 show almost 50 % lower capacitance than $\text{Mo}_{2.7}\text{V}_{1.3}\text{C}_3$ (450 F cm^{-3}) (see **figure 1. 11**). As it was previously demonstrated with Ti_3C_2 MXene that MXene surfaces showing a higher concentration of O-type termination groups stores the highest capacitance (Lukatskaya, Mashtalir, Ren, Dall’Agnese, Rozier, Taberna, Naguib, Simon, Barsoum and Gogotsi, 2013; Lukatskaya *et al.*, 2017), see also Eq. (1.6). Therefore, it was supported that the higher O-type groups in $\text{Mo}_{2.7}\text{V}_{1.3}\text{C}_3$ allow it to display enhanced electrochemical performance (See **figure 1. 11**). Since, $\text{Mo}_{2.7}\text{V}_{1.3}\text{C}_3$ MXene shows the best electrochemical performance among other $\text{Mo}_x\text{V}_{4-x}\text{C}_3$ phases and therefore, it can be used

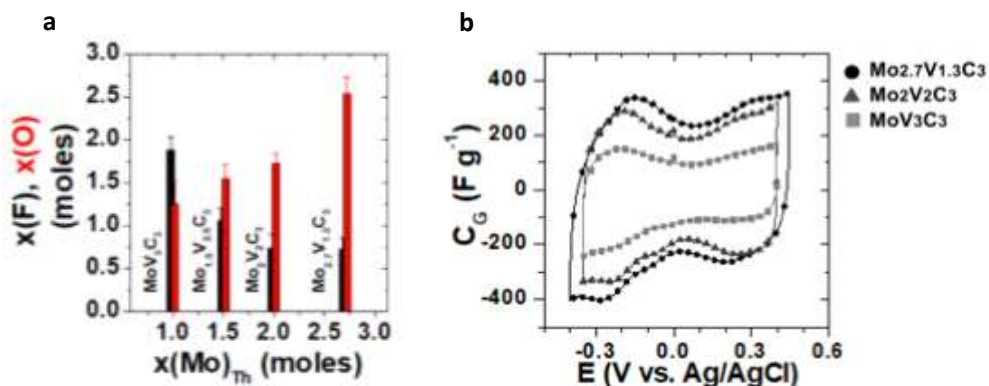


Figure 1. 11. (a) Distribution of the oxygen ($x(\text{O})$) and fluorine ($x(\text{F})$) content of the $(\text{Mo}, \text{V})_4\text{C}_3$ MXenes MLs, as determined by energy dispersive X-Ray spectroscopy. Cyclic voltammetry on films of the $(\text{Mo}, \text{V})_4\text{C}_3$ MXenes. Unpublished work, data is provided by Dr. David Pinto from the Drexel University.

further for the electrochemical studies. And, therefore, the coupling of $\text{Mo}_{2.7}\text{V}_{1.3}\text{C}_3$ with Ti_3C_2 in the asymmetric configuration would further extend the cell voltages of the MXene based pseudocapacitor, which still remains unexplored. Therefore, **chapter 4** of this thesis is dedicated towards the assembly of $\text{Mo}_{2.7}\text{V}_{1.3}\text{C}_3$ with Ti_3C_2 MXene in the asymmetric configuration cell.

Strategy II- Using super-concentrated solutions as water-in-salt electrolytes

As highlighted in the above *section*, the voltage of the electrochemical device is dependent upon the electrochemical potential windows of both positive and negative electrodes and as well as on the electrochemical stability of the electrolyte solution. According to (Smith and Dunn, 2015), the stability of an aqueous electrolyte can either be extended by reducing the reaction kinetics related to the water splitting and/or by forming passive layers. The presence of passive layers avoids migration of the electron from the electrode surface to the electrolyte HOMO and LUMO (Li *et al.*, 2018), which could extend the

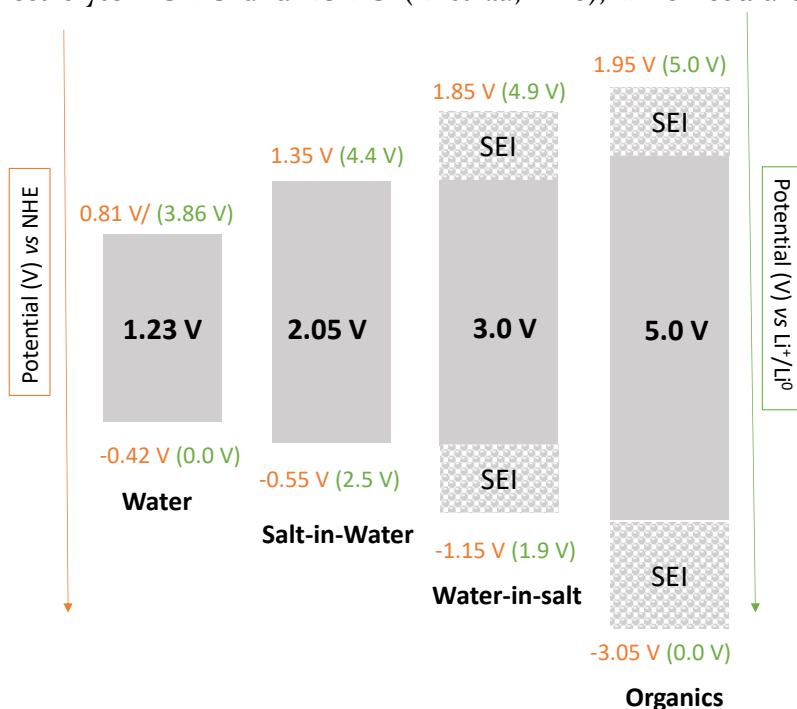


Figure 1. 12. Illustration of the electrochemical potential window of the water, salt-in-water (eg. 1 m of Li-TFSI), water-in-salt (eg. 21 m of Li-TFSI) and organic electrolytes (eg. LiPF₆ in EC-DMC). This illustration is created using the data available in various references ((Smith and Dunn, 2015; Suo *et al.*, 2015; Borodin *et al.*, 2017; Coustan, Shul and Bélanger, 2017; Tian *et al.*, 2017))

stability window of the electrolytes. Such has been seen in batteries when they are composed of organic and ionic liquids (Goodenough and Park, 2013). In such cases, passive layers, which are also termed as solid-electrolyte interfaces (SEIs), allows the electrode materials to operate beyond the stability limits of their electrolyte solutions (Goodenough and Kim, 2010). To a certain extent, the traditional aqueous electrolyte with salt concentrations $< 5 \text{ mol kg}^{-1}$, the SEI formation is not witnessed during the investigations (Dubouis *et al.*, 2018). Interesting, recently, a new class of super-concentrated aqueous electrolytes such as *water-in-salt* created a paradigm shift in the field (Suo *et al.*, 2015). In such high concentrations, the amount of salt is usually greater than water, which according to (Lannelongue, Bouchal, *et al.*, 2018), can also be signified

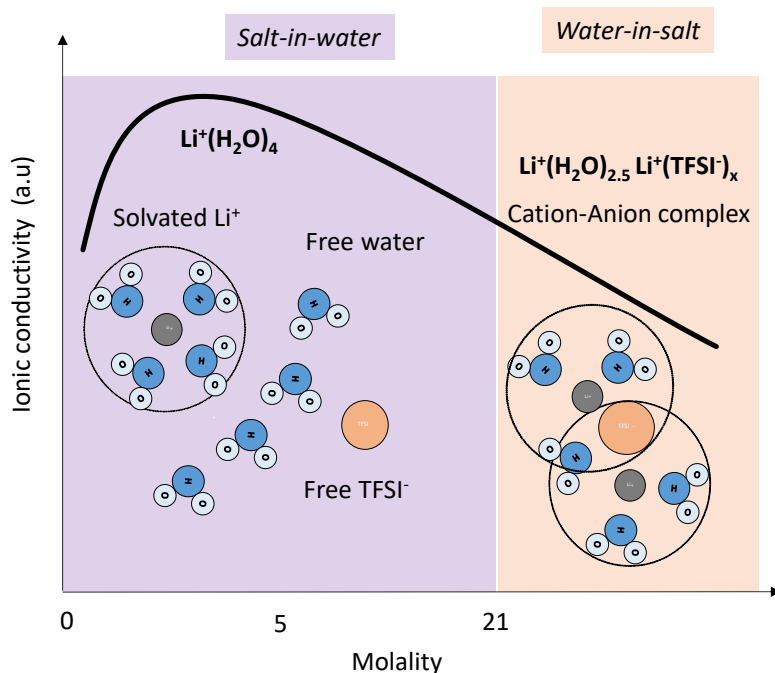


Figure 1.13. Schematic illustration of the solvation sheath of Li^+ cations and TFSI^- anions from low to high concentration of the aqueous electrolytes. This illustration is created based on the various understanding by several authors (Borodin *et al.*, 2017; Coustan, Shul and Bélanger, 2017; Dubouis *et al.*, 2018)

as $mass_{salt}/mass_{water}$ or $volume_{salt}/volume_{water} > 1$. Because of the high salt to water ratio, the water molecules in the solvation sheath of electrolyte ion reduces, which helps in reducing the reaction kinetics of water splitting reactions (Suo *et al.*, 2015). Whereas, certain anions of electrolyte salt has a possibility to coexist in the solvation sheath of the cations, which at certain electrochemical potential reduces to form passive layers. According to (Smith and Dunn, 2015), both of these aspects extend the electrochemical stability of the electrolyte solutions (**Figure 1. 12**). In this scenario, super-concentrated Li-TFSI salt based aqueous electrolyte is a good example. In the case of Li-TFSI based water-in-salt electrolyte, according to (Borodin *et al.*, 2017), when the concentration of Li-TFSI salt is increased from 1 to 20 m (mol kg⁻¹), the molar ratio between water-to-salt reduces from 55.6 to 2.6. This lowers the number of water molecules from the solvation sheath of Li⁺ cation and involves the TFSI⁻ anion in the solvation sheath of Li⁺. According to (Borodin *et al.*, 2017), this can also be denoted as Li⁺(H₂O)₄ to nearly a cation-anion complex of Li⁺(H₂O)_{2.5} Li⁺(TFSI⁻)_x (with $x > 1$, with a possibility of $x=2$), as shown by **Figure 1. 13**. Although, the effect of using this complex cation-anion environment and in-turn to the extension of the electrochemical stability of the electrolyte is still in under debate. But, to a certain extent, it is proposed by (Coustan, Shul and Bélanger, 2017), that the cation-anion complex on the positive vertex potential avoids the migration of water on the electrode surface, which increases the onset electrochemical potential of oxygen evolution reaction. Whereas on the negative potentials, according to (Dubouis *et al.*, 2018), the reduction of water generates highly reactive OH⁻ ions, which reacts with TFSI⁻ anions to form a passive layer of LiF and CF_x. This, according to several authors (Kühnel *et al.*, 2016; Tian *et al.*, 2017; Dubouis *et al.*, 2018), are the reasonable factors to extend the electrochemical window of the Li-TFSI based water-in-salt electrolyte up to a surprisingly high value of 3.0 V. Such a high value is in-fact what is observed in batteries consisting of organic electrolytes. As a whole, considering

the benefit of using water-in-salt electrolytes concerning the extension of the voltages, the approach of using water-in-salt electrolyte can help in resolving the issue of low energy densities in aqueous pseudocapacitors. Therefore, *chapter 5* of this thesis is dedicated to the implementing of water-in-salts as an electrolyte media for high-voltage pseudocapacitors.

1.4. Summary and conclusions

This chapter introduces supercapacitors, as an electrochemical energy storage device which delivers high power densities and long cycle life. However, unlike batteries, supercapacitors suffer from low energy densities, which restraints them in the applications when high energy densities are desirable along with high power capabilities. Therefore, it vital to work towards this problem. This is the general focus of this thesis. As, different mechanisms of charge storage exists in supercapacitors, which depends upon the material and electrolytes used, they are generally classified into carbon-based electric double capacitors and pseudocapacitors. Since different categories can exist in supercapacitors, the problem related to low energy densities in supercapacitors also needs to be resolved through different strategies. Therefore, among several problems, this chapter identifies, three major problems and provides a reasonable approach to tackle them. The first problem is related to the low values of capacitance in carbon-based double layer capacitors at high charging or discharging rates. The second problem is pointed towards the low nominal voltages in water-based pseudocapacitors. Whereas, the third problem is associated with the low values of capacitance in the material of a pseudocapacitor. All of these problems are either related to the low values of capacitance and/or the voltage of the supercapacitor. Since, the energy in a supercapacitor has a proportionality relationship to the capacitance and voltage, solving the above-mentioned problems could enhance the low energy densities of supercapacitors. Because

of this, general objectives are laid out for this thesis towards this direction, which is described in the next section.

1.5. General objectives of the thesis

Based on the problems described in **section 1.4** and their approach, the following are the three general objectives of this thesis:

- (i) *Is to fabricate electrode materials based on the 3-D architecture of the porous carbons and evaluate its material and electrochemical properties towards supercapacitor type energy storage.*
- (ii) *Is to demonstrate a full MXene cell based on 2-D Ti_3C_2 and $Mo_{2.7}V_{1.3}C_3$ MXene.*
- (iii) *Is to build a high-voltage pseudocapacitor cell based on non-carbon active materials with water-in-salt electrolytes and to evaluate its electrochemical properties.*

1.6. References

Abdollahifar, M. *et al.* (2018) 'High-performance carbon-coated $ZnMn_2O_4$ nanocrystallite supercapacitors with tailored microstructures enabled by a novel solution combustion method', *Journal of Power Sources*. Elsevier, 378, pp. 90–97. doi: 10.1016/j.jpowsour.2017.12.022.

Alhabeab, M. *et al.* (2017) 'Guidelines for Synthesis and Processing of Two-Dimensional Titanium Carbide ($Ti_3C_2T_x$ MXene)', *Chemistry of Materials*, 29(18), pp. 7633–7644. doi: 10.1021/acs.chemmater.7b02847.

Anasori, B. *et al.* (2015) 'Two-Dimensional, Ordered, Double Transition Metals Carbides (MXenes)', *ACS Nano*, 9(10), pp. 9507–9516. doi: 10.1021/acs.nano.5b03591.

Anasori, B., Lukatskaya, M. R. and Gogotsi, Y. (2017) '2D metal carbides and nitrides (MXenes) for energy storage', *Nature Reviews Materials*. Nature Publishing Group, 2(2), p. 16098. doi: 10.1038/natrevmats.2016.98.

Augustyn, V., Simon, P. and Dunn, B. (2014) 'Pseudocapacitive oxide materials for high-rate electrochemical energy storage', *Energy and Environmental Science*, 7(5), pp. 1597–1614. doi: 10.1039/c3ee44164d.

Avireddy, H. *et al.* (2016) *Effect of Various Binders on the Performance of Supercapacitor*

Electrodes, 4th International Symposium on Enhanced Electrochemical Capacitors. doi: 10.13140/RG.2.1.5080.6242.

Barsoum, M. W. (2000) 'MN_nAXN phases: a new class of solids; thermodynamically stable nanolaminates', *Progress in Solid State Chemistry*, pp. 201–281. doi: 10.1016/S0079-6786(00)00006-6.

Barsoum, M. W. (2013) *MAX phases: Properties of machinable ternary carbides and nitrides*, *MAX Phases: Properties of Machinable Ternary Carbides and Nitrides*. Edited by Wiley: Hoboken. doi: 10.1002/9783527654581.

Béguin, F. *et al.* (2014) 'Carbons and electrolytes for advanced supercapacitors', *Advanced Materials*, 26(14), pp. 2219–2251. doi: 10.1002/adma.201304137.

Bloom, C. O. (1975) 'A rate of approach to the steady state of solutions of second-order hyperbolic equations', *Journal of Differential Equations*, 19(2), pp. 296–329. doi: 10.1021/acs.nanolett.7b00533.

Borodin, O. *et al.* (2017) 'Liquid Structure with Nano-Heterogeneity Promotes Cationic Transport in Concentrated Electrolytes', *ACS Nano*, 11(10), pp. 10462–10471. doi: 10.1021/acsnano.7b05664.

Brousse, T. *et al.* (2017) 'Materials for Electrochemical Capacitors', in *Springer Handbook of Electrochemical Energy*. Berlin, Heidelberg: Springer Berlin Heidelberg, pp. 495–561. doi: 10.1007/978-3-662-46657-5_16.

Brousse, T., Bélanger, D. and Long, J. W. (2015) 'To Be or Not To Be Pseudocapacitive?', *Journal of The Electrochemical Society*, 162(5), pp. A5185–A5189. doi: 10.1149/2.0201505jes.

Chmiola, J. (2006) 'Supporting Material: Anomalous Increase in Carbon Capacitance at Pore Sizes Less Than 1 Nanometer', *Science*, 313(5794), pp. 1760–1763. doi: 10.1126/science.1132195.

Choi, D., Blomgren, G. E. and Kumta, P. N. (2006) 'Fast and reversible surface redox reaction in nanocrystalline vanadium nitride supercapacitors', *Advanced Materials*. John Wiley & Sons, Ltd, 18(9), pp. 1178–1182. doi: 10.1002/adma.200502471.

Conway, B. E. (2013) 'The Electrochemical Behavior of Ruthenium Oxide (RuO₂) as a Material for Electrochemical Capacitors', in *Electrochemical Supercapacitors*. Boston, MA: Springer US, pp. 259–297. doi: 10.1007/978-1-4757-3058-6_11.

Coustan, L., Shul, G. and Bélanger, D. (2017) 'Electrochemical behavior of platinum, gold and glassy carbon electrodes in water-in-salt electrolyte', *Electrochemistry Communications*, 77, pp. 89–92. doi: 10.1016/j.elecom.2017.03.001.

Crosnier, O. *et al.* (2018) 'Polycationic oxides as potential electrode materials for aqueous-based electrochemical capacitors', *Current Opinion in Electrochemistry*, 9, pp. 87–94. doi: 10.1016/j.coelec.2018.05.005.

Demarconnay, L., Raymundo-Piñero, E. and Béguin, F. (2010) 'A symmetric carbon/carbon supercapacitor operating at 1.6 v by using a neutral aqueous solution', *Electrochemistry Communications*, 12(10), pp. 1275–1278. doi: 10.1016/j.elecom.2010.06.036.

Dubouis, N. *et al.* (2018) 'The role of the hydrogen evolution reaction in the solid–electrolyte interphase formation mechanism for “ *Water-in-Salt* ” electrolytes', *Energy & Environmental Science*. The Royal Society of Chemistry, 11(12), pp. 3491–3499. doi: 10.1039/C8EE02456A.

Dyatkin, B. *et al.* (2016) 'Influence of Surface Oxidation on Ion Dynamics and Capacitance in Porous and Nonporous Carbon Electrodes', *Journal of Physical Chemistry C*. American Chemical Society, 120(16), pp. 8730–8741. doi: 10.1021/acs.jpcc.6b01204.

Feng, H. *et al.* (2016) 'Hierarchical structured carbon derived from bagasse wastes: A simple and efficient synthesis route and its improved electrochemical properties for high-performance supercapacitors', *Journal of Power Sources*. Elsevier, 302, pp. 164–173. doi: 10.1016/j.jpowsour.2015.10.063.

Fic, K. *et al.* (2012) 'Novel insight into neutral medium as electrolyte for high-voltage supercapacitors', *Energy Environ. Sci.* The Royal Society of Chemistry, 5(2), pp. 5842–5850. doi: 10.1039/C1EE02262H.

Forse, A. C. *et al.* (2016) 'New perspectives on the charging mechanisms of supercapacitors', *Journal of the American Chemical Society*. American Chemical Society, 138(18), pp. 5731–5744. doi: 10.1021/jacs.6b02115.

Forse, A. C. *et al.* (2017) 'Direct observation of ion dynamics in supercapacitor electrodes using in situ diffusion NMR spectroscopy', *Nature Energy*. Nature Publishing Group, 2(3), p. 16216. doi: 10.1038/nenergy.2016.216.

Gao, P. C. *et al.* (2015) 'Graphene-like carbide derived carbon for high-power supercapacitors', *Nano Energy*, 12, pp. 197–206. doi: 10.1016/j.nanoen.2014.12.017.

Gao, Q. *et al.* (2012) 'Exploring the large voltage range of carbon/carbon supercapacitors in aqueous lithium sulfate electrolyte', *Energy & Environmental Science*. The Royal Society of Chemistry, 5(11), p. 9611. doi: 10.1039/c2ee22284a.

Ghidiu, M. *et al.* (2015) 'Conductive two-dimensional titanium carbide “clay” with high volumetric capacitance', *Nature*. Nature Publishing Group, 516(7529), pp. 78–81. doi: 10.1038/nature13970.

Ghodbane, O., Pascal, J. L. and Favier, F. (2009) 'Microstructural effects on charge-storage properties in MnO₂-based electrochemical supercapacitors', *ACS Applied Materials and Interfaces*, 1(5), pp. 1130–1139. doi: 10.1021/am900094e.

Gogotsi, Y. and Penner, R. M. (2018) 'Energy Storage in Nanomaterials – Capacitive, Pseudocapacitive, or Battery-like?', *ACS Nano*, 12(3), pp. 2081–2083. doi:

10.1021/acsnano.8b01914.

Gogotsi, Y. and Simon, P. (2011) 'True performance metrics in electrochemical energy storage', *Science*. American Association for the Advancement of Science, 334(6058), pp. 917–918. doi: 10.1126/science.1213003.

Goodenough, J. B. and Kim, Y. (2010) 'Challenges for rechargeable batteries', *Chem. Mater.* American Chemical Society, 22(3), pp. 587–603. doi: 10.1016/j.jpowsour.2010.11.074.

Goodenough, J. B. and Park, K. S. (2013) 'The Li-ion rechargeable battery: A perspective', *Journal of the American Chemical Society*. American Chemical Society, 135(4), pp. 1167–1176. doi: 10.1021/ja3091438.

Goubard-Bretesché, N. *et al.* (2015) 'Nanocrystalline FeWO₄ as a pseudocapacitive electrode material for high volumetric energy density supercapacitors operated in an aqueous electrolyte', *Electrochemistry Communications*, 57, pp. 61–64. doi: 10.1016/j.elecom.2015.05.007.

Goubard-Bretesché, N., Crosnier, O., Buvat, G., *et al.* (2016) 'Electrochemical study of aqueous asymmetric FeWO₄/MnO₂ supercapacitor', *Journal of Power Sources*, 326, pp. 695–701. doi: 10.1016/j.jpowsour.2016.04.075.

Goubard-Bretesché, N., Crosnier, O., Favier, F., *et al.* (2016) 'Improving the Volumetric Energy Density of Supercapacitors', *Electrochimica Acta*, 206, pp. 458–463. doi: 10.1016/j.electacta.2016.01.171.

Griffin, J. M., Forse, A. C., Wang, H., Trease, N. M., Taberna, P. L., *et al.* (2015) 'Ion counting in supercapacitor electrodes using NMR spectroscopy', *Faraday Discussions*, 176, pp. 49–68. doi: 10.1039/c4fd00138a.

Griffith, K. J. *et al.* (2016) 'High-Rate Intercalation without Nanostructuring in Metastable Nb₂O₅ Bronze Phases', *Journal of the American Chemical Society*. American Chemical Society, 138(28), pp. 8888–8899. doi: 10.1021/jacs.6b04345.

Helmholtz, H. (1853) 'Ueber einige Gesetze der Vertheilung elektrischer Ströme in körperlichen Leitern mit Anwendung auf die thierisch-elektrischen Versuche', *Annalen der Physik*. John Wiley & Sons, Ltd, 165(6), pp. 211–233. doi: 10.1002/andp.18531650603.

Herrero, E., Buller, L. J. and Abruña, H. D. (2001) 'Underpotential deposition at single crystal surfaces of Au, Pt, Ag and other materials', *Chemical Reviews*. American Chemical Society, 101(7), pp. 1897–1930. doi: 10.1021/cr9600363.

Hope, M. A. *et al.* (2016) 'NMR reveals the surface functionalization of Ti₃C₂ MXene', *Phys. Chem. Chem. Phys.*, 18(7), pp. 5099–5102. doi: 10.1039/C6CP00330C.

Hu, M. *et al.* (2016) 'High-Capacitance Mechanism for Ti₃C₂T_x MXene by in Situ Electrochemical Raman Spectroscopy Investigation', *ACS Nano*, 10(12), pp. 11344–11350. doi: 10.1021/acsnano.6b06597.

Jäckel, N. *et al.* (2016) 'Increase in Capacitance by Subnanometer Pores in Carbon', *ACS Energy Letters*. American Chemical Society, 1(6), pp. 1262–1265. doi: 10.1021/acseenergylett.6b00516.

John Wang *et al.* (2007) 'Pseudocapacitive Contributions to Electrochemical Energy Storage in TiO₂ (Anatase) Nanoparticles'. American Chemical Society . doi: 10.1021/JPo74464W.

Kondrat, S. *et al.* (2014) 'Accelerating charging dynamics in subnanometre pores'. doi: 10.1038/NMAT3916.

Kondrat, S. *et al.* (2016) 'Pressing a spring: what does it take to maximize the energy storage in nanoporous supercapacitors?', *Nanoscale Horiz.* The Royal Society of Chemistry, 1(1), pp. 45–52. doi: 10.1039/C5NH00004A.

Kondrat, S. and Kornyshev, A. (2013) 'Charging Dynamics and Optimization of Nanoporous Supercapacitors', *The Journal of Physical Chemistry C*. American Chemical Society, 117(24), pp. 12399–12406. doi: 10.1021/jp400558y.

Kühnel, R. S. *et al.* (2016) "Water-in-salt" electrolytes enable the use of cost-effective aluminum current collectors for aqueous high-voltage batteries', *Chemical Communications*, 52(68), pp. 10435–10438. doi: 10.1039/c6cc03969c.

Kuo, S.-L. and Wu, N.-L. (2005) 'Electrochemical Capacitor of MnFe₂O₄ with NaCl Electrolyte', *Electrochemical and Solid-State Letters*. The Electrochemical Society, 8(10), p. A495. doi: 10.1149/1.2008847.

Laheäär, A. *et al.* (2015) 'Appropriate methods for evaluating the efficiency and capacitive behavior of different types of supercapacitors', *Electrochemistry Communications*. Elsevier B.V., 60, pp. 21–25. doi: 10.1016/j.elecom.2015.07.022.

Lannelongue, P., Le Vot, S., *et al.* (2018) 'Investigation of Ba_{0.5}Sr_{0.5}Co_xFe_{1-x}O_{3-δ} as a pseudocapacitive electrode material with high volumetric capacitance', *Electrochimica Acta*, 271, pp. 677–684. doi: 10.1016/j.electacta.2018.03.173.

Lannelongue, P., Bouchal, R., *et al.* (2018) "Water-in-Salt" for Supercapacitors: A Compromise between Voltage, Power Density, Energy Density and Stability', *Journal of The Electrochemical Society*, 165(3), pp. A657–A663. doi: 10.1149/2.0951803jes.

Largeot, C. *et al.* (2008) 'Relation between the ion size and pore size for an electric double-layer capacitor', *Journal of the American Chemical Society*, 130(9), pp. 2730–2731. doi: 10.1021/ja7106178.

Levi, M. D. *et al.* (2010) 'Electrochemical quartz crystal microbalance (EQCM) studies of ions and solvents insertion into highly porous activated carbons', *Journal of the American Chemical Society*. American Chemical Society, 132(38), pp. 13220–13222. doi: 10.1021/ja104391g.

Li, Y. *et al.* (2018) 'Design and Mechanisms of Asymmetric Supercapacitors', *Chemical Reviews*. American Chemical Society, 118(18), pp. 9233–9280. doi:

10.1021/acs.chemrev.8b00252.

Li, Z. *et al.* (2016) 'One-pot construction of 3-D nitrogen-doped activated graphene-like nanosheets for high-performance supercapacitors', *Electrochimica Acta*. Elsevier Ltd, 190, pp. 378–387. doi: 10.1016/j.electacta.2015.12.210.

Long, J. W. *et al.* (2002) ' Voltammetric Characterization of Ruthenium Oxide-Based Aerogels and Other RuO₂ Solids: The Nature of Capacitance in Nanostructured Materials ', *Langmuir*, 15(3), pp. 780–785. doi: 10.1021/la980785a.

Luan, Y. *et al.* (2015) 'A hierarchical porous carbon material from a loofah sponge network for high performance supercapacitors', *RSC Advances*. Royal Society of Chemistry, 5(53), pp. 42430–42437. doi: 10.1039/c5ra05688h.

Lukatskaya, M. R., Mashtalir, O., Ren, C. E., Dall'Agnese, Y., Rozier, P., Taberna, P. L., Naguib, M., Simon, P., Barsoum, M. W. and Gogotsi, Y. (2013) 'Cation intercalation and high volumetric capacitance of two-dimensional titanium carbide', *Science*. American Association for the Advancement of Science, 341(6153), pp. 1502–1505. doi: 10.1126/science.1241488.

Lukatskaya, M. R., Mashtalir, O., Ren, C. E., Dall'Agnese, Y., Rozier, P., Taberna, P. L., Naguib, M., Simon, P., Barsoum, M. W., Gogotsi, Y., *et al.* (2013) 'Cation Intercalation and High Volumetric Capacitance of Two-Dimensional Titanium Carbide', *Science*, 341(September), pp. 1502–1506. doi: 10.1557/mrc.2012.25.

Lukatskaya, M. R. *et al.* (2017) 'Ultra-high-rate pseudocapacitive energy storage in two-dimensional transition metal carbides', *Nature Energy*, 6. doi: 10.1038/nenergy.2017.105.

Lukatskaya, M. R., Dunn, B. and Gogotsi, Y. (2016) 'Multidimensional materials and device architectures for future hybrid energy storage', *Nature Communications*. Nature Publishing Group, 7, p. 12647. doi: 10.1038/ncomms12647.

Mendoza-Sánchez, B. *et al.* (2013) 'An investigation of nanostructured thin film α -MoO₃ based supercapacitor electrodes in an aqueous electrolyte', *Electrochimica Acta*, 91, pp. 253–260. doi: 10.1016/j.electacta.2012.11.127.

Merlet, C. *et al.* (2012) 'On the molecular origin of supercapacitance in nanoporous carbon electrodes', *Nature Materials*. Nature Publishing Group, 11(4), pp. 306–310. doi: 10.1038/nmat3260.

Merlet, C. *et al.* (2013) 'Highly confined ions store charge more efficiently in supercapacitors', *Nature Communications*. Nature Publishing Group, 4, p. 2701. doi: 10.1038/ncomms3701.

Meshkian, R. *et al.* (2018) 'W-Based Atomic Laminates and Their 2D Derivative W₁₋₃₃C MXene with Vacancy Ordering', 1706409, pp. 1–8. doi: 10.1002/adma.201706409.

Naguib, M. *et al.* (2011) 'Two-dimensional nanocrystals produced by exfoliation of Ti₃AlC₂', *Advanced Materials*. 2011/08/24, 23(37), pp. 4248–4253. doi: 10.1002/adma.201102306.

- Naguib, M. and Gogotsi, Y. (2015) 'Synthesis of two-dimensional materials by selective extraction', *Accounts of Chemical Research*, 48(1), pp. 128–135. doi: 10.1021/ar500346b.
- Peán, C. *et al.* (2015) 'Confinement, Desolvation, and Electrosorption Effects on the Diffusion of Ions in Nanoporous Carbon Electrodes', *Journal of the American Chemical Society*. UTC, 137(39), pp. 12627–12632. doi: 10.1021/jacs.5b07416.
- Peán, C. *et al.* (2014) 'On the dynamics of charging in nanoporous carbon-based supercapacitors', *ACS Nano*, 8(2), pp. 1576–1583. doi: 10.1021/nn4058243.
- Perez, A. J. *et al.* (2018) 'Proton Ion Exchange Reaction in Li_3IrO_4 : A Way to New $\text{H}_{3+x}\text{IrO}_4$ Phases Electrochemically Active in Both Aqueous and Nonaqueous Electrolytes', *Advanced Energy Materials*, 8(13), p. 1702855. doi: 10.1002/aenm.201702855.
- Prehal, C. *et al.* (2015) 'Tracking the structural arrangement of ions in carbon supercapacitor nanopores using in situ small-angle X-ray scattering', *Energy and Environmental Science*, 8(6), pp. 1725–1735. doi: 10.1039/c5ee00488h.
- Qie, L. *et al.* (2013) 'Synthesis of functionalized 3D hierarchical porous carbon for high-performance supercapacitors', *Energy and Environmental Science*, 6(8), pp. 2497–2504. doi: 10.1039/c3ee41638k.
- Richey, F. W. *et al.* (2014) 'Ionic liquid dynamics in nanoporous carbon nanofibers in supercapacitors measured with in operando infrared spectroelectrochemistry', *Journal of Physical Chemistry C*. UTC, 118(38), pp. 21846–21855. doi: 10.1021/jp506903m.
- Salanne, M. *et al.* (2016) 'Efficient storage mechanisms for building better supercapacitors', *Nature Energy*. Nature Publishing Group, 1(6), p. 16070. doi: 10.1038/nenergy.2016.70.
- Simon, P., Gogotsi, Y. and Dunn, B. (2014) 'Where do batteries end and supercapacitors begin?', *Science (New York, N.Y.)*. American Association for the Advancement of Science, 343(6176), pp. 1210–1. doi: 10.1126/science.1249625.
- Smith, L. and Dunn, B. (2015) 'Opening the window for aqueous electrolytes', *Science*, 350(6263), p. 918. doi: 10.1126/science.aad5575.
- Sudha, V. and Sangaranarayanan, M. V. (2002) 'Underpotential deposition of metals: Structural and thermodynamic considerations', *Journal of Physical Chemistry B*. American Chemical Society, 106(10), pp. 2699–2707. doi: 10.1021/jp013544b.
- Sun, G. *et al.* (2015) 'Three-dimensional hierarchical porous carbon/graphene composites derived from graphene oxide-chitosan hydrogels for high performance supercapacitors', *Electrochimica Acta*. Elsevier Ltd, 171, pp. 13–22. doi: 10.1016/j.electacta.2015.05.009.
- Suo, L. *et al.* (2015) "'Water-in-salt" electrolyte enables high-voltage aqueous lithium-ion chemistries', *Science*, 350(6263), pp. 938–943. doi: 10.1126/science.aab1595.

- Tao, Q. *et al.* (2017) 'Two-dimensional $\text{Mo}_{1.33}\text{C}$ MXene with divacancy ordering prepared from parent 3D laminate with in-plane chemical ordering', *Nature Communications*. 2017/04/26, 8, p. 14949. doi: 10.1038/ncomms14949.
- Tian, Z. *et al.* (2017) 'Superconcentrated aqueous electrolyte to enhance energy density for advanced supercapacitors', *Functional Materials Letters*, 10(06), p. 1750081. doi: 10.1142/S1793604717500813.
- Toupin, M., Brousse, T. and Bélanger, D. (2004) 'Charge storage mechanism of MnO_2 electrode used in aqueous electrochemical capacitor', *Chemistry of Materials*, 16(16), pp. 3184–3190. doi: 10.1021/cm049649j.
- Wang, L. *et al.* (2016) "Brick-and-mortar" sandwiched porous carbon building constructed by metal-organic framework and graphene: Ultrafast charge/discharge rate up to 2Vs^{-1} for supercapacitors', *Nano Energy*, 30, pp. 84–92. doi: 10.1016/j.nanoen.2016.09.042.
- Wu, J. *et al.* (2017) 'Selective Charging Behavior in an Ionic Mixture Electrolyte-Supercapacitor System for Higher Energy and Power', *Journal of the American Chemical Society*, 139(51), pp. 18681–18687. doi: 10.1021/jacs.7b10693.
- Wu, N. L. (2002) 'Nanocrystalline oxide supercapacitors', *Materials Chemistry and Physics*. Elsevier, 75(1–3), pp. 6–11. doi: 10.1016/S0254-0584(02)00022-6.
- Xu, Y. *et al.* (2014) 'Holey graphene frameworks for highly efficient capacitive energy storage', *Nature Communications*, 5. doi: 10.1038/ncomms5554.
- Yang, W. *et al.* (2017) 'Facile synthesis of nitrogen-doped porous carbon for high-performance supercapacitors', *RSC Advances*. Royal Society of Chemistry, 7(87), pp. 55257–55263. doi: 10.1039/c7ra11646b.
- Zhang, B. *et al.* (2016) 'Recent advances in electrospun carbon nanofibers and their application in electrochemical energy storage', *Progress in Materials Science*. Elsevier Ltd, 76, pp. 319–380. doi: 10.1016/j.pmatsci.2015.08.002.
- Zheng, J. P. (1995) 'Hydrous Ruthenium Oxide as an Electrode Material for Electrochemical Capacitors', *Journal of The Electrochemical Society*. The Electrochemical Society, 142(8), p. 2699. doi: 10.1149/1.2050077.
- Zhou, Q. *et al.* (2017) 'Fast charge rate supercapacitors based on nitrogen-doped aligned carbon nanosheet networks', *Electrochimica Acta*. Elsevier Ltd, 251, pp. 91–98. doi: 10.1016/j.electacta.2017.08.106.

Chapter 2:

Introduction to experimental methods

2.1. Introduction

The main objective of this chapter is to give a general understanding of the equipment and the characterization techniques used in this thesis. Section 2.1 introduces the electrospinning technique, whereas section 2.3 and 2.4 provides an overview of the material and electrochemical characterization, respectively.

2.2. Electrospinning

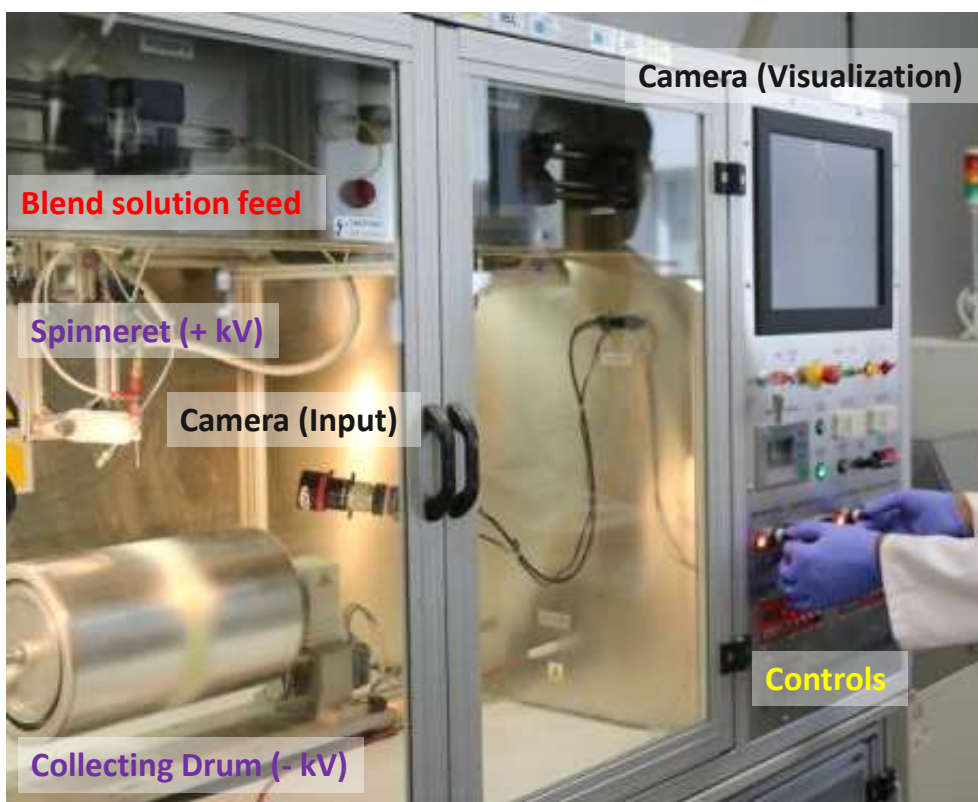


Figure 2. 1 Yflow® electrospinning equipment at IREC (Barcelona) which was used to fabricate polymer mats in this thesis

Electrospinning is a scalable technique to produce large quantities of 1-D nanofibers (NFs) by stretching and splitting the conducting polymers using high electric force. The typical electrospinning equipment consists of a syringe pump, a spinneret, and a collector. The syringe pump acts as a reservoir for the

polymer blend solution from which, under a controlled feed rate, the polymer solution is injected to the spinneret. Whereas, the spinneret acts as an ejecting source and is usually electrically connected to a high voltage source. **Figure 2.1** shows an example of the electrospinning unit, in which the above-mentioned components are labeled. The application of a high voltage leads to an introduction of an electrostatic force. The balance between this electrostatic force and surface tension leads to the formation of Taylor cone, a conical shape jet (jet based on the leaky dielectric model subjected to electrically conductive fluids) (Zhang *et al.*, 2016). The brief explanation of this model is discussed in the following paragraph. During electrospinning, when the process of jetting occurs in an electric field, the polymer blend solution possesses a transition zone, an example is shown in **figure 2. 2a**.

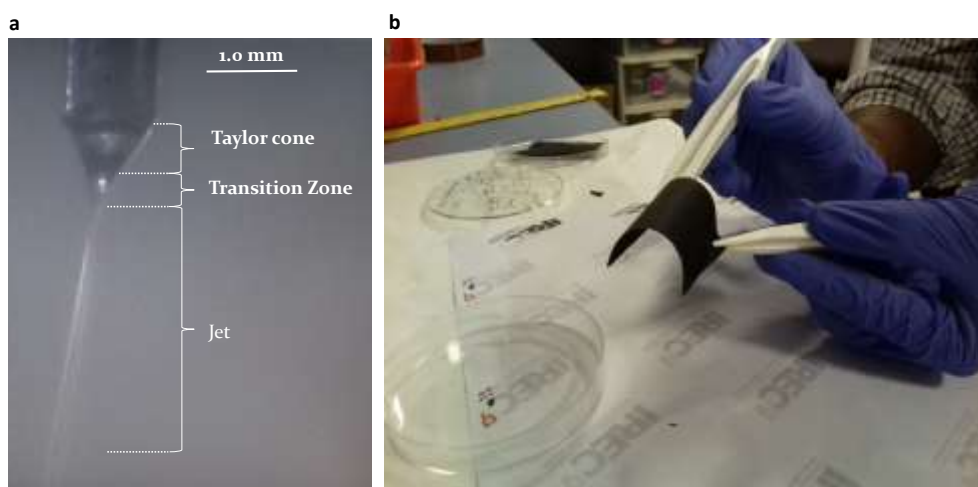


Figure 2. 2. (a) Visualization of the Taylor cone and jet formation through the camera. (b) Carbon nanofiber film after stabilization and carbonization process (Images obtained at IREC, Barcelona)

According to (Han, Yarin and Reneker, 2008), in this transition zone, a pre-stretching causes the electrically charged jet to induce a strain. Due to this, jets

faces viscoelastic stress in the longitudinal direction, which causes the jets to turn into thinner and thinner fibers and eventually resulting microfiber with diameters with micro- or nano-size. After the conical jet, the evaporation of the solvent begins which leads to increase in electrostatic repulsion forces between the charged jets resulting in the splitting of jets forming 1-D NFs (which are collected to an electrically connected ground). The formation of NFs and their physical characteristics depend upon the feed rate, the applied electric field and the distance between the spinneret and current collector. Apart from these, the diameter and length of NFs, strongly depends upon on the usage type of polymer. According to the review published by (Zhang *et al.*, 2016), some of the most common polymers, especially, for energy storage application point of view, can be divided into (a) guest and (b) host polymers. Some of the guest polymers such as Polystyrene and Poly (methyl methacrylate) act as a sacrificial phase and can be removed during thermal treatment. Whereas, host polymers such as Polyimide and Polyacrylonitrile (PAN) generally use as a scaffold. The electrospun NFs from these host polymers could be subjected to different thermal treatments to obtain CNFs. Among several host polymers, PAN is most widely used as a precursor for CNFs due to its excellent mechanical and high carbon yield. Electrospun PAN NFs typically requires a two-step thermal treatment process – (a) stabilization and (b) carbonization. According to (Rahaman, Ismail and Mustafa, 2007) and (Zhang *et al.*, 2016), stabilization is generally carried out in the air between 200°C to 280°C to process dehydrogenation and cyclization resulting in a continuous series connected C-N aromatic ring connected (in form of ladder structure). Dehydrogenation occurs through the elimination and oxidation of water leading to the formation of double bonds and adjacent groups react with nitrile groups to custom a ladder structure which thermally stable during carbonization [1]. The second step, namely carbonization, is carried out in an inert atmosphere to further grow the aromatic ring and to eliminate

heteroatoms (such as nitrogen). Complete removal of heteroatoms requires an additional thermal treatment high temperatures (of about 3000°C), also known as graphitization, to obtain graphitic carbon layers provides extremely high electrical conductivity to CNFs. However, graphitization could bring deteriorating effects resulting from the application of high temperatures and reduces the electrochemical performances (Zhang *et al.*, 2016). In addition to this, the presence of heteroatoms such as oxygen and nitrogen group could aid in providing an additional charge storage behavior which could also help in improving capacitance or capacity.

In chapter 3, electrospinning is used to fabricate carbon flexible electrode (both, CNFs and Fe-porous CNFs), as shown in *figure 2. 2b*. These electrodes were prepared using Nanotechnology Solutions from Yflow® electrospinning equipment at IREC (Barcelona). The details of the precursor and their modification and well as the control parameters of the electrospinning are described in the experimental section of *chapter 3*.

2.3. Material Characterization

2.3.1. X-Ray Diffraction (XRD)

The technique of X-Ray Diffraction (XRD) is used to study the compositional and crystallographic phase of the prepared materials. From the fundamental point of view, when a material (usually crystal) is exposed to an X-ray beam at different incident angles, a diffraction pattern is observed. As the wavelength of the X-rays is in the order of magnitude when compared to the interatomic distance of the crystal material, an elastic scattering between the beam light and electrons of the material generates interferences. These interferences are constructive, resulting in an increase of the intensity at specific angular positions. This variation of the intensity is seen as a diffraction pattern. Which, according to the Bragg's law occurs when the eq. (2.1) is satisfied.

$$2 d_{hkl} \sin(\theta) = n\lambda \quad (2.1)$$

In here, θ is the incident angle, λ is the X-ray wavelength, n is a positive integer number and d_{hkl} represents the inter-planar distances between the (h,k,l) miller planes. **In chapter 3**, XRD is used to identify the crystallographic phase of the prepared electrodes (both, CNFs and Fe-porous CNFs). With these materials, XRD measurements were obtained at IREC (Barcelona) by operating Bruker D8 advance with Cu. $K\alpha_1$ radiation ($\lambda=1.5405 \text{ \AA}$). The obtained XRD pattern was matched with crystallographic JCPDS database using the X'pert High Score (plus) software. In case of **chapter 4 and 5**, XRD measurements were carried out on a Rigaku Smartlab and a Rigaku MiniFlex (Tokyo) diffractometer using Cu $K\alpha_1$ ($\lambda=1.5405 \text{ \AA}$) radiation at Drexel University (Philadelphia, USA). *Dr. Bryan Byles* measured the XRD of the MnO_2 samples. Whereas, *Dr. Narendra Kurra* helped the corresponding author of this thesis to carry out the XRD measurement on the 2-D Ti_3C_2 MXene. It is noteworthy to mention that the interpretation of the results were carried out by the corresponding author of this thesis. For example, d-spacing of the 2-D Ti_3C_2 MXene was calculated to correlate with the electrochemical properties. Whereas, XRD pattern of different phases of MnO_2 was examined and as well as correlated with their electrochemical properties.

2.3.2. SEM

The technique of the Scanning Electron Microscopy (SEM) is used to gain information related to the morphology of the materials. On the operational point of view, SEM uses the concentrated beam of electrons on the material's surface and by recording the electrons coming from the materials, images can be generated. Backscattering and low energy secondary electrons are two common ways of collecting these oncoming electrons. For backscattering mode, detectors usually record the signal coming from the elastic scattering between the atoms of the sample and the electron beam. Whereas, low energy

secondary electrons record the electrons attributed to the impact point of the electron beam, which is later presented at different incident angles with respect to the sample morphology and this way images are also obtained. **In chapter 3**, FESEM from Zeiss Series Auriga was used at IREC to analyze the morphology of carbon nanofibers. Whereas, in the case of **chapter 5**, the morphology of the 2-D Ti_3C_2 MXene and MnO_2 were analyzed by Zeiss Supra 50VP, at Drexel University (Philadelphia, USA). *Dr. Babak Anasori* and *Dr. Bryan Byles* measured the SEM images of the 2-D Ti_3C_2 MXene and MnO_2 . However, the interpretation of results and their correlation was carried out by the corresponding author of the thesis.

2.3.3. Energy Dispersive X-ray Spectroscopy (EDS)

EDS allows to examine the chemical composition of the prepared materials, when it is exposed to an electron beam (usually with SEM), X-rays are emitted. These X-rays, in terms of the photon energy, depicts the specific electronic transition state of elements. This way, the atomic composition of the sample can be quantified. **In this thesis**, EDS is used to quantify the ratio between the cations inserted in the tunnel structure of the MnO_2 .

2.3.4. Transmission Electron Microscopy (TEM)

Unlike SEM, the beam of electrons in TEM is transmitted through the sample. The interaction between the given sample and the beam of electrons generates inelastic or elastic scattering. Depending upon the aim of the investigation, either inelastic or elastic scattering can be implemented to obtain the TEM images. Whereas, electron diffraction uses an elastic type of scattering. While spectroscopy techniques like Electron Energy Loss Spectroscopy (EELS) uses an inelastic type of scattering. In general, the electron beam of the TEM is focused on the samples by a condenser lens. This lens can be either in their converged or parallel form. A convergent beam is implied in case of the

Scanning mode of TEM (STEM), where the electron beam is moved along the sample for the recording the image. While a parallel beam is implied in the case of the conventional mode of TEM. In general, the obtained TEM images are the result of the signal recorded by which is measured either with the phase or amplitude contrast of the electrons. The phase contrast is shaped by the interference of more than one electron beam when it is fixated on the material. This approach gives more precision at the atomic scale, because of which high-resolution images can be obtained. Such images are usually referred to as high-resolution TEM images (or HR-TEM). Besides this, the examination of images using Fast-Fourier-Transformation (FFT) gives crystallographic details of the sample. In the case of amplitude contrast, bright or dark field mode of analysis can be conducted. In STEM mode, different signals are generated which are in fact dependent upon the solid angle position of the TEM detector. For example, the position of the solid angle with the Bright-Field (BF) detector is lower than 10 mrad. Whereas, an Annular-Dark-Field (ADF) detector have solid angles between 10 and 50 mrad. Although, further higher angles (> 50 mrad) can be also applied with the High-Angle-Annular-Dark-Field (HAADF) detector. It is noteworthy to mention that the chemical composition of the samples can be obtained through the HAADF detector, as it provides contrast proportional to the atomic number. Furthermore, spectroscopy analysis like EELS mapping can be achieved, when a mono-energetic electronic beam is focused on the material and the energy distribution analysis of the transmitted beam is recorded. **In chapter 3**, samples of carbon nanofibers were analyzed using the TEM technique. Samples for Transmission Electron Microscopy (TEM) were prepared by dispersing samples in hexane and collecting them on TEM copper grids. Scanning Transmission Electron Microscopy (STEM) and High-Resolution Transmission Electron microscopy (HRTEM) analysis was conducted by using an FEI Tecnai F20 field emission gun microscope operated at 200 kV with a point-to-point resolution of 0.19 nm, which is equipped with

Electron Energy Loss Spectroscopy (EELS) and Annular Dark Field (ADF) detectors. These analyses were carried out in collaboration with *Prof. Jordi Arbiol* of ICN2 (Barcelona). *Dr. Pengyi Tang* carried out the measurements and analyzed the data. The interpretation of the data and correlation with the other measurements were carried out the corresponding of this thesis.

2.3.5. Raman Spectroscopy

Raman spectroscopy examines the chemical forms of the materials by detecting the vibrations at the molecular level. From the fundamental point of view, a single frequency of radiation is implemented to irradiate the material and the scattering of this oncoming radiation is detected. This is why, Raman scattering is articulated as the wavenumbers (cm^{-1}), which is an energy shift of the exciting radiation. Raman scattering is highly sensitive to the symmetric covalent bonds and their change in their orientations. Since, carbon materials exhibit several folds of hybridization (sp^1 , sp^2 and sp^3) with several short, medium and long-range ordering (Dennison and Holtz, 1996; Hodkiewicz, 2010). Raman spectroscopy is generally used to detect these atomic ordering. *In chapter 3*, Raman spectra were used to detect the structural fingerprints of carbon nanofibers. The Raman spectra were recorded by using a Horiba Spectrometer HR800 (LabRAM Series, Horiba Jobin Yvon), which was located at the CCIiTUB (University of Barcelona).

2.3.6. Surface Area Analysis

Surface area analysis is vital to support the electrochemical properties of the electrode materials. These analyses are usually carried out below 1 bar (100 kPa) by adsorption of gases, like Nitrogen, Argon, etc., at cryogenic temperatures (eg. $\text{N}_2 = 77 \text{ K}$, $\text{Ar} = 87 \text{ K}$). According to (Thommes *et al.*, 2015), in general case of gas/solid systems, adsorption is termed as the enrichment of the ions or molecules at an interface of the solid. This interaction can occur either by

physical or chemical forms. In physical forms, which is also called as physisorption, an adsorbable gas is in contact with the surface of the material. Whereas, the formation of chemical bonds through intermolecular forces happens with the chemical type of interaction. This is termed as chemisorption. In the experimental point of view, onwards process of adsorption is followed by its converse, which is also called as desorption. These processes also indicate the direction in which experiments are taken place and are usually referred by their adsorption and desorption curves. For analysis, these curves are plotted with respect to a relative pressure (p/p_0^{-1}), in which p represents the equilibrium pressure, whereas p_0 is the saturation pressure

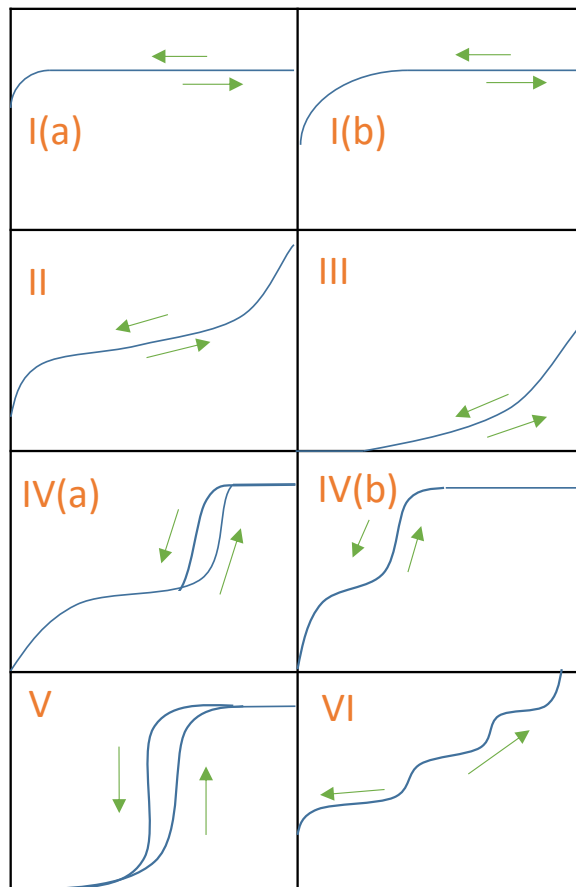


Figure 2. 3. Isotherms identified by IUPAC norms, figures drawn by the concept examined by (Thommes et al., 2015)

during the adsorption temperature. These plots are called as adsorption isotherms. It is noteworthy to mention that gas molecules can also enter in the bulk structure of the material, which is termed as absorption. Which, in most cases, is difficult to differentiate with the adsorption and therefore sorption term is also implied during the investigations. So, in certain cases, the reader can find the adsorption isotherms as sorption isotherms. According to the IUPAC norms, isotherms are identified into six types (see **figure 2.3**). Using these isotherms textural properties can be examined. In the context of the physisorption, IUPAC defines the size of the pores, as macropores (pores widths > 50 nm), mesopores (pores widths 2-50 nm) and micropores (< 2 nm). Such type of pore width and the mode of interaction with the gases could be identified by analyzing the type of isotherm. For example, the Type I isotherm indicates the presence of micropores materials, such as activated carbons. In this, Type I(a) depicts the narrow size micropores ($< \sim 1$ nm), while Type I(b) indicates wider size micropores or certain cases narrow mesopores ($< \sim 2.5$ nm). Type II isotherm demonstrates the unrestricted monolayer-multilayer adsorption, in which the point-B indicates the full adsorption of monolayers. Though, in Type III isotherm there is an absence of point A, which indicates relatively weak adsorption of gases molecules. Furthermore, the Type IV isotherm is generally seen in many oxides gels and industrial absorbents, consisting of mesopores. Once again, it is important to highlight that, in certain conditions, there is a mismatch between the adsorption and desorption curve, which causes hysteresis. This hysteresis is also useful to identify the type of mesopores. For instance, Type IV(a) isotherm implies mesopores with a narrow width (pores wider than ~ 4 nm), while Type IV(b) isotherm suggests cylindrical and conical mesopores. Besides this, Type VI isotherm is also observed with the materials consisting of non-uniform surfaces accompanying with layer-by-layer adsorption. Using the above isotherms, the surface area of the material can be measured. The Brunauer-Emmett-Teller method is

commonly implied. This method is applied in two stages: (i) transform the isotherm into BET plot and calculate the BET monolayer capacity (n_m), and (ii) area related to BET is calculated from n_m . For the first stage, the following equation can be used:

$$\frac{\frac{p}{p_0}}{n(1 - \frac{p}{p_0})} = \frac{1}{Cn_m} + \frac{C-1}{Cn_m} \left(\frac{p}{p_0}\right) \quad (2.2)$$

where n is the amount of adsorbed at a relative pressure (p/p_0). The n_m can be derived by plotting from the linear relationship between $\frac{\frac{p}{p_0}}{n(1 - \frac{p}{p_0})}$ and $\left(\frac{p}{p_0}\right)$, which is also called as BET plot. It is vital to note that the BET method is limited to Type II and Type IV isotherms and attention is needed in the presence of micropores, especially with Type I isotherm and combinations of Type I and IV and as well as the Type I and II, as it is challenging to separate the filling of the micropore and well as the monolayer-multilayer adsorptions. According to (Thommes *et al.*, 2015), the following procedure can be applied to avoid the subjective monolayer capacity:

- (i) C quantity in BET equation must be positive;
- (ii) BET equation should be restricted in the range when $n(1 - \frac{p}{p_0})$ increases in a continuous way with respect to $\left(\frac{p}{p_0}\right)$;
- (iii) The value of $\left(\frac{p}{p_0}\right)$ resultant to n_m must be within the chosen BET range.

Considering these above steps, the usual range for the relative pressure is ~ 0.05 to 0.30 . For the second stage, the BET method is applied to calculate the BET-area (a_s), which is derived by:

$$a_s(\text{BET}) = n_m \cdot L \cdot \frac{\sigma_m}{m} \quad (2.3)$$

Where σ_m is the average area occupied by the adsorbate gas. Furthermore, the pore size & volume distribution can also be achieved from the isotherms. Although, a general method like Barret-Joyner and Halenda (BJH) needs to be avoided with micropores, as BJH method underestimates the mesopores less 10 nm. In the case of microporous materials, molecular simulations and computational quantum mechanical modeling like Density Functional Theory (DFT) needs to be applied with a pore shape model (*eg.* cylindrical, spherical and slit).

In chapter 3, the porosity of the samples was obtained from the nitrogen sorption isotherms at 77 K. This instrument in this case of Micromeritics ASAP 2020 porosimeter and the measurements were carried out at IREC (Barcelona). The specific surface area of the samples was estimated by the BET plot of the adsorption isotherm, in which the range of the relative pressure is between ~0.05 to 0.30. The pore size distribution was obtained from the DFT model with an assumption of the cylindrical type of carbon pores. The measurements were done by *Marco Argudo*, who was responsible for the Micromeritics porosimeter. The corresponding author of this thesis, collected and analyzed the data.

2.3.7. Iodometric Titrations

Unlike, surface probing spectroscopy techniques, like the X-ray Photoelectron Spectroscopy (XPS), iodometric titration technique allows the user to measure the bulk Average Oxidation State (AOS) of the material. This way, the analysis allows the user to correlate the AOS data with the electrochemical measurements, as the electrode materials during the electrochemical measurements are in their bulk state. **In chapter 5**, iodometric titration was used to measure the AOS of the MnO₂ samples following the previous reports (*Vázquez-Vázquez et al.*, 1998; *Laiho et al.*, 2003) The measurements were carried out in collaboration with *Prof. Ekaterina Pomerantseva* of the Drexel

University (USA). In which, *Dr. Bryan Byles* carried out the iodometric titration measurements and calculated the AOS of the MnO_2 samples. The interpretation of the AOS data along with the electrochemical measurements was carried out by the corresponding author of this thesis. To keep the reader in the context of the investigation, the experimental procedure is explained in the following paragraph.

Briefly, ~10-15 mg of MnO_2 was dissolved in a mixed solution containing 20 mL of 0.06 M KI and 10 mL of 1M HCl, forming an amber-colored solution. The resulting solution was then titrated with a 0.2 N $\text{Na}_2\text{S}_2\text{O}_3$ solution until it became clear, with ~1 mL of starch solution added near the end of the titration as an indicator for verification that the titration was complete. The amount of Mn^{4+} and thus AOS of the MnO_2 samples could be then be calculated from the volume of titrant added. The general formula of the MnO_2 compounds studied here can be written as $\text{A}_x\text{Mn}_{1-\alpha}^{3+}\text{Mn}_\alpha^{4+}\text{O}_2$ (where A = Na or K), and α can be calculated from the Eq.:

$$\alpha = \frac{V * n * M}{m} \quad (2.4)$$

where V is the volume of titrated $\text{Na}_2\text{S}_2\text{O}_3$ solution, n is the normality of the $\text{Na}_2\text{S}_2\text{O}_3$ solution (0.2 N), M is the molar mass of the MnO_2 sample, and m is the mass of the MnO_2 sample in solution.

2.3.8. Electrical Measurements

The electrical conductivity can be obtained by the reverse of the resistivity, which can be measured through four-probe configuration. **In chapter 3**, the four-probe test equipment (EverBeing SP4) was used to measure the electrical conductivity of the prepared fiber electrodes. The experiments were conducted with the help of *Dr. Jordi Jacas Biendicho* at IREC (Barcelona). Four finger contact electrodes were put within a distance of 4 mm and in-plane resistance was measured in the parallel direction of the rotating current collector of the

fiber electrodes. The in-plane resistivity was measured using anisotropic Van der Pauw method (Price, 1972). No compressive force and change of temperatures were applied for the fiber electrodes.

2.4. Electrochemical characterization

2.4.1. Electrochemical Apparatus

The electrochemical workstation is one of the main apparatus. It is composed of a signal waveform generator, computer, and galvanostat/potentiostat. In this work, a VMP-3 potentiostat/galvanostat from Biologic (France) was used as an electrochemical workstation. With these workstations, the user defines the requisite parameters in the computer, which is later instructed to the block composed of the signal waveform generator. Later on, the output from this block is applied to an electrochemical cell. In this thesis, two configurations were used, namely a two-electrode and the three-electrode cell. **Figure 2.4 a** shows the general schematic of these two configurations. The current is flown through the Working-Electrode (WE) and Counter-Electrode (CE), whereas, the voltage is controlled or measured between the Reference-Electrode (RE) and WE. In the case of the three-electrode configuration, the RE has a stable and well-known electrochemical potential. Because of which, WE can be accurately controlled or measured. Besides this, metals such as gold and silver wires can be also used as RE. Such REs are implemented based on the three-electrode cell provider or depending upon the compatibility between the RE and the used electrolyte solution for the electrochemical analysis. However, these REs are termed as pseudo-references (pseudo-RE), as their potential changes depending upon the type of the electrolyte solution. Therefore, it is important to measure the electrochemical potential of the pseudo-RE versus a standard RE before the analysis. Unlike three-electrode cell configuration, in two-electrode cell configuration, the controlled or measured voltage is the voltage of the electrochemical cell, as the RE and the CE are shorted. **This**

thesis uses both the two-electrode and three-electrode cell configuration to determine the electrochemical characterization of the prepared electrodes. **In chapter 3**, the EL-cell was used as a three-electrode cell configuration. In such a case, a gold wire is used as a pseudo-RE (Maksymiuk *et al.*, 2013). Whereas, during the two-cell configuration measurements, a T-shape Swagelok cell with a body polytetrafluoroethylene (PTFE) polymer is used. Besides this, in **chapter 4** and **5** of this thesis, Saturated Calomel Electrode, and Silver Chloride Electrode, respectively, were used as a RE in the three-electrode cell configuration. In both two- and three-cell configurations, several transient, and stationary techniques can be used for the analysis. The brief description of these techniques is in the following sections.

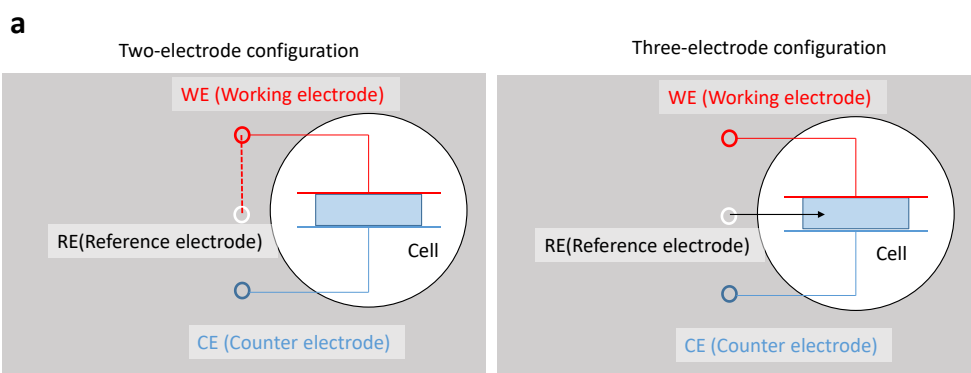


Figure 2. 4 (a) Two- and three-electrode electrochemical cell configuration.

2.4.2. Transient Techniques: Cyclic Voltammetry (CV) and Galvanostatic charge and discharge (GCD)

The transient technique allows the users to follow the variable parameters, like current and voltage variation. Following are the transient techniques by which the user can use in their electrochemical investigations.

Cycling voltammetry (CV): In this thesis, CV is used when the investigation requires the following features to be determined:

1. Electrochemical potential stability window,

2. Qualitative and pseudo-qualitative behavior,
3. Rate-capability (Value of capacity or capacitance over the scan rate),
4. Long term stability (Value of capacity or capacitance over a number of cycles).

In a CV (Elgrishi *et al.*, 2018), a linear ramp of the potential is applied to the WE. The potential is usually varied between the minimum and maximum electrochemical window of the electrode material. In such cases, the potential given at a certain point can be represented as:

$$E = E_o - vt, \text{ when } E \geq E_1 \quad (2.5)$$

$$E = E_o + vt, \text{ when } E \leq E_2 \quad (2.6)$$

where E_o (V) is the potential at the starting position, v is the scan rate ($V s^{-1}$), E_1 and E_2 are the minimum and maximum potential limits, respectively. Using the CV, the charge type of the electrode system can be predicted. For example, when the redox materials store charges based on the redox reaction, the CV curve can be significantly characterized by reversible current peaks. Whereas, for a non-faradaic reaction like the ideal case of double-layer capacitance, the observed current in the CV curve is constant at a given potential (*See figure 2.5*). However, in practical applications, the resistance with the electrode material distorts the ideal capacitive (rectangular) behavior (*See figure 2.5*). It is noteworthy that the several materials also exhibit multiple redox reactions within the electrochemical potential window, which convolutes close to a

rectangular-like CV curve. In **chapter 3, 4 and 5**, CV is used to distinguish the capacitive behavior of the electrodes materials.

Galvanostatic charge and discharge (GCD): In this thesis, GCD is used when the investigation requires the following features to be determined:

1. Electrochemical potential stability window,

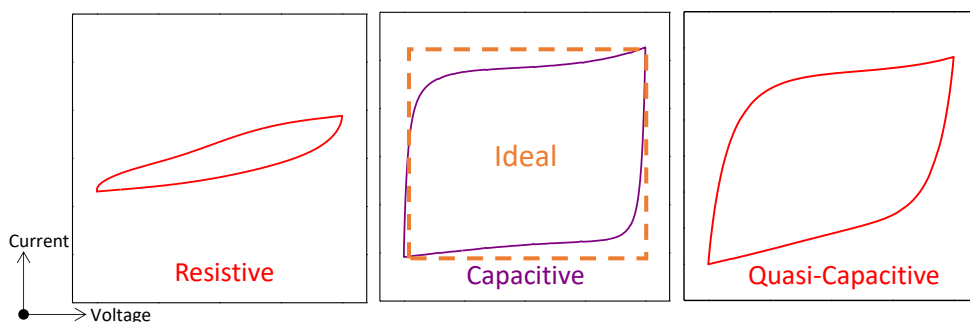


Figure 2. 5. Depiction of CV curve in an electrochemical supercapacitor. Left, indicates the case with electrodes with high resistance; Middle, indicates ideal and real case of the capacitive behavior (eg. CNFs//CNFs cell in 6 M of potassium hydroxide electrolyte, CV at a scan rate of 1000 mVs^{-1}); Right, indicates the case of the quasi-behavior. Units= a.u

2. Long term stability (Value of capacity or capacitance over the number of cycles).

The ideal response of the capacitor is shown in **figure 2.6**, which indicates that the potential varies linearly when the electrode material is discharged or charged. This behavior can be given as:

$$V(t) = Ri + \frac{t}{C}i \quad (2.7)$$

where R is the resistance (Ohm), i is the applied current in (Ag^{-1}), C (F) is the capacitance and t (s) is the time required to charge and discharge. Both CV and GCD can be used to determine the electrochemical stability in terms of the capacity or capacitance retention over cycling. In **chapter 4 and 5**, GCD is used to determine the electrochemical stability of the electrode materials. Nevertheless, Both CV and GCD techniques are limited when the quantitative electrochemical analysis, like the separation between the kinetic and diffusion controlled process, is required. Therefore, stationary techniques like electrochemical impedance spectroscopy are needed. The description of these techniques is in the following paragraph.

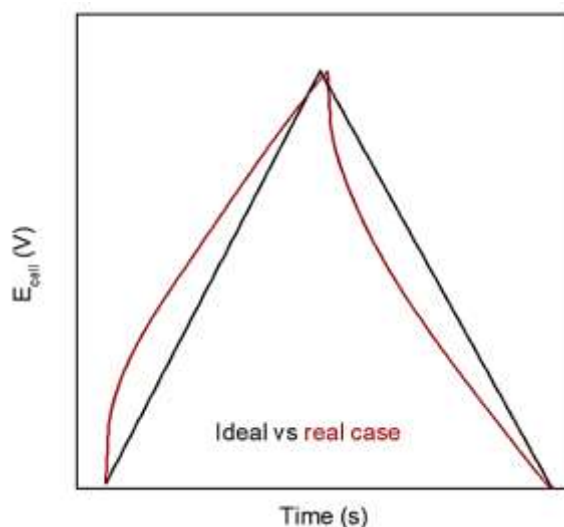


Figure 2. 6. GCD curve of an electrochemical supercapacitor, depicting the ideal vs real case (eg. $\text{Ti}_3\text{C}_2/\text{MnO}_2$ cell in 21 m of potassium acetate electrolyte, GCD at a current density of 0.5 Ag^{-1}). Units= a.u

2.4.3. Stationary Techniques: Electrochemical Impedance spectroscopy

Electrochemical impedance spectroscopy (EIS) uses an AC signal over a different range of frequencies, which can be used to determine the impedance (Z) of the electrochemical cell or the electrode material used in the electrochemical cell. Since, the behavior of the electrochemical processes has dependence to the applied frequencies, the variation of the impedance along

with the frequency can be used to separate the electrochemical behavior of the electrode materials or the supercapacitor cells. Because of this, studies need to be complimented along with the CV and GCD measurements. In general, during the EIS analysis, a sinusoidal potential or current is applied. The signal of this applied potential can be given as:

$$V(\omega) = V_o \sin(\omega t) \quad (2.8)$$

Whereas, the signal of the current can be given as:

$$I(\omega) = I_o \sin(\omega t + \phi) \quad (2.9)$$

In these equations, V and I are considered as the applied potential (V) and current (A), respectively. These signals are independence with the angular frequency of ω (rad s⁻¹). Also, V_o and I_o in the above equations are the amplitude of the applied potential and current, respectively. Besides these terms, in here, ϕ represents the phase angle, which is in-fact the lag between the current response and the applied potential. The magnitude of the impedance ($|Z|$) is defined as the complex vector of the capacitive and resistive impedances. $|Z|$ can be represented as:

$$|Z(\omega)| = \frac{V_o}{I_o} \exp(-i \phi) \quad (2.10)$$

Since it is in the complex vector format, the $|Z(\omega)|$ can be separated into its real $Z'(\omega)$ and imaginary $Z''(\omega)$ parts, as:

$$Z(\omega) = Z'(\omega) - i Z''(\omega) \quad (2.11)$$

Where $Z'(\omega)$ and $Z''(\omega)$ are:

$$Z'(\omega) = R \text{ (resistive contribution)} \quad (2.12)$$

$$Z''(\omega) = \frac{1}{\omega C} \text{ (capactive contribution)} \quad (2.13)$$

This $Z(\omega)$ allows the users to distinguish different electrochemical processes at applied frequencies (Barsoukov and Macdonald, 2005). The impedance of the electrochemical cell can be described into an equivalent circuit (an

electrical circuit). The equivalent circuit of an ideal supercapacitor is composed of a resistor and capacitor element in a series connection. These elements are represented as the series resistance (R_s) and double layer capacitance (C_{DL}). And, using the different frequencies during the EIS measurements, these two features can be separated. For example, at high frequencies (>200 kHz), the impedance related to the C_{DL} has no contributions and therefore the total value of the impedance $Z(\omega)$ would be related to the $Z'(\omega)$. Since the value of $Z'(\omega)$ is solely related to the resistance, the value of $Z'(\omega)$ at high frequencies can be considered as the R_s . Whereas, at low frequencies (like 10 mHz), only C_{DL} is finite and therefore the total value of the impedance is related to $Z''(\omega)$. And, since the value of $Z''(\omega)$ is the inverse of capacitance, from eq. 2.13. The value of C_{DL} can be acquired at low frequencies (10 mHz).

Equivalent Distributed Resistances (EDR): In reality, the electrode of the ELDC behaves in a much more complex way. The factors like porosity and roughness of the electrode and as well the contact with the current collector plays a vital role. These factors also show their influence with the variation of the frequencies and in-turn the electrical parameters in the equivalent circuit. For example, the model proposed by Levie indicates that the porous carbon electrodes can be designated with the transmission model (Béguin and Frackowiak, 2013), which consists of several RC constants, as shown by **figure 2.7**. This can be represented as:

$$Z_p = \sqrt{R_p Z_E} \operatorname{coth} (R_p Z_E) \quad (2.14)$$

Where Z_p is the impedance of the electrode's porosity, Z_E with the interface impedance between the electrolyte/electrode and R_p with the ionic resistance of the electrode material. Furthermore, with the consideration of the series resistance in the eq. 2.14, the total impedance of the electrode or device can be depicted, which can be written as:

$$Z_{SC} = R_s + Z_E \quad (2.15)$$

With this equation, the ability of the electrolyte penetration within the carbon pores and related resistance can be examined. This information can be achieved due to the fact of the electrolyte ions interact differently with the applied frequencies. For example, when high frequencies are applied during the EIS measurements, only the external surface of the electrode and the large size pores interacts with the electrolyte-ions. Whereas, this interaction reaches at the deeper sites of the carbon pores when frequencies are decreased. This interaction behavior is in-fact linked with *electrolyte-ion penetration* or can be deliberate as the exchange of electrolyte-ions with the bulk liquid electrolyte and the carbon pore. This interaction can be also quantified into resistance by analyzing the EIS data in the Nyquist plot.

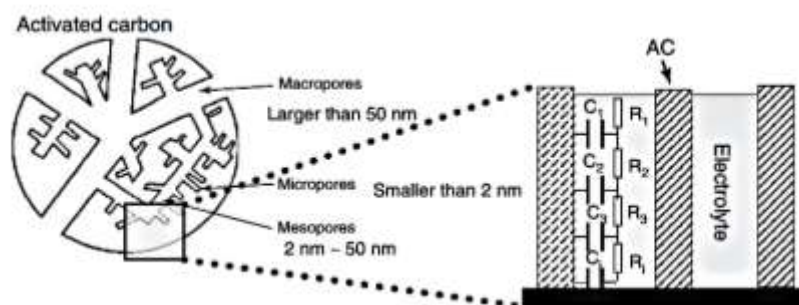


Figure 2. 7. Schematic illustration of the porous carbon electrode, figure reproduced from (Béguin and Frackowiak, 2013) with permission from John Wiley and Sons.

Nyquist plot is a Cartesian coordinate of the real and imaginary Impedance. An example of this plot for a porous electrode is shown in **figure 2.8**. In this plot, the first intercept on the real axis is the equivalent series resistance (ESR) of the device. Whereas, the delimiting sloppy region followed by near vertical line region depicts the *knee frequency* (Taberna, Simon and Fauvarque, 2003; Barsoukov and Macdonald, 2005). This knee frequency is a transition state-of-charge in which there is a full access to the electrolyte penetration region (or electrolyte exchange) and the electrode surface. The tangential intersection of the delimiting sloppy region on the real axis (X-axis in the Nyquist plot), which appears after knee frequency, leads to a value of resistance. This value is the combination of series resistances and resistances related to the penetration of the electrolyte ions. Deducing this value with the series resistance (first intercept at high frequency in the Nyquist plot) indicates the resistance of the electrolyte-ion penetration or the exchange of electrolyte-ions between the

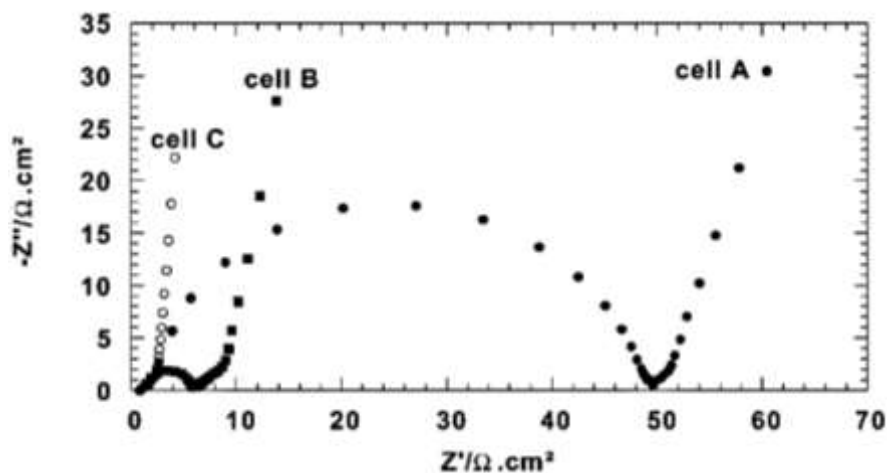


Figure 2. 8. Nyquist plot obtained from PEIS measurements with activated carbon electrodes based supercapacitor cell. Figure reproduced from (Portet et al., 2004) with permission from Elsevier. In here, influence of the aluminum current collector in Nyquist plot is shown. The cell A, represents with the as received aluminum current collector; cell B, represents with the electrochemically aluminum current collector; cell C, represents the modified aluminum current collector (conductive sol-gel coated + electrochemically etched).

bulk-liquid electrolyte and the pore (Barsoukov and Macdonald, 2005; Gao *et al.*, 2015; Dyatkin *et al.*, 2016). This resistance is also identified as the Equivalent Distributed Resistances (EDR). It is noteworthy to mention that, in cells and the devices, the resistances originated due to the contact of the electrode with the current collector can be usually seen as a semi-circular loop (also known as charge-transfer resistance). An example of such a phenomenon is shown in **figure 2.8**. And, therefore, the EDR also effects the electrolyte-ion penetration or exchange of electrolyte-ions and in-turn the electrochemical performances of the materials. **Chapter 3** uses the Potentiostatic mode of EIS (PEIS) to analyze the EDR of the prepared materials. In those experiments, the PEIS was carried out at open circuit voltage (OCV) with an amplitude of 5 mV s⁻¹. The range of frequencies for this set of experiments was from 200 kHz to 10 mHz. Besides this PEIS was also used to quantify the relaxation time constant of the cells. **In chapter 4**, phase angle measurements at low frequency (10 mHz) using PEIS was also used to distinguish the electrochemical processes.

Relaxation time constant: Relaxation time constant is considered as a merit factor for electrochemical supercapacitors, as it defines minimum time to discharge the full energy of an EDLC cell with efficiency > 50 % (Taberna, Simon and Fauvarque, 2003). Also, the frequency related to this relaxation time constant is the bandwidth in which the supercapacitor cell can be integrated into an electrical circuit. The relaxation time constant can be analyzed by plotting the complex capacitance plots, using the available impedance data. The frequency dependence of the real ($C'(\omega)$) and imaginary $C''(\omega)$ parts of the capacitance can be obtained from the electrochemical impedance spectroscopy measurements, by using the following equations (Taberna, Simon and Fauvarque, 2003):

$$C'(\omega) = \frac{-Z''(\omega)}{\omega|Z(\omega)|^2} \quad (2.16)$$

$$C''(\omega) = \frac{-Z'(\omega)}{\omega|Z(\omega)|^2} \quad (2.17)$$

The relaxation time constant (τ_0) can be obtained by measuring the frequency (f_0) when the $C''(\omega)$ reaches a maximum value in the plot of $C''(\omega)$ versus applied frequency. Using this measured f_0 , the time constant can be derived as $\tau_0 = 1/f_0$. This method of analysis was also used in **chapter 3** for determining the relaxation time constant of the cells.

2.4.4. Self-discharge analysis

The fade of voltage in supercapacitor after a full charge is termed as the self-discharge (Andreas, 2015). Self-discharges in supercapacitors are usually quick and three-quarters of the energy is delivered when the device reaches the first half of its voltage. Because of this, supercapacitors usually fails to meet the energy requirements of the electronic or electrical circuit in which it is placed. This is one of the reasons why supercapacitors need to be charged at frequent intervals with a constant current to maintain its fully charged state. So far, the origin of self-discharges has been identified as parasitic Faradaic reactions, charge re-distribution and ohmic leakage. Parasitic Faradaic reactions are observed when the cells are operated beyond the working electrochemical potential windows of its electrode materials and as well as the electrochemical stability windows of its liquid electrolyte. Besides this, operating the cell beyond these limits not arises parasitic Faradaic reactions but also degrades the lifetime of the cell. Therefore, operating the electrochemical cells within the safer is vital. For ohmic leakage, is generally arisen due to the fault in the assembly of the electrochemical cell, either resistive passive layer on the current collectors in which electrode materials are placed or resistive pathway connection between the positive and negative electrodes. Lastly, self-discharge due to the charge re-distribution originates due to electronic/ionic resistance of the materials and interaction of the electrolyte ions with the electrode materials (eg. electrolyte resistance in carbon pores for EDLCs). This type of

self-discharge is the main concern and limits the application of the supercapacitors as a self-sufficient energy storage device and therefore, it is vital to resolve the problem of self-discharge. In reality, certain materials, especially with pseudocapacitive properties exhibit the combination of both Faradaic reaction and charge re-combination type of self-discharge. It is noteworthy to mention that the Faradaic reaction and parasitic Faradaic reaction are two different processes. The prior term is related to the valence state of the electrode material (eg. MnO_2), while, the later one is either related to the decomposition of the material and electrolyte due to the non-safer operational limits of the cell voltages. Since a mix of both Faradaic reaction and charge re-combination type of self-discharges happens, it is difficult to adequate a self-discharge charge model. The analysis gets even more challenging in the cases when the investigation hold newly developed materials or when they are combined with new electrolyte formulations. However, an inspection of self-discharges between two different supercapacitor system is to observe the diffusion-controlled processes through the mathematical equations. For instance, self-discharges limited by the diffusion processes usually exhibits a linear relationship, when the potential or voltage is plotted versus the square root of the self-discharge time. This can be also represented by the Convey modified Fick's law, which is given as:

$$V_t = V_i - \frac{2 z F A D^{1/2} \pi^{-1/2} c_0}{C} t^{1/2} \quad (2.18)$$

where z , c_0 and D are the charge, initial concentration and charge diffusion coefficient of the reacting species, V_i is the initial voltage of charging and A is electrode area.

In chapter 5, the concept of the linear relationship between the voltage and the square root of the self-discharge time is implied to compare self-discharges behavior between the asymmetric YP-50//YP- 50 and Ti_3C_2 // α - MnO_2 cell. Self-

discharges in $\text{Ti}_3\text{C}_2//\alpha\text{-MnO}_2$ and YP-50//YP-50 cell were evaluated by measuring the open circuit voltage of cell after being charged to its optimum voltage at a current density of 10 mA g^{-1} , holding cell voltage for 2 h and then releasing the voltage. For the self-discharge investigation of Ti_3C_2 and $\alpha\text{-MnO}_2$ electrodes in the asymmetric cell $\text{Ti}_3\text{C}_2//\alpha\text{-MnO}_2$ configuration, the electrochemical potentials of Ti_3C_2 and $\alpha\text{-MnO}_2$ electrodes were examined with reference to SCE.

2.4.5. Methods of calculation for supercapacitor performance

In general, the capacitance, C (F) is calculated as:

$$C = \left(\frac{1}{v \cdot V} \right) \int_{V^-}^{V^+} I(V) dV, \quad (2.19)$$

where V (V) is the potential and v (mV s^{-1}), the scan rate. V_+ and V_- is the value of vertex potential in the electrochemical window, respectively. I (mA) is the current response to the applied voltage, in the cyclic voltammetry technique. The capacity (mAh) is calculated as:

$$\text{Capacity} = \frac{C \cdot V}{3.6} \quad (2.20)$$

Specific capacitance (F g^{-1} or F cm^{-3}) or capacity (mAh g^{-1} or mAh cm^{-3}) was calculated by dividing the Eq. (3) or (4), respectively, either by mass (g) or geometrical volume (cm^3) of the electrodes. For the full cell, volume or weight of both electrodes (positive and negative) were considered. The thickness of the membrane was not taken into account while measuring the volumetric performance. In several cases, the CV curves of the supercapacitor (both electrode or/and cell) can show non-rectangular behavior, which can be either originated because of the redox reaction or combinations of redox reaction and EDLC. In such cases (Laheäär *et al.*, 2015), charge or capacity (Q , C g^{-1} or mAh g^{-1}) needs to be considered for the calculation of the charge stored in the electrode material. **In chapter 3-5**, CV curves were used to calculate the

capacitance of prepared electrodes materials. It is noteworthy to mention that in order to compare the values of the capacitance of the prepared electrodes with existing literature, calculation of the single electrode capacitance was taken into account in the two-electrode configuration. In such cases, to obtain the single electrode specific capacitance, the factor of 4 is multiplied with the specific cell capacitance.

2.5. Conclusions

In this chapter, basics understanding of the techniques were presented and brief information about the use of the above techniques in the following chapters.

2.6. References

Andreas, H. A. (2015) 'Self-Discharge in Electrochemical Capacitors: A Perspective Article', *Journal of The Electrochemical Society*, 162(5), pp. A5047–A5053. doi: 10.1149/2.0081505jes.

Barsoukov, E. and Macdonald, J. R. (2005) *Impedance spectroscopy : Theory, Experiment, and Applications*. Second edi. Edited by E. Barsoukov and J. R. Macdonald. New Jersey, USA: John Wiley & Sons, Inc., Hoboken, New Jersey.

Béguin, F. and Frackowiak, E. (2013) *Supercapacitors: Materials, Systems, and Applications*, Wiley-VCH Verlag. doi: 10.1002/9783527646661.

Dennison, J. R. and Holtz, M. (1996) 'Raman Spectroscopy of carbon materials', *Spectroscopy*, 11(8), pp. 38–45. doi: 10.1002/9783527610426.bardo30306.

Dyatkin, B. *et al.* (2016) 'Influence of Surface Oxidation on Ion Dynamics and Capacitance in Porous and Nonporous Carbon Electrodes', *Journal of Physical Chemistry C*. American Chemical Society, 120(16), pp. 8730–8741. doi: 10.1021/acs.jpcc.6b01204.

Elgrishi, N. *et al.* (2018) 'A Practical Beginner's Guide to Cyclic Voltammetry', *Journal of Chemical Education*, 95(2), pp. 197–206. doi: 10.1021/acs.jchemed.7b00361.

Gao, P. C. *et al.* (2015) 'Graphene-like carbide derived carbon for high-power supercapacitors', *Nano Energy*, 12, pp. 197–206. doi: 10.1016/j.nanoen.2014.12.017.

Han, T., Yarin, A. L. and Reneker, D. H. (2008) 'Viscoelastic electrospun jets: Initial

stresses and elongational rheometry'. doi: 10.1016/j.polymer.2008.01.035.

Hodkiewicz, J. (2010) *Characterizing Carbon Materials with Raman Spectroscopy*, Thermo Fisher Scientific.

Laheäär, A. *et al.* (2015) 'Appropriate methods for evaluating the efficiency and capacitive behavior of different types of supercapacitors', *Electrochemistry Communications*. Elsevier B.V., 60, pp. 21–25. doi: 10.1016/j.elecom.2015.07.022.

Laiho, R. *et al.* (2003) 'Low-field magnetic properties of $\text{LaMnO}_{3+\delta}$ with $0.065 \leq \delta \leq 0.154$ ', *Journal of Physics and Chemistry of Solids*. Pergamon, 64(12), pp. 2313–2319. doi: 10.1016/S0022-3697(03)00266-X.

Maksymiuk, K. *et al.* (2013) *Handbook of reference electrodes*, Springer. doi: 10.1007/978-3-642-36188-3_5.

Portet, C. *et al.* (2004) 'Modification of Al current collector surface by sol-gel deposit for carbon-carbon supercapacitor applications', *Electrochimica Acta*, 49(6), pp. 905–912. doi: 10.1016/j.electacta.2003.09.043.

Price, W. L. V (1972) 'Extension of Van der Pauw's theorem for measuring specific resistivity in discs of arbitrary shape to anisotropic media', *Journal of Physics D: Applied Physics*, 5(6), pp. 1127–1132. doi: 10.1088/0022-3727/5/6/315.

Rahaman, M. S. A., Ismail, A. F. and Mustafa, A. (2007) 'A review of heat treatment on polyacrylonitrile fiber', *Polymer Degradation and Stability*. Elsevier, 92(8), pp. 1421–1432. doi: 10.1016/j.polymdegradstab.2007.03.023.

Taberna, P. L., Simon, P. and Fauvarque, J. F. (2003) 'Electrochemical Characteristics and Impedance Spectroscopy Studies of Carbon-Carbon Supercapacitors', *Journal of The Electrochemical Society*. The Electrochemical Society, 150(3), p. A292. doi: 10.1149/1.1543948.

Thommes, M. *et al.* (2015) *Physisorption of gases, with special reference to the evaluation of surface area and pore size distribution (IUPAC Technical Report)*, *Pure and Applied Chemistry*. doi: 10.1515/pac-2014-1117.

Vázquez-Vázquez, C. *et al.* (1998) 'Characterization of $\text{La}_{0.67}\text{Ca}_{0.33}\text{MnO}_{3+\delta}$ particles prepared by the sol-gel route', *Journal of Materials Chemistry*. The Royal Society of Chemistry, 8(4), pp. 991–1000. doi: 10.1039/a707226k.

Zhang, B. *et al.* (2016) 'Recent advances in electrospun carbon nanofibers and their application in electrochemical energy storage', *Progress in Materials Science*. Elsevier Ltd, 76, pp. 319–380. doi: 10.1016/j.pmatsci.2015.08.002.

Chapter 3:

**3-D electrospun Fe/Fe₂O₃
porous carbon nanofibers as
electrode materials for High-
rate supercapacitors**

3.1 Introduction

As highlighted in the section 1.4.1 of this thesis (*see chapter 1*), binder-based porous carbon electrode suffer from low effective utilization of the electrolyte ions. This makes the binder-based electrode to suffer from low values of capacitance at high rates. Besides highlighting this problem in section 1.4.1, it was also proposed that the approach of designing a porous carbon-based electrode with a 3-D architecture might resolve the problem faced with binder-based carbon electrodes. Considering this, the general objective of this chapter is to design a porous carbon electrode based on a 3-D architecture.

3.1.1. Existing methods vs Electrospinning technique to form 3-D carbon electrodes

There have been several reports on the fabrication of porous carbon-based electrodes. For example, (Jiang, Sheng, Long and Fan, 2015) and (Xu *et al.*, 2014) used etching and vacuum assisted filtration and hydrothermal, respectively to prepare 3-D porous carbon electrodes. However, both of these routes suffer from the issue of low scalability. In this regard, electrospinning is an encouraging method to make 3-D porous carbon electrodes, as it allows higher scalability over the 3-D carbon producing routes proposed by (Jiang, Sheng, Long and Fan, 2015) and (Xu *et al.*, 2014). (Zhang *et al.*, 2016) in their review highlights several reports, describing the use of the electrospinning technique to make the carbon electrodes. However, rather than a 3-D architecture of the carbon electrode, the reports highlighted by (Zhang *et al.*, 2016) show only porous on the carbon matrix. One way to make the 3-D architecture of the carbon electrodes is to make use of the axially controlled mode of electrospinning technique.

3.1.2. Axially controlled mode of electrospinning technique to form 3-D carbon electrodes

Controlling the axis, either the x or y-axis, during electrospinning is called as an axially controlled mode of the electrospinning. Previously, (Flox *et al.*, 2013) showed that by controlling X-axis direction throughout the electrospinning process offers an oriented network of the layer-by-layer fiber assembly, which resembles the architecture of a 3-D macro-porous electrode. According to (Flox *et al.*, 2013), this electrode design affords efficient transport of electrons and as well as effective accessibility of electrolyte ions. By applying the 3-D macro-porous carbons as electrodes, (Flox *et al.*, 2013) showed that the electrochemical performances of Vanadium Redox Flow batteries (VRFB) are enhanced. Therefore, one of the objectives of this chapter is *to design a 3-D architecture of the carbon electrode using the axially controlled mode of electrospinning technique.*

3.1.3. Existing methods vs Catalytic graphitization route to form porous carbon electrode

(Zhang *et al.*, 2016) in their review, highlighted that the widely reported method to make porous carbon nanofibers through electrospinning is to make use of polymers as a sacrificial host. However, according to (Zhang *et al.*, 2016), using polymers as a sacrificial host to form pores in electrospun fibers, require temperatures of thermal treatment $>1000^{\circ}$ C. An example of this case is Poly(methyl methacrylate) (PMMA). According to (Zhang *et al.*, 2016), the use of such high temperatures can cause deterioration of 3-D electrode architecture and reduces the electrochemical performance. Though, (Griffin, Forse and Grey, 2016) proposed that co-polymer like Nafion is a favorable nominee for a sacrificial host, as it decomposes within $< 1000^{\circ}$ C. But, the high price of Nafion, which is ~ 7 times higher than

PMMA (Sigma-Aldrich®), could increase the cost of electrospinning process. These aspects escalation the cost of production and create an obstacle in using electrospinning technique in the practical applications. Towards this, according to (Zhang *et al.*, 2016), the use of catalytic graphitization route to form pores can have an advantage over polymer removal methods, as catalytic graphitization route uses metal salt as a precursor. Since the price of the traditional metal salt precursor (Iron (III) acetylacetonate) is ~3 times lower than Nafion (Sigma-Aldrich®) and also needs lower temperatures during the thermal treatment to form pores (~< 800° C).

According to (Zhang *et al.*, 2016), in order to achieve the catalytic graphitization process a polymer blend solution of metal salt and carbon polymer precursor needs to be electrospun to form mats. It is essential to stabilize these mats in the air and carbonize in an inert atmosphere. According to (Boris, 2000), during the air treatment metal salt decomposes to form metal oxide structures. Whereas, according to (Shen, 2015), under the inert atmosphere (around 800° C), in order to maintain the low partial pressure of oxygen as well as due to thermodynamic favorability carbon matrix reacts with the liberated oxygen anions of metal oxide to form carbon monoxide. This carbon monoxide further reduces the metal oxide to metal and carbon to form carbon dioxide. This overall process, carving and etching carbon, gives rise to the formation of pores in the carbon matrix. (Zhang *et al.*, 2016) in their review highlights several reports which describes the use of the catalytic graphitization method. However, the reports highlighted by (Zhang *et al.*, 2016) does not include the use of the catalytic graphitization route in the 3-D architecture of the carbon electrode. Therefore, one of the objectives of this chapter *is to implement*

the catalytic graphitization route in axially controlled electrospun 3-D carbon electrodes. Besides this, since the architecture of being porous in a 3-D architecture of the carbon electrode could enhance the value of the capacitance at high charging and discharging rates. So, one of the objectives of this chapter is also to evaluate the electrochemical properties of the prepared electrodes. Additionally, as the pores formed with the catalytic graphitization route would largely depend upon the amount of the metal salt precursor used and in-turn in their electrochemical properties. Consequently, one of the objectives of this chapter is also to investigate the influence of the concentration of the metal salt precursor towards the material and the electrochemical properties.

3.1.3. Objectives of this chapter

Based on the discussion mentioned in the above section, the objectives of this chapter are:

- (i) To design a 3-D architecture of the carbon electrode using the axially controlled mode of electrospinning technique.
- (ii) To implement the catalytic graphitization route in axially controlled electrospun 3-D carbon electrodes.
- (iii) To evaluate the influence of the metal salt precursors' concentration towards the material and electrochemical properties of the electrodes prepared with the objective (i) and (ii).

3.2. Fabrication of electrodes

3.2.1. Preparation of polymer blend solutions

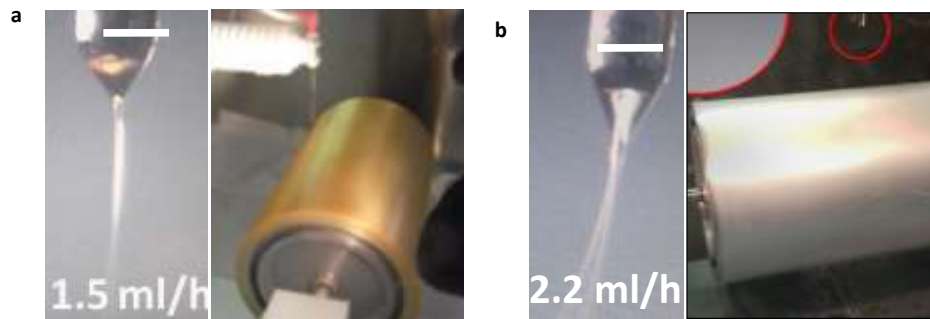


Figure 3. 1. (left) Visualization of the Taylor cone and (right) collection of the polymer mats on the rotating drum collector using the axially controlled mode of electrospinning. The scale in the Taylor cone is 1.0 mm.

A blend precursor solution was formed by dissolving Iron (III) Acetylacetonate (99%, $\text{Fe}(\text{acac})_3$) and Polyacrylonitrile (99%, PAN; M_w : 150,000) in N, N-dimethylformamide (99%, DMF) for a 1 h at 80°C. Acetylacetonate anion based precursor is selected over chloride anion (a generally used salt precursor in the field) as acetylacetonate anion based precursor shows a homogenous distribution of nanostructures on the carbon matrix after the thermal treatments (*See Appendix section A.1 for further details*). The quantity of PAN polymer (as carbon precursor) and DMF (as solvent) was about 2 g and 20 g, respectively. Three different concentrations were chosen to study the influence of the iron precursor and understand their material and electrochemical properties. Three different weight percent (wt. %) namely, 1 wt. %, 3 wt. % and 4.7. wt. % was used. The wt. %, such as in the case of $\text{Fe}(\text{acac})_3$, would signify the weight content of Fe in $\text{Fe}(\text{acac})_3$ with respect to PAN polymer. For comparative

purpose, a reference sample of a polymer blend solution without the iron salt precursor was also prepared. These polymer blends were loaded into 20 ml plastic syringes.

3.2.2. Preparation of polymer mats using axially controlled mode of electrospinning

The plastic syringe with the polymer blend was attached to a stainless steel spinneret with an internal and external diameter of 0.6 mm and 0.9 mm, respectively. In regards to axially controlled mode of the electrospinning, the speed and acceleration of the spinneret were controlled in the direction of X -axis. The speed and acceleration for X -axis movement of the spinneret were 2.45 mm s^{-1} and 1.47 mm s^{-2} , respectively. The polymer blends with Fe salt precursor were injected with a feed rate of 1.5 ml h^{-1} , whereas 2.2 ml h^{-1} for the polymer blends without the Fe salt precursor. An electrical force, in terms of the voltage, was applied between the spinneret and the ground. With the application of the voltage between the spinneret (as a source) and ground, the ejected droplet of the polymer blends forms a Taylor cone (a conical shape jet). According to (Zhang *et al.*, 2016), it is important to achieve this Taylor cone to have one 1-D fiber, as it indicates a balance between the electrostatic force and surface tension. **Figure 3.1 a-b (left image)**, shows an example of the Taylor cone for the polymer blends prepared with and without Fe precursor. The values of the voltages to form the Taylor cone are shown in **table 3.1**. These fibers are collected on a rotating drum. **Figure 3.1 a (right)** shows the collection of the fibers with the without Fe precursor. Whereas, **Figure 3.1 b (right)** for the fibers with Fe precursor. Prolong time of electrospinning leads to fiber mats of 60 cm x 30 cm. An example is shown in **Figure 3.2 a** with the polymer mats prepared with Fe precursor. As, the electrospinning equipment used in this

investigation is an industrial-prototype system from Nanotechnology Solutions, Yflow® (*see chapter 2 for details*), therefore the use and in-turn prepared 3-D carbon electrodes can be potentially applied in the commercial products.

Iron precursor content	Source voltage (kV)	Collector voltage (kV)	Feed rate (ml h ⁻¹)	Drum rotation (rpm)
0 wt.%	6.93	-6.97	2.2	947
1 wt.%	10.56	-8.46	1.5	969
3 wt.%	12.07	-7.09	1.5	929
4.7 wt.%	6.93	-3.01	1.5	500

Table 3. 1. Parameters for axially controlled electrospinning 3-D electrodes. In all cases, the distance between the source (spinneret outlet) to the ground (drum collector) was about 8 cm.

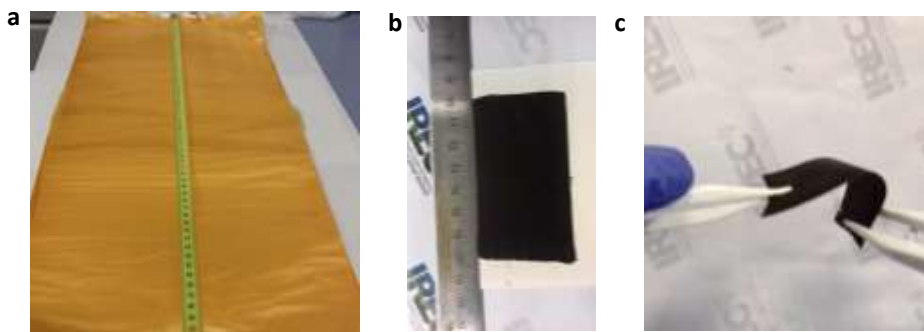


Figure 3. 2. (a) Polymer mats with iron precursor nearly an area of 60 cm x 30 cm, (b) metal oxide based CNFs film after the thermal treatments and (c) showcase of flexible metal oxide based CNFs film.

3.2.3. Thermal treatment of the polymer mats

The obtained polymer mats were stabilized in the air at 270°C (7 h; 1°C min⁻¹) and, finally, where carbonized in Ar/H₂ (5%) at 500°C and 800°C (1 h at each step; 5°C min⁻¹) to obtain metal oxide-carbon nanofibers (CNFs) film. An example is shown in **Figure 3.2 b**. It is noteworthy that the Ar/H₂ (5%) was used over Ar (inert) as the atmosphere during the carbonization process, Ar/H₂ (5%) acts reducing atmosphere to provide higher specific surface area related to the carbon pores, which is a favorable factor of the electrochemical supercapacitors (*See Appendix section A.2 for further details*). The obtained films are self-supporting and flexible. An example is shown in **figure 3.2 c**. These films were stored in Ar-glove box and used as electrode materials without any further treatment.

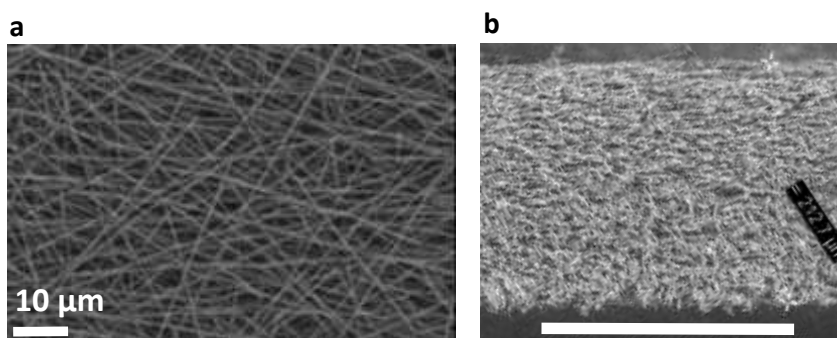


Figure 3. 1. (a) SEM images of 4.7 wt. % catalyst added CNFs, showing random and interconnected orientation. (b) Cross-section of the 3-D electrodes whose thickness was > 200 μm (scale: 200 μm).

3.3. Material characterization

The obtained films of CNFs were characterized by several techniques, which are described in the following sections. The SEM image of the CNFs

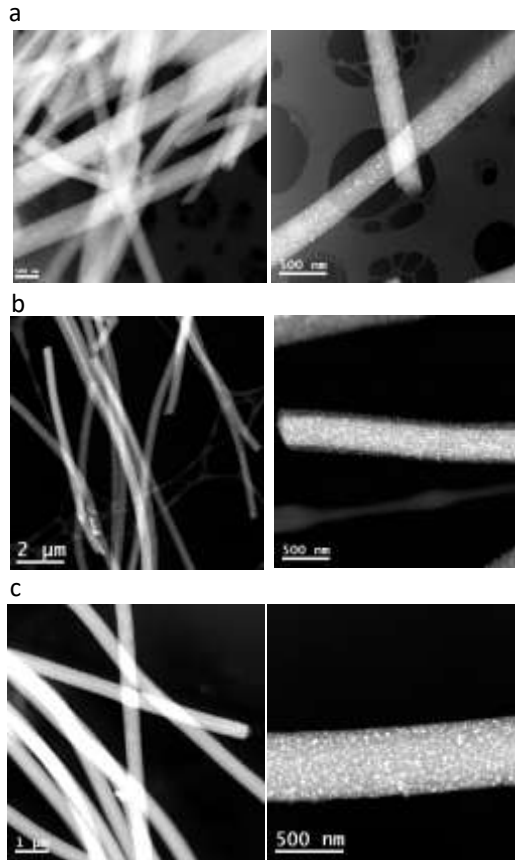


Figure 3. 2. Annular dark-field-scanning transmission electron microscopy images of (a) 1 wt. % iron precursor CNFs. (b) 3 wt. % iron precursor CNFs. (c) 4.7 wt. % iron precursor CNFs, showing homogenous distribution of nanostructures in carbon fiber.

films, as in **Figure 3.3**, show-oriented network of layer-by-layer fibers, resembling a 3-D macro-porous electrode. For the explored range of the Fe precursor, the nominal concentration was from 4.7 wt. % to 3 wt. %, 1 wt. %. ADF-STEM images, as shown by **figure 3. 4**, indicates a homogeneous distribution of the nanostructures in all concentrations of Fe precursor.

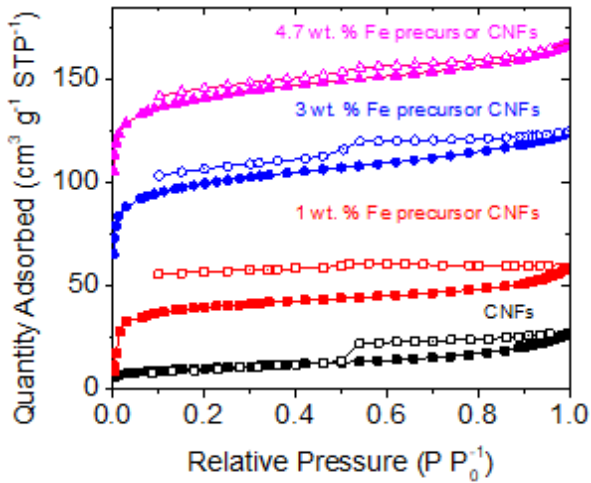


Figure 3. 3. Nitrogen sorption isotherms of carbon nanofibers with variation of the Fe precursor concentration

TGA analysis was carried out and the weight loss is shown in **Appendix-A, section A.3**. The residual weight loss indicates the amount of

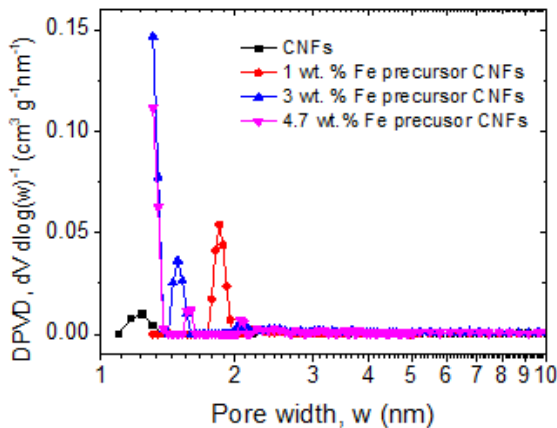


Figure 3. 4. DFT differential pore volume distribution (DPVD) of carbon nanofibers with variation of the catalyst precursor concentration. Textural analysis show isotherm related to the microporous region and the majority of the pores within the width of < 2 nm.

nanostructures in the CNFs. TGA shows that by decreasing the catalyst

precursor from 4.7 wt. % to 3 wt. % and 1 wt. %, the content of nanostructures decreases from 21.2 wt. % to 12.8 wt. % and 5.6 wt. %, respectively. To understand the pore properties, textural analysis via nitrogen sorption isotherm was carried out. The obtained isotherms are shown in **Figure 3.5**. The figure displays hysteresis of H4 type with an I(b) type isotherm.

According to (Thommes *et al.*, 2015), this type of hysteresis indicates the broad range micro-porosity in the range $< \sim 2.5$ nm and cylindrical mesoporosity caused by cavitation-induced evaporation (*See chapter 2, for theory*) Specific Surface Area (SSA) analysis were carried by BET theory and the corresponding data is shown in **Table 3.2**.

Iron precursor	BET-SSA (m ² g ⁻¹)	DFT micropore volume (cm ³ g ⁻¹)	DFT mesopore volume (cm ³ g ⁻¹)	DFT Cumulative pore volume (cm ³ g ⁻¹)	Micropore (%)	Mesopore (%)	Micropore volume /Mesopore volume (v/v)
0 wt. %	36	0.01182	0.02731	0.03913	30.2	69.79	0.43
1 wt. %	155	0.05	0.02899	0.07899	63.2	36.7	1.72
3 wt. %	317	0.12902	0.04996	0.17898	72.0	27.9	2.58
4.7 wt. %	440	0.19458	0.04473	0.23931	81.3	18.6	4.35

Table 3. 1. Data depicting the BET-SSA and DFT pore volumes and as well as the four-probe electrical conductivity values with the variation of Fe precursor in the polymer blend.

For the comparative purpose, CNFs without Fe precursor was also evaluated, which considered as 0 wt. % of Fe precursor. The analysis indicates that by decreasing the concentration of the Fe precursor, corresponding BET-SSA decreases from 440 to 317 m² g⁻¹, 155 m² g⁻¹ and 36 m² g⁻¹. Differential pore size and volume analysis were also carried out to

understand the pore distribution and the plot is shown in **Figure 3.6**. This plot indicates a large distribution of micropores in the range of 1-2 nm. The micropore volume to cumulative pore volume decreases from 81% to 72%, 63% and 30% with the decrease in Iron precursor. Although, this decrease in pore volume and BET specific surface area is an unfavorable parameter towards capacitance, the electrical conductivity of the film electrode is important. The electrical conductivity of the film electrodes was measured

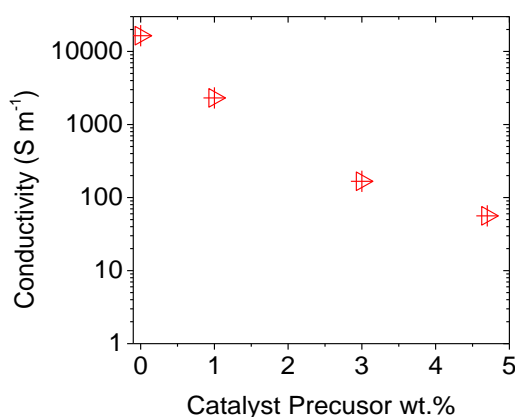


Figure 3. 5. 4-probe conductivity of electrode measured with respect to the weight of the catalyst.

by 4-probe experiments (*see chapter 2, for theory*). The results are shown in **Figure 3.7**. The data indicates that the electrical conductivity of the film electrode increases from a value of 56 to 16,450 S m⁻¹ with the decreased of the Iron precursor concentration. This increase in conductivity can have a high influence on the capacitance enhancement at high rates, which is a favorable factor to retain capacitance at high rates. Since, the low electrical conductivity of 56 S m⁻¹ was observed with the higher concentration of Fe precursor (4.7 wt. %), concentrations of Fe precursor above 4.7 wt. % were not considered in this investigation. P-XRD analysis was carried out to observe the crystallographic information of the nanostructures present in

the matrix of CNFs. The P-XRD pattern of the samples is shown in **Figure 3.8**. The analysis indicates that the samples prepared with the lower Fe precursor concentration, such as 1 wt. % and 3 wt. % shows the presence of α -Fe₂O₃. This phase of Fe₂O₃ can be indexed to the JCPDS card number of 00-033-0664. Whereas, cubic γ -Fe₂O₃ phase with the CNFs prepared with

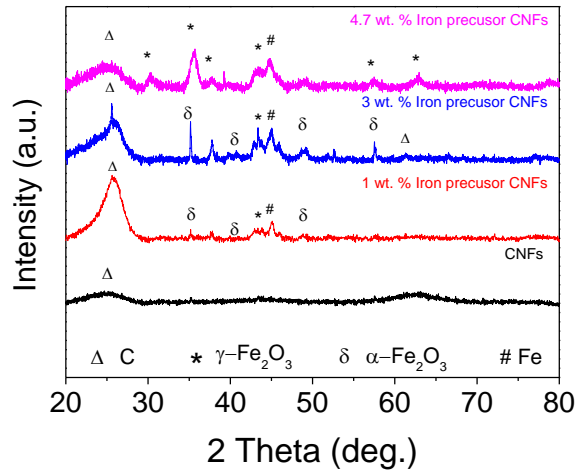


Figure 3. 6. X-ray powder diffraction (XRD) patterns of the fibers used in the present study

the higher concentration of the Fe precursor (4.7 wt. %), indexing to the JCPDS card number of 00-039-1346. It is noteworthy to mention that the metallic Fe can be also seen with the CNFs prepared with Fe precursors. This Fe can be indexed to a JCPDS card number of 00-006-0696. Whereas, with CNFs without Fe precursor, such as 0 wt. %, pattern related to the Iron or Iron oxide phases were absent.

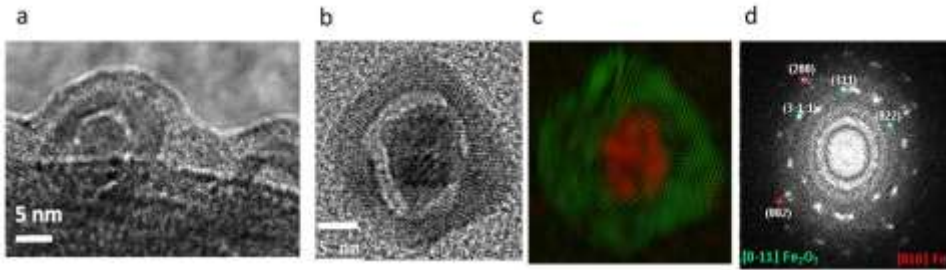


Figure 3. 7. (a) BF-TEM and (b) ADF- STEM of images of the nanostructure. (c) EELS mapping and (d) reduced FFT and phase filtered composition maps of the nanostructure.

Further imaging analysis was carried out with the samples to understand the pores and the decoration of Fe/Fe₂O₃ structures on the CNFs matrix. In this case, the CNFs prepared with 4.7 wt. % of Fe precursor was analyzed first. The BF-TEM *image* of the nanostructure attached to the fiber surface is shown in **Figure 3.9 a**. Furthermore, ADF-STEM images of one such nanostructure, as shown by the **figure. 3.9 b**, show a yolk-shell morphology. The EELS composition map obtained on these nanostructures is shown by **figure.3. 9 c**, which indicates that the yolk is composed of iron, while the shell is rich in with iron and oxygen. Reduced-FFT and phase filtered composition maps as well as its reciprocal space (frequency space) analyses, as shown by the **figure. 3.9 d**, show that the shell is composed of cubic Fe₂O₃, with [FD₃-MZ] - Space group 227, also named as γ -Fe₂O₃ crystal phase, with lattice parameters of $a = 0.837$ nm, and $\alpha = 90^\circ$ as visualized along the [0-11] direction, and the yolk of cubic Fe, [FM₃-M] - Space group 225, with lattice parameters of $a = 0.3595$ nm, and $\alpha = 90^\circ$ as visualized along [010] direction. Lowering the concentration of Fe precursor, such as 3 wt. % and 1 wt. % shows the absence of yolk-shell Fe/Fe₂O₃ morphology (*See Appendix section A.3*).

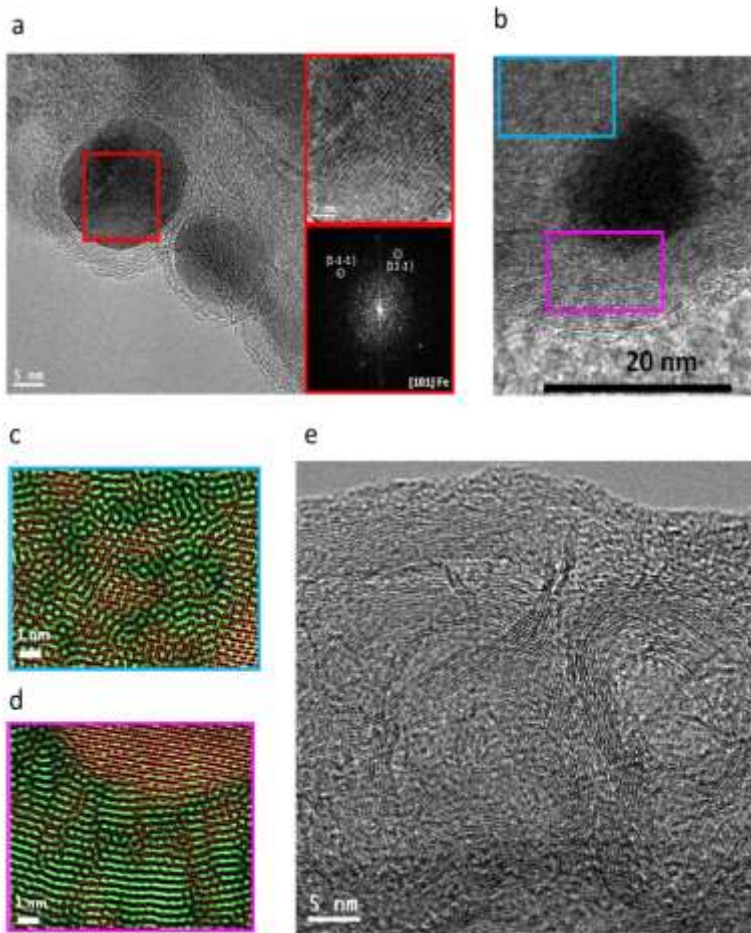


Figure 3. 8. a, Left: low magnification TEM image showing the nanoparticles surrounded by graphitic carbon. Right: the HRTEM detail of the red squared area and the corresponding reduced FFT spectrum indicate that the nanoparticle crystallizes in the Cubic Fe, $[FM_3M]$ -Space group 225, with lattice parameters of $a = b = c = 0.3595$ nm, and $\alpha = \beta = \gamma = 90^\circ$ as visualized along the $[101]$ direction. b, HRTEM image showing the carbon ordering (graphitic layers) around the nanostructure. Phase filtered image from the selected regions, (Green- Carbon and Red- Iron): c, showing non-ordered carbon and d, showing turbostratic Ts-effect component of ordered graphitic structures(Oya and Marsh, 1982a). e, Turbostratic Ts-effect component of ordered graphitic pores on matrix of CNFs

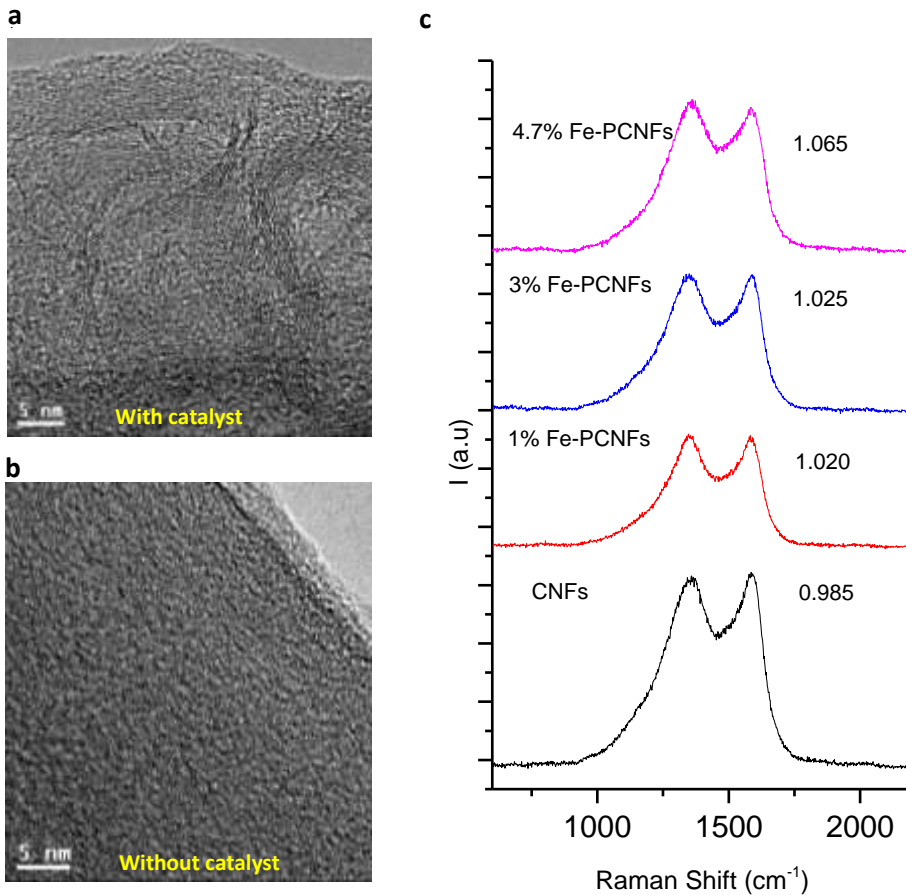


Figure 3. 9. HRTEM images of (a) Fe precursor added CNFs and (b) without Fe precursor. (c) Raman spectra of catalyst added and without carbon nanofibers. Purple and orange highlight, indicates the D and G band respectively.

Further imaging analyses via HR-TEM on the carbon matrix prepared with a 1 wt. % of iron precursor (**Figure. 3.10 a**), indicate the presence of graphitic carbon pores, bordering the nanostructures. The power spectrum (FFT) shows that these nanostructures are composed of the cubic Fe crystal phase (red square in **Figure. 3.10 a**). Phase filtering analysis in one such location (Pink color square in **Figure. 3.10 b**), demonstrates that the Fe is surrounded by ordered carbon layers (**Figure. 3.10 d**). However, non-

ordered carbon layers have also been observed in the carbon matrix (**Figure 3.10 c**). This non-ordered carbon, as highlighted with the blue color box in the **figure 3.10 c**, resembles a non-ordered carbon, whereas, the carbon ordering resembles to turbostratic T_s -effect component of ordered graphitic structures, as previously highlighted by (Oya and Marsh, 1982a). Besides Fe nanostructures, these turbostratic T_s ordered graphitic layers form a pore-like structure (**figure 3.10 e**), which was also observed at different locations of the carbon matrix (**Appendix-A, section A.4**). **Figure 3.11 a and b**, shows the HR-TEM images of carbon matrix with and without Fe precursor. These graphitic layers appear when the CNFs are produced when Fe precursor are used (**Figure 3.10 a**). However, the graphitic carbon ordering is absent when no Fe precursor is used to make CNFs. Both samples were also analyzed by Raman spectroscopy and their spectra are shown by **Figure 3.11 c**. The degree of graphitization, which is the ratio between I_G/I_D (**see chapter 2, for the theory**), indicates a value of 0.985 without the Fe precursor, whereas 1.020 when Fe precursor is added. The following paragraph explains the formation of the graphitic ordered carbon pores based on the existing theories.

Mechanism of pore formation based on existing theories: *In the above analysis formation of the yolk-shell Fe/Fe₂O₃ nanostructures were observed. This yolk-shell structures might happen via the reductive transformation of the Kirkendall effect, during carbothermal treatment (Tracy, 2014; Cho, Hong and Kang, 2015). Such kind of Kirkendall effect has a faster diffusion of iron cations towards an inner-wards direction when compared to the outward diffusion of the oxygen anions. This happens due to the larger ionic radius of iron cations than oxygen anion, converting the iron oxide into iron. The ionic radius of Fe cations, Fe²⁺ is 76 pm, Fe³⁺ is 65 pm, whereas oxygen*

anions are 140 pm (Cho, Hong and Kang, 2015). Such a transformation is depicted via the Cabrera-Mott model (Tracy, 2014; Cho, Hong and Kang, 2015)(**Figure 3.12**). This discussion supports the formation of a yolk-shell morphology. In parallel, carbon neighboring to iron oxide reacts with the liberated oxygen anions to form the pores (as discussed in the introduction). This overall process gives rise to the pores adjoining to nanostructures (Ryu *et al.*, 2013; Tracy, 2014; Cho, Hong and Kang, 2015; Avireddy, Morante and Flox, 2016). At high temperatures, such as 800°C, the iron nanostructures form an eutectic-liquid of Fe_xC_y , which dissolves the amorphous carbon and, then, this dissolved amorphous carbon precipitates to form ordered graphitic structures(Oya and Marsh, 1982b; Krivoruchko and Zaikovskii, 1998; Caspers *et al.*, 2002). The formation of the T_s -effect ordered graphitic structures occurs because of the thermal treatment of non-graphitic parent carbon or non-graphitized turbostratic carbon domains with finely divided the small iron nanostructure (<20nm)(Oya and Marsh, 1982b).

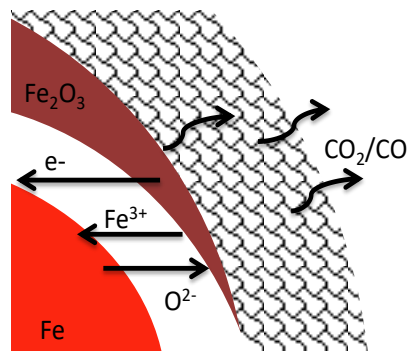


Figure 3. 10. Schematic showing reductive transformation of Kirkendall effect

3.4. Electrochemical Characterization

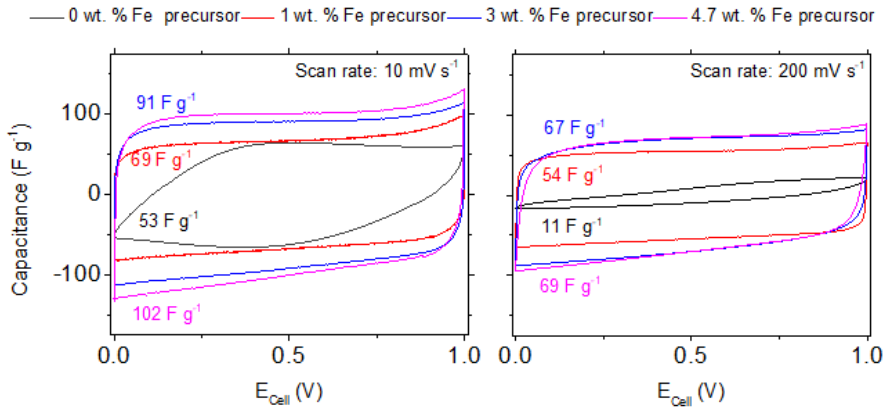


Figure 3. 11. CVs curves of the CNFs electrode in a two electrode cell configuration. Left graph indicates the charge storage behavior at a scan rate of 5 mV s^{-1} , whereas, right, shows at 200 mV s^{-1} .

Electrochemical performances are measured in a configuration of a two-electrode cell (see methods for details), where the electrolyte media is an aqueous solution of 6 M potassium hydroxide. Cyclic voltammogram of CNFs prepared with 1 wt. % of the iron precursor at a scan rate of 10 mV s^{-1}

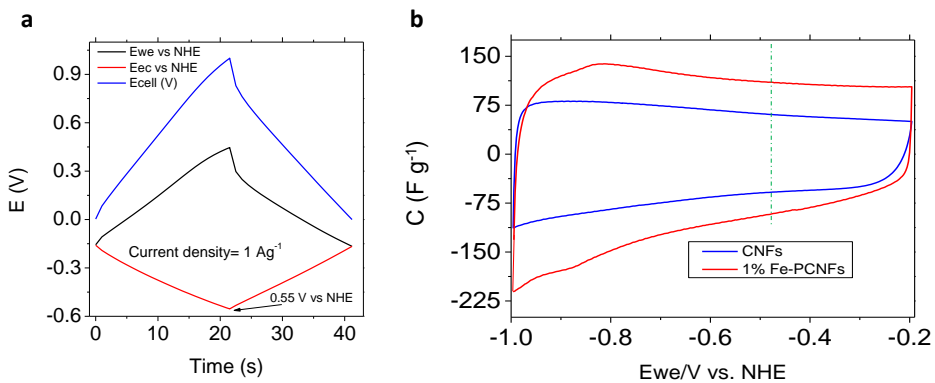


Figure 3. 12. (a) GCD curves of the individual behavior of electrodes, in a two electrode configuration. (b) CVs curves of carbon nanofibers with and without Fe precursor.

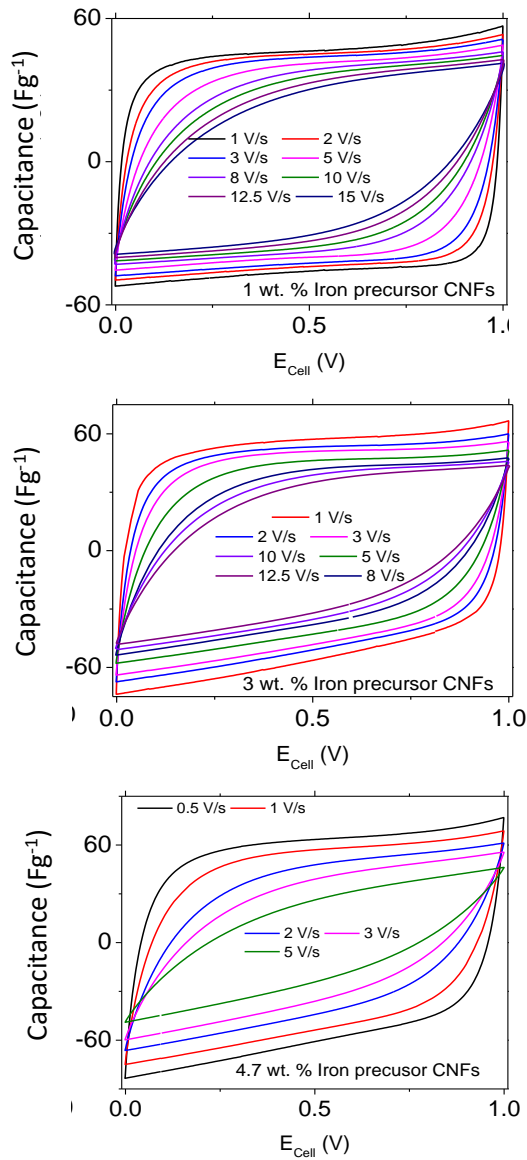


Figure 3. 13. CVs curves at different rates for (a) 1 wt. % (b) 3 wt. % and (c) 4.7 wt. % Fe precursor added carbon nanofiber electrodes

¹ is shown by the **figure. 3. 13**, which depicts a rectangular loop, corresponding to a capacitance of 69 F g⁻¹. A three electrode configuration

of EL-cell with a gold pseudo-reference is used to measure the individual potential windows of the electrodes (See methods for details). Galvanostatic mode of charge and discharge in a full cell within the 1.0 V, allows the negative electrode to function between 0.45 to -0.15 V vs. NHE (**figure 3.14 a**). Whereas, the positive electrode operates within -0.15 to -0.55 V vs. NHE. Since the contribution of redox reactions from Fe_2O_3 nanoparticles occurs beyond -0.55 V vs. NHE (**figure 3.14 b**), the rectangular response of CV curve in full cell configuration can be solely related to an electric double layer capacitances. This value of capacitance increases from 69 F g^{-1} to 91 and 102 F g^{-1} with the increase of iron precursor from 1 wt. % to 3 wt. % and 4.7 wt. %, respectively. As capacitance is associated from the sorption of charges at the FSI's between electrolyte and electrode and is proportionate to specific surface area and pore volume related narrow size micropores (Chmiola, 2006). The tendency of increase in capacitance is attributed with the increase of BET-SSA from 155 to 317 m^2

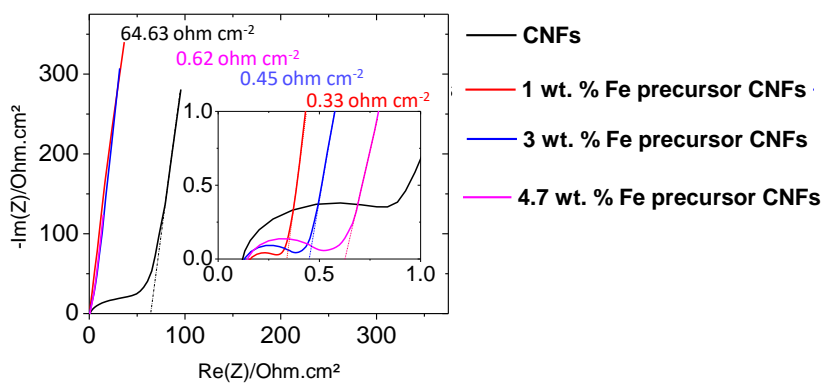


Figure 3. 14. Nyquist plot of the CNFs with different concentrations of the catalyst precursor. Inset, showing the high frequency region, indicating the contact resistance and as well as the equivalent distributed resistances.

g^{-1} and $440 \text{ m}^2 \text{ g}^{-1}$ and micropore volume from 63% to 72% and 81% (**Table 3.2**, as seen in previous sections).

While capacitance increases with the increase of iron precursor, the capacitance in a relationship with rate depicts an opposite trend. At high rates, such as at 200 mV s^{-1} , though the capacitance still resembles to a

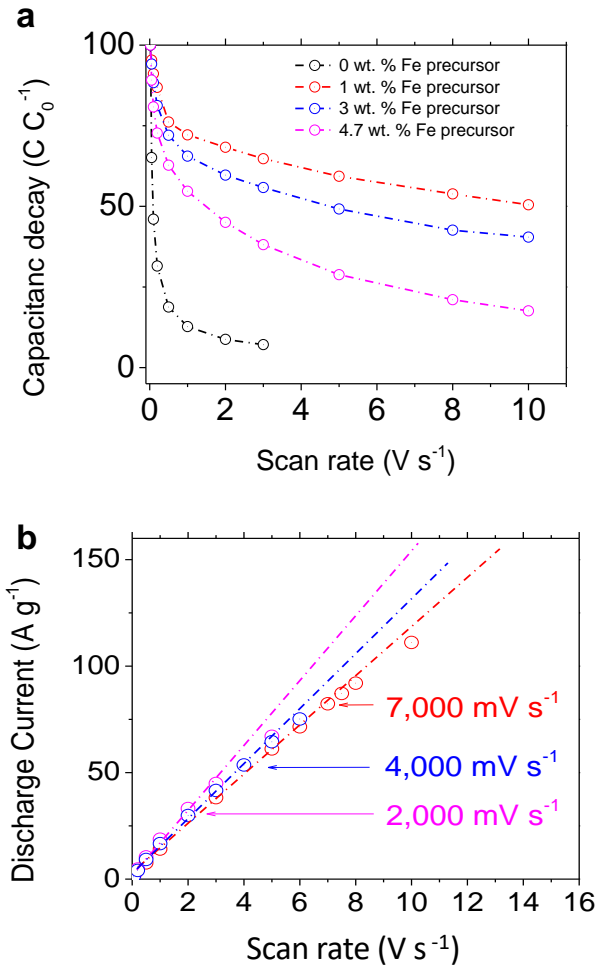


Figure 3. 15. (a) Correlation of the rate decay along with the concentration of catalyst precursor. (b) Plot between discharge current and scanning rate depicting the linear behaviour.

double layer charging, the capacitance values of 1 wt. %, 3 wt. % and 4.7 wt. % corresponds to 54 F g⁻¹, 67 F g⁻¹ and 69 F g⁻¹, respectively. This, as a capacitance rate decay represents a value of 79%, 74% and 67% ($C_{200\text{ mV s}^{-1}}/C_{10\text{ mV s}^{-1}}$). It is noteworthy that in the case of CNFs with 1 wt. % of the iron precursor, increasing scanning rate higher than 1,000 mV s⁻¹, still resembles the CV loop to a double layer capacitance (**Figure 3.15. b**). Whereas, carbon nanofibers prepared with the higher concentrations of iron precursor (3 and 4.7 wt. %) shows a change in capacitance response from rectangular to quasi-rectangular (**Figure 3.15. c and d**, respectively). As a whole, when the scan rates are varied from low (10 mV s⁻¹) to very high rates (5,000 mV s⁻¹), the order of capacitance value changes from 4.7 wt. % > 3 wt. % > 1 wt. % to 3 wt. % > 1 wt. % > 4.7 wt. %. These findings indicate an affinity in a decrease of rate-capacitance with the increase of iron precursor's concentration. Though the reduction in this rate-capacitance behavior is large, the electrolyte ion-exchange resistance of in-pore with bulk electrolyte ions (indicated by Equivalent Distributed Resistance, EDR) shows a minimal increase from 0.33 to 0.45 ohm cm⁻² and 0.62 ohm cm⁻² (**Figure 3.16**). Besides this, it is remarkable to observe their effects on the electrical conductivity with an increase of iron precursor from 1 wt. %, 3 wt. % and 4.7 wt. %, as it decreases largely from 2,313 to 167 S m⁻¹ and 56 S m⁻¹, respectively (**Figure. 3.7**). This trend corresponds to a decrease in the intrinsic conductivity of electrodes with the increase of iron precursor. This variation in conductivity has a strong influence on the movement of charge within the CNFs matrix, independently of the increased BET-SSA from 155 to 440 m² g⁻¹ and micropore volume from ~81% to ~63% (**Table 3.2**) and corresponding capacitance (69 to 102 F g⁻¹). This happens due to an increase of iron precursor, increases the nanostructures and associated pores in CNFs matrix, which shrinks the conductive cross section of the fiber.

Which is responsible for the decrease in the effective or overall conductivity of the electrode. This decrease of electrode's electrical conductivity causes hindrance to the electron transport through fiber as well as to electrical charging carbon surface, which can be supported with the reduction of charge polarization from ~ 24 to $13 \mu\text{F cm}^{-2}$ and $6 \mu\text{F cm}^{-2}$ with the increase of catalyst precursor (charge polarization is considered by normalizing capacitance value at $5,000 \text{ mV s}^{-1}$ with the BET-SSA). This reduction of electrical charging causes the CV curve to be quasi-capacitive and its values to decrease in the fibers prepared with the higher concentrations of catalyst. At high rates, such as $> 1000 \text{ mV s}^{-1}$, this hindrance towards electron transport and electrical charging of carbon surface causes the response of capacitance to become quasi-EDLC and its values to decrease. Because of these reasons, increasing iron precursor from 1 wt. % to 3 wt. % and 4.7 wt. %, decreases the maximum scan rate from 7,000 to 4,000 mV s^{-1} and 2,000 mV s^{-1} (**Figure. 3.17 b**) and increases

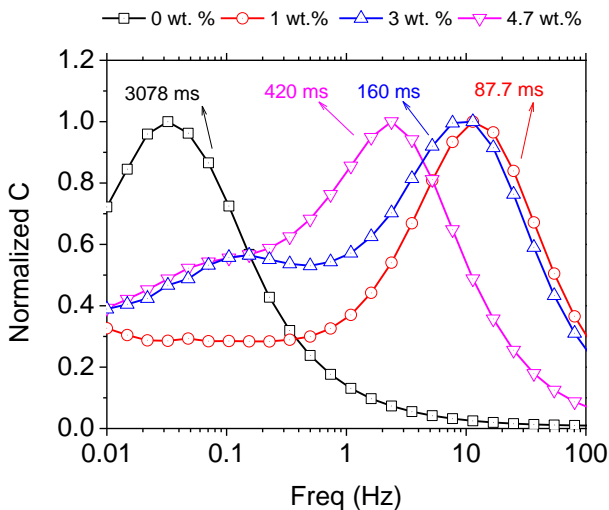


Figure 3. 16. Relationship between the relaxation time and the concentration of the catalyst

the relaxation time constant from 87.8 to 106 ms and 420 ms (minimum time to discharge the full energy from an double layer capacitor cell with an efficiency > 50%) (**Figure. 3.18**).

Furthermore, due to the absence of nanostructures and associated micropores, CNFs without any iron precursor shows higher conductivity of $16,450 \text{ S m}^{-1}$ than iron precursor added CNFs (56 to $2,313 \text{ S m}^{-1}$, **Figure 3.7**). And therefore, should show an EDLC behavior at high rates.

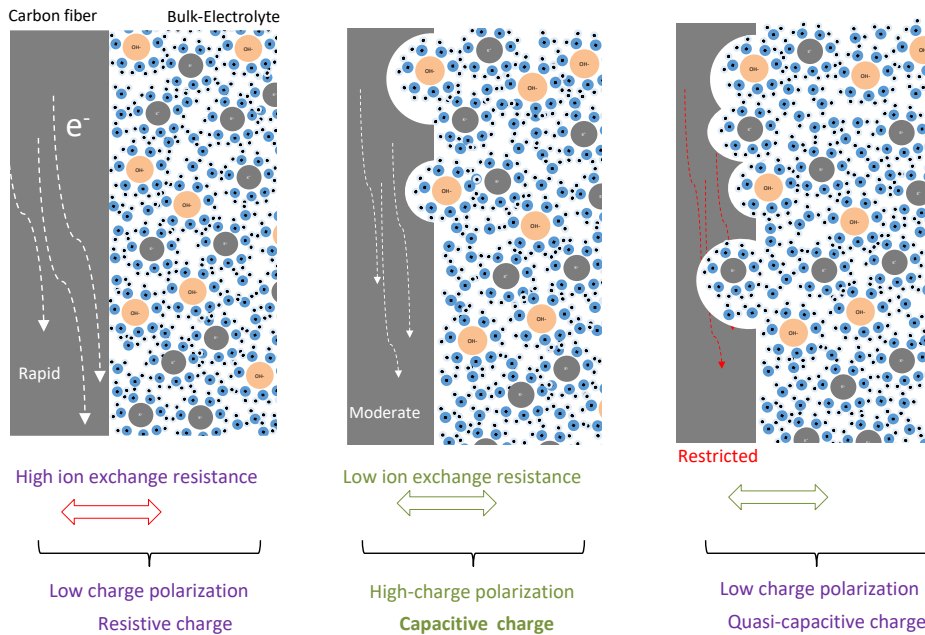


Figure 3. 17. Schematic illustration showing the influence of the Fe precursor concentration in the charging behavior of the carbon nanofibers at high rates, which specifies a tradeoff between the Fe precursor concentration and capacitance in the view of high rate capacitance.

Hypothesis: The low ELDC behavior in the CNFs without the Fe precursor could be related to the low specific surface area. As CNFs show a macro-pores 3-D architecture and extremely low BET- SSA of $36 \text{ m}^2 \text{ g}^{-1}$ (**Table 3.2**)

than iron precursor added CNFs ($155 - 440 \text{ m}^2 \text{ g}^{-1}$), CNFs behaves much like a planar electrode (Merlet *et al.*, 2012). In which, the FSI suffers from over-screening effect (Merlet *et al.*, 2012; Forse *et al.*, 2016). In over-screening effect, an excess charge of first ion layer is counterbalanced by second and following ion layer, restricting the movement of ions during charging and discharging. Because of this effect, the ion-exchange resistance increases to $64.63 \text{ ohm-cm}^{-2}$ (Figure 3.16) and a resistive capacitance response and low values are observed at high rates (11 F g^{-1} at 200 mV s^{-1} , Figure. 3.13).

So, an ideal concentration of the iron precursor to further achieve a high-rate capacitance would be between 0 - 1 wt. %. This understanding is shown in Figure 3.19. However, a further decrease in concentration will show a capacitance lower than that of a typical capacitance range of wider-microporous carbons (pore within 1-2 nm), such as Carbon Derived Carbons (CDCs) and graphene-like CDCs from the chlorination of titanium carbide or silicon carbide (~ 80 to 100 F g^{-1}) (Chmiola, 2006; Largeot *et al.*, 2008; Gao *et al.*, 2015). Moreover, an increase in concentration greater than 4.7 wt. %, though, would improve the capacitance, by increasing the specific surface area and related pores. But, will also diminish the rate capacitance as well as increase the relaxation time, as electrode resistance escalations due to shrinkage of fiber's conductivity. Therefore, a balance between conductivity and capacitance allows the electron to move throughout the electrode and highly charging the carbon surface of FSI even at high rates. This optimum point of balance was currently found to be with the fibers prepared with 1 wt. % of the iron precursor.

Comparison with the literature:

The relaxation time constant of 87.8 ms for the CNFs prepared with 1% of iron precursor, was lower than that of on-chip micro-supercapacitor based

on activated carbon (700 ms (Pech *et al.*, 2010)) and close to carbon onions micro-supercapacitors (26 ms (Pech *et al.*, 2010)). Moreover, with supercapacitors prepared in an aqueous 6 M potassium hydroxide electrolyte (Fig. 4), this relaxation time was lower-most among the other 3-D carbon frameworks such as reduced graphene oxide (1239 ms (Jiang, Sheng, Long and Fan, 2015)), carbon derived metal organic frameworks, MOF (825 ms (Wang *et al.*, 2016)), 3-D graphene (490 ms (Xu *et al.*, 2014)), functional pillared graphene (475 ms (Jiang, Sheng, Long, Wei, *et al.*, 2015)), graphene nanomesh carbon nanotube (236 ms (Jiang, Sheng, Long and Fan, 2015)), holey 3-D graphene (170 ms (Xu *et al.*, 2014)), carbon derived 3-D graphene-MOF (215 ms (Wang *et al.*, 2016)).

3.5. Conclusions

This chapter tackles the rate capability (capacitance fade over rate) problem in binder-based porous carbon supercapacitors. This problem is resolved by fabricated a 3-D architecture of porous carbon electrode through the axially controlled mode of the electrospinning process. The carbon pores are induced with the help of metal/metal oxide pore method. This process is also called as a catalytic graphitization method. In such a method, the iron precursor is blended with the polymer solution, which is later electrospun to form mats. These modified mats were subjected to thermal treatments to obtain free-standing electrode films. Analysis through imaging techniques on these films indicates a formation of finely dispersed nanostructures of iron/iron oxide and as well as the porous on the carbon surface. Besides imaging analysis, textural analysis via gas adsorption measurements also confirms the presence of pores. Furthermore, analysis through high-resolution imaging and Raman spectroscopy indicates the presence of a graphitic type of carbon ordering with the carbon pores. To explain these observations, a hypothesis based

on existing theories is presented. The hypothesis depicts that the nanostructures etches or carves the surface of nanofibers to form pores through well-known Kirkendall process. Whereas, at high temperatures (such as 800°C) the nanostructures induce their catalytic activity to form graphitic carbon pores. Conclusively, an electrospun iron/iron oxide porous carbon nanofiber based 3-D electrode was achieved. In this way, the first and the second objective of this chapter were accomplished. Furthermore, in order to achieve an optimum rate capability, the influence of different concentrations of the iron precursor was also investigated. In this regard, three different concentrations of iron precursor were used, namely, 1 wt.%, 3 wt.% and 4.7 wt.%. The analysis of the results are the following: Firstly, increasing the concentration of iron precursor from 1 wt.% to 4.7 wt.% results in the increase of ratio between micropore to mesopore volume by a factor of 4.3. This increase in the ratio increases the values of capacitance by a factor of 1.5 (precisely from 69 to 102 F g⁻¹). This observation was supported with the increased craving of carbon surface with the increased density of nanostructures, as deduced with gravimetric and high-resolution imaging techniques. Secondly, the increased craving or etching of the carbon with the increase of iron precursor (1 to 4.7 wt.%) shrinks the electrical conductivity of the fiber electrode by a factor of 41 (from 2,313 to 56 S m⁻¹). This decrease in the electrodes' electrical conductivity hinders the electron transport through the fiber electrode. The combination of these features directly collaborates with the relaxation time constant for the supercapacitor cells prepared electrodes. For example, the least concentration of the iron precursor (1 wt.%) shows a relaxation time constant value of nearly 88 ms. This value increases to 160 ms and 420 ms with samples prepared with a higher concentration of iron precursor (3 wt.% and 4.7 wt.%, respectively). These results indicate a

tradeoff tendency between capacitance and conductivity, which is directly linked to the variation of the concentration for the iron precursor. Therefore, conclusively, apart from considering the design aspect of the 3-D electrode and the use of catalytic graphitization method, it is also vital to use an optimum concentration of the iron precursor to achieving high electrochemical performance. As a whole, the exposed method of using a 3-D architecture based porous carbon electrode along with the catalytic graphitization method with the optimum concentration of metal precursor, is an important strategy in designing high-rate macro-size supercapacitors with both better energy and power capabilities.

3.6. References

Avireddy, H., Morante, J. R. and Flox, C. (2016) 'A Perspective: Could Carbon Current Collectors Improve the Energy Density of Aqueous Alkaline Symmetric Supercapacitors?', *Energy Harvesting and Systems*, 3(4), pp. 1–10. doi: 10.1515/ehs-2016-0015.

Boris, V. L. (2000) 'Mechanism of carbothermal reduction of iron , cobalt , nickel and copper oxides', *Thermochimica Acta*, 360, pp. 109–120. Available at: <http://opensourceecology.org/w/images/c/c3/Lvov.pdf> (Accessed: 17 October 2017).

Caspers, P. J. *et al.* (2002) 'In vivo confocal raman spectroscopy of the skin', *Microscopy and Microanalysis*, 8(SUPPL. 2), pp. 288–289. doi: 10.1017/S1431927602020226.

Chmiola, J. (2006) 'Supporting Material: Anomalous Increase in Carbon Capacitance at Pore Sizes Less Than 1 Nanometer', *Science*, 313(5794), pp. 1760–1763. doi: 10.1126/science.1132195.

Cho, J. S., Hong, Y. J. and Kang, Y. C. (2015) 'Design and Synthesis of Bubble-Nanorod-Structured Fe₂O₃ -Carbon Nanofibers as Advanced Anode Material for Li-Ion Batteries', *ACS Nano*. American Chemical Society, 9(4), pp. 4026–4035. doi: 10.1021/acs.nano.5b00088.

Flox, C. *et al.* (2013) 'Highly electrocatalytic flexible nanofiber for improved vanadium-based redox flow battery cathode electrodes', *RSC Advances*. The Royal Society of Chemistry, 3(30), p. 12056. doi: 10.1039/c3ra40463c.

Forse, A. C. *et al.* (2016) 'New perspectives on the charging mechanisms of

supercapacitors', *Journal of the American Chemical Society*. American Chemical Society, 138(18), pp. 5731–5744. doi: 10.1021/jacs.6b02115.

Gao, P. C. *et al.* (2015) 'Graphene-like carbide derived carbon for high-power supercapacitors', *Nano Energy*, 12, pp. 197–206. doi: 10.1016/j.nanoen.2014.12.017.

Griffin, J. M., Forse, A. C. and Grey, C. P. (2016) 'Solid-state NMR studies of supercapacitors', *Solid State Nuclear Magnetic Resonance*, 74–75(March), pp. 16–35. doi: 10.1016/j.ssnmr.2016.03.003.

Jiang, L., Sheng, L., Long, C. and Fan, Z. (2015) 'Densely packed graphene nanomesh-carbon nanotube hybrid film for ultra-high volumetric performance supercapacitors', *Nano Energy*, 11, pp. 471–480. doi: 10.1016/j.nanoen.2014.11.007.

Jiang, L., Sheng, L., Long, C., Wei, T., *et al.* (2015) 'Functional Pillared Graphene Frameworks for Ultrahigh Volumetric Performance Supercapacitors', *Advanced Energy Materials*, 5(15), p. 1500771. doi: 10.1002/aenm.201500771.

Krivoruchko, O. P. and Zaikovskii, V. I. (1998) 'A new phenomenon involving the formation of liquid mobile metal-carbon particles in the low-temperature catalytic graphitisation of amorphous carbon by metallic Fe, Co and Ni', *Mendeleev Communications*, 8(3), pp. 97–99. doi: 10.1070/MC1998v008n03ABEH000944.

Largeot, C. *et al.* (2008) 'Relation between the ion size and pore size for an electric double-layer capacitor', *Journal of the American Chemical Society*, 130(9), pp. 2730–2731. doi: 10.1021/ja7106178.

Merlet, C. *et al.* (2012) 'On the molecular origin of supercapacitance in nanoporous carbon electrodes', *Nature Materials*. Nature Publishing Group, 11(4), pp. 306–310. doi: 10.1038/nmat3260.

Oya, A. and Marsh, H. (1982a) 'Phenomena of catalytic graphitization', *Journal of Materials Science*. Kluwer Academic Publishers, 17(2), pp. 309–322. doi: 10.1007/BF00591464.

Oya, A. and Marsh, H. (1982b) 'Phenomena of catalytic graphitization', *Journal of Materials Science*, 17(2), pp. 309–322. doi: 10.1007/BF00591464.

Pech, D. *et al.* (2010) 'Ultrahigh-power micrometre-sized supercapacitors based on onion-like carbon', *Nature Nanotechnology*, 5(9), pp. 651–654. doi: 10.1038/nnano.2010.162.

Ryu, W.-H. *et al.* (2013) 'Cobalt(ii) monoxide nanoparticles embedded in porous carbon nanofibers as a highly reversible conversion reaction anode for Li-ion batteries', *Journal of Materials Chemistry A*. The Royal Society of Chemistry, 1(10), p. 3239. doi: 10.1039/c3ta01443f.

Shen, Y. (2015) 'Carbothermal synthesis of metal-functionalized nanostructures for energy and environmental applications', *J. Mater. Chem. A*. The Royal Society of Chemistry, 3(25), pp. 13114–13188. doi: 10.1039/C5TA01228G.

Thommes, M. *et al.* (2015) *Physisorption of gases, with special reference to the evaluation of surface area and pore size distribution (IUPAC Technical Report)*, *Pure and Applied Chemistry*. doi: 10.1515/pac-2014-1117.

Tracy, B. D. A. and J. B. (2014) 'Nanoparticle conversion chemistry: Kirkendall effect, galvanic exchange, and anion exchange', *Nanoscale*. The Royal Society of Chemistry, 6(21), pp. 12195–12216. doi: 10.1039/C4NR02025A.

Wang, L. *et al.* (2016) "Brick-and-mortar" sandwiched porous carbon building constructed by metal-organic framework and graphene: Ultrafast charge/discharge rate up to 2Vs⁻¹ for supercapacitors', *Nano Energy*, 30, pp. 84–92. doi: 10.1016/j.nanoen.2016.09.042.

Xu, Y. *et al.* (2014) 'Holey graphene frameworks for highly efficient capacitive energy storage', *Nature Communications*, 5. doi: 10.1038/ncomms5554.

Zhang, B. *et al.* (2016) 'Recent advances in electrospun carbon nanofibers and their application in electrochemical energy storage', *Progress in Materials Science*. Elsevier Ltd, 76, pp. 319–380. doi: 10.1016/j.pmatsci.2015.08.002.

Chapter 4:

**Electrochemical properties
of 2-D Molybdenum
Vanadium Carbide MXene
in various monovalent and
a bivalent cation based
aqueous electrolytes (Li^+ ,
 Na^+ , K^+ and Mg^{2+})**

4.1 Introduction

As highlighted in **chapter 1**, supercapacitors show lower energy densities than batteries. Although pseudocapacitors, such as Ti_3C_2 MXene, exhibits high volumetric capacitances ($>900 \text{ F cm}^{-3}$) than carbon materials ($< 25 \text{ F cm}^{-3}$), the electrochemical cell composed of Ti_3C_2 MXene (as $\text{Ti}_3\text{C}_2//\text{Ti}_3\text{C}_2$) displays a narrow cell voltage of 0.6 V. As, energy has a proportionally with the cell voltage, such narrow cell voltage causes the cell to operate with low volumetric energy density, which eventually limits the use of Ti_3C_2 MXene cell in applications where volumetric energy density of a requisite energy storage is critical. Furthermore, to tackle this problem, it was proposed in **chapter 1** that new MXenes like $\text{Mo}_{2.7}\text{V}_{1.3}\text{C}_3$ is a promising candidate for the positive electrode, thanks to its favorable electrochemical potential window. And, therefore, coupling $\text{Mo}_{2.7}\text{V}_{1.3}\text{C}_3$ with Ti_3C_2 in the asymmetric configuration would further extend the voltage of the MXene based pseudocapacitor cell. Yet, understanding of the electrochemical properties, especially with several cations based electrolyte systems are still required with $\text{Mo}_{2.7}\text{V}_{1.3}\text{C}_3$ MXene. Because the understanding gained with the selection of an appropriate electrolyte system can be useful in assembling cells with better electrochemical performance. Therefore, before assembling the asymmetric $\text{Ti}_3\text{C}_2//\text{Mo}_{2.7}\text{V}_{1.3}\text{C}_3$ cell, we investigate the electrochemical response of $\text{Mo}_{2.7}\text{V}_{1.3}\text{C}_3$ MXene in various monovalent and bi-valent cation, such as Li^+ , Na^+ , K^+ and Mg^{2+} . As, sulfate anion (SO_4^{2-}) shows symmetrical charge density and smaller Cosmo Volume (77.7 \AA^3) compared to other organic anions (eg. TFSI^- , CH_3CO_2^- , $\text{C}_7\text{H}_{12}\text{CO}_2^-$, CH_3SO_3^-) and mineral anions (eg. ClO_4^- and NO_3^-), which is a favorable property in improving the dissolution of aqueous electrolyte system and in-turn its electrochemical property. Therefore, sulfate anion was selected among other anions groups.

In this view, various monovalent cations based electrolytes, eg. 1 M Li_2SO_4 , 1 M Na_2SO_4 , 0.5 M K_2SO_4 and a bivalent cation (1 M MgSO_4) were selected to study the electrochemical properties of $\text{Mo}_{2.7}\text{V}_{1.3}\text{C}_3$ MXene. As a whole, one of the objectives of this chapter is to study the electrochemical properties of $\text{Mo}_{2.7}\text{V}_{1.3}\text{C}_3$ MXene in various monovalent and a bivalent sulfate-based electrolyte.

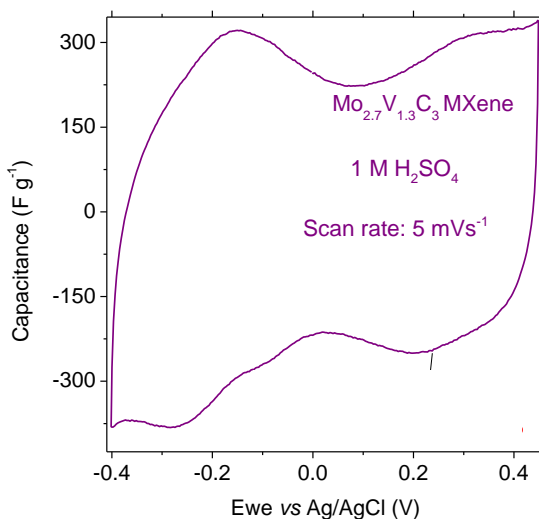


Figure 4. 1. CV curves of $\text{Mo}_{2.7}\text{V}_{1.3}\text{C}_3$ MXene in 1 M H_2SO_4 (in a three-electrode cell configuration)

Besides this objective, as $\text{Mo}_{2.7}\text{V}_{1.3}\text{C}_3$ MXene demonstrated charge storage in the positive potential window (-0.4 V to 0.45 V vs Ag/AgCl, see **figure 4.1**), whereas it well know that the Ti_3C_2 MXene store charges in the negative potential windows (-0.7 V to 0.3 V vs Ag/AgCl). Therefore, $\text{Mo}_{2.7}\text{V}_{1.3}\text{C}_3$ MXene is a potential candidate (as a positive electrode) to couple with the Ti_3C_2 MXene (as a negative electrode) to form a full MXene based device. And, assembly and exhibition of electrochemical properties of such full MXene based cell have been not described so far in the literature. Consequently, after tackling the first objective (the electrochemical behavior of the $\text{Mo}_{2.7}\text{V}_{1.3}\text{C}_3$ MXene), another objective of this chapter is to assemble a

full cell based on $\text{Mo}_{2.7}\text{V}_{1.3}\text{C}_3//\text{Ti}_3\text{C}_2$ MXene with the appropriate selection of the cation (information obtained from objective 1).

Objectives of this chapter

Based on the above discussion, the objectives of this chapter are:

- (i) To evaluate the electrochemical performance of $\text{Mo}_{2.7}\text{V}_{1.3}\text{C}_3$ in various monovalent and a bivalent cation based aqueous electrolytes (Li^+ , Na^+ , K^+ and Mg^{2+})
- (ii) To assemble and evaluate a full cell with Ti_3C_2 and $\text{Mo}_{2.7}\text{V}_{1.3}\text{C}_3$ MXene as a negative and positive electrode, respectively, in the selected electrolyte systems from objective 1.

4.2. Materials and Methods

Preparation of $\text{Mo}_{2.7}\text{V}_{1.3}\text{C}_3$ MXene films¹: The etching of the $\text{Mo}_{2.7}\text{V}_{1.3}\text{AlC}_3$ MAX phases was carried out by following the protocol established for the double transition MAX phases (Anasori *et al.*, 2015). In this protocol, 1 g $\text{Mo}_{2.7}\text{V}_{1.3}\text{AlC}_3$ MAX was added slowly to 10 mL of a 48-51% aqueous solution of HF to chemically etch the aluminum from $\text{Mo}_{2.7}\text{V}_{1.3}\text{AlC}_3$ MAX. The reaction was stirred with a Teflon-bar for 96 h at 50 °C. The resulting products were transferred to a 50 mL centrifugation tube and washed with the deionized water by centrifugation at 3500 rpm, until the pH of the solution was reached to 6-7. The residues of the last wash were dispersed, filtered on a cellulose acetate membrane (Millipore, 0.45 μm pore size) and dried under vacuum at 80 °C, to obtain powders consisting of $\text{Mo}_{2.7}\text{V}_{1.3}\text{C}_3$

¹ These films were obtained as a part of the collaborative project with Prof. Yury Gogotsi of Drexel University. Dr. David Pinto provided these electrode films. The corresponding author of this thesis carried out the electrochemical studies with Dr. David Pinto.

multi-layers. 0.55 M of these powders were further dispersed in an aqueous solution of tetramethylammonium hydroxide (TMAOH, 25 wt.% in water, Sigma-Aldrich) and stirred for 18 h. After this, this slurry was centrifuged and the decantation of the supernatant resulted in sediment. This sediment was washed until the pH of the solution reached 8. With the final decantation, the sediment was redispersed in distilled water, which was later bath-sonicated under argon bubbling for a period of 1 h. This supernatant of the solution was collected in the form of a film using a vacuum-assisted filtration method, where a Celgard® membrane with an average pore size of 64 nm was used as a filter.

4.3. Electrochemical properties of $\text{Mo}_{2.7}\text{V}_{1.3}\text{C}_3$ MXene

4.3.1 Electrochemical potential windows

The CV technique was used to evaluate the electrochemical behavior of the $\text{Mo}_{2.7}\text{V}_{1.3}\text{C}_3$ MXene in various sulfate electrolytes (1 M Li_2SO_4 , 1 M Na_2SO_4 , 1 M MgSO_4 , and 0.5 M K_2SO_4). The CV curve at a scan rate of 5 mV s^{-1} , as shown in **figure 4.2 a**. The CV curves indicate an electrochemical potential window of 0.9 V (from -0.7 to 0.2 V vs Ag/AgCl). This window is larger than the electrochemical potential window of in 1 M H_2SO_4 (as shown in **figure 4.1**. of 0.85 V, from -0.4 V to 0.45 V vs Ag/AgCl). And, to understand this trend, various sulfate electrolytes were protonated with H_2SO_4 acid, up to a similar pH of 2.3. Throughout the discussions, these modified electrolytes were considered as acidified sulfate electrolytes, various non-protonated electrolytes as non-acidified electrolytes. Similar to the case of the non-acidified sulfate electrolytes, CV technique was also applied to observe the electrochemical properties of $\text{Mo}_{2.7}\text{V}_{1.3}\text{C}_3$ MXene in acidified sulfate

electrolytes. The resulting CV curves are shown in **figure 4.2 b**. In this figure, although the electrochemical windows are the widest in acidified electrolytes (0.95 V) when compared to the acidic 1 M H₂SO₄ (0.85 V, as

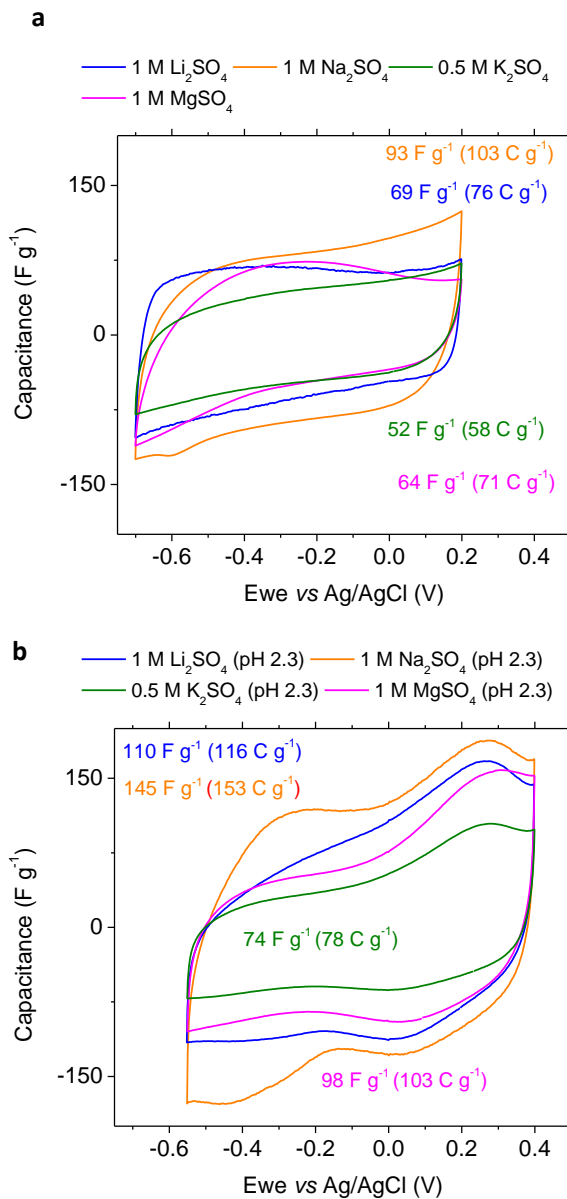


Figure 4. 2. CV curves of Mo_{2.7}V_{1.3}C₃ MXene in (a) non-acidified and (b) acidified sulfate based aqueous electrolytes (in a three-electrode cell configuration)

shown previously in **figure 4.1**), and the non-acidified sulfate electrolytes (0.9 V). The vertex window in acidified sulfate electrolytes is shifted from -0.55 V to 0.4 V vs. Ag/AgCl when compared with that of acidic 1 M H₂SO₄ (0.85 V from -0.4 V to 0.45 V vs. Ag/AgCl), and the non-acidified electrolytes (0.9 V from -0.7 V to 0.2 V vs. Ag/AgCl). The shift of the electrochemical window can be connected with the decrease of pH from the non-acidified electrolyte (neutral, -0.7 V_{negative vertex} vs. Ag/AgCl) when compared with that of the acidified sulfate electrolytes (pH ~ 2.3, -0.55 V_{negative vertex} vs. Ag/AgCl) and highly acidic electrolyte (1 M H₂SO₄, pH ~ 0, -0.4 V_{negative vertex} vs. Ag/AgCl). This shift can be supported through the Nernst equation, which is given as Eq. (5.1)(Li *et al.*, 2018).

$$E_{negative} = -0.059 pH \quad (5.1)$$

Besides this, as (Seh *et al.*, 2016) and (Handoko *et al.*, 2017) has shown with Mo₂C and Mo₂TiC₂, respectively, that Mo-MXene demonstrates low over-potential for HER. Taking this into account, as Mo_{2.7}V_{1.3}C₃ also consists of Mo layers (at least 67 mol. % Mo, based on a solid solution hypothesis, **see chapter 1, figure 1.9**), the higher negative vertex potential in acidic and acidified electrolytes (-0.55 and -0.4 vs Ag/AgCl) can be also accounted to the catalytic properties Mo layers in Mo_{2.7}V_{1.3}C₃ MXene.

4.3.2. Analysis of the charge storage profile

Besides the information related to the electrochemical window, the CV curves in **figure 4.3**, also show dissimilar charge responses between non-acidic and acidic sulfate electrolytes. In case of non-acidic electrolytes (like 1 M Li₂SO₄ and 1 M Na₂SO₄), the CV curves designate a rectangular-like charge profile. Whereas, in the case of acidified electrolytes, non-rectangular like is noted. This behavior is further analyzed by applying the PEIS technique at different electrochemical potential windows and later

analyzing the value of phase angle at 10 mHz. The plot of phase angle versus the electrochemical potential is shown in **figure 4.4**. In case of Na_2SO_4 and Li_2SO_4 electrolytes, a phase angle with a value of $\sim 80^\circ$ and $\sim 75^\circ$, respectively,

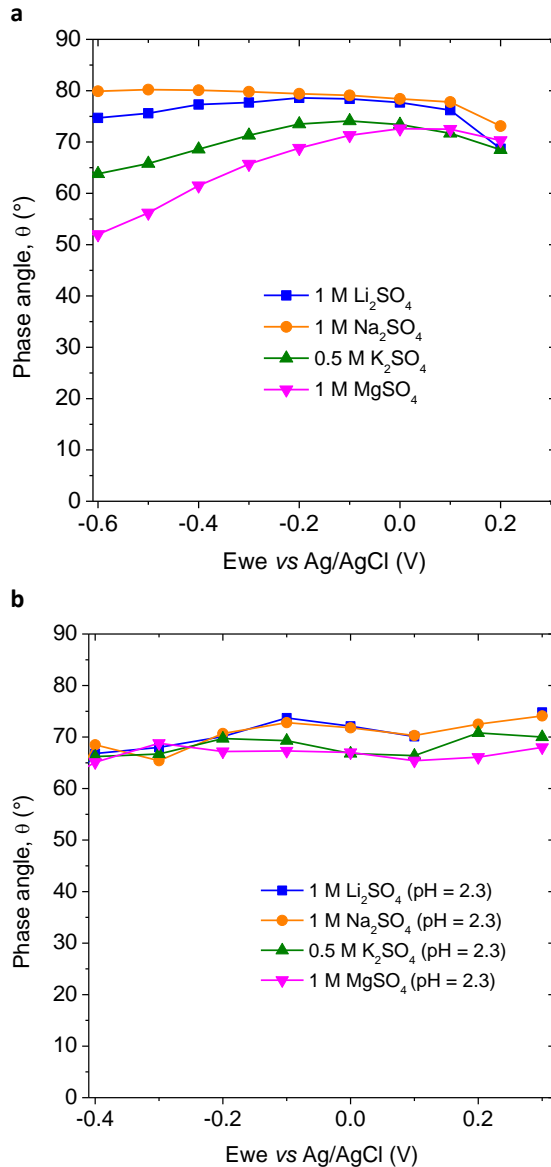


Figure 4. 3. Phase angle versus the electrochemical potential plot of $\text{Mo}_{2.7}\text{V}_{1.3}\text{C}_3$ MXene in (a) non-acidified and (b) acidified sulfate based aqueous electrolytes. The value of the phase angle was taken at 10 mHz

was seen within the potential window (0.1 to -0.6 V vs Ag/AgCl). Such values of the phase angle are close to an ideal capacitive performance (phase angle of 90°). Therefore, the rectangular-like charge profile in case of Na_2SO_4 and Li_2SO_4 (non-acidified) electrolytes can be quantified to EDLC-like charge storage. While in case of K_2SO_4 and MgSO_4 electrolytes, in the negative electrochemical potentials (at -0.6 V vs Ag/AgCl), the value of phase angle decreases to $\sim 65^\circ$ and $\sim 50^\circ$, respectively. Previously, a similar trend was also shown by (Levi *et al.*, 2015) for K^+ and Mg^{2+} ions with Ti_3C_2 MXene. In that case, (Levi *et al.*, 2015) identified this electrochemical behavior as diffusion limitation leading to a quasi-capacitance behavior, which (Levi *et al.*, 2015) pointed to be originated with the steric hindrance of the large size monovalent K^+ and bivalent Mg^{2+} ions during the insertion/de-insertion within the Ti_3C_2 MXene interlayers. Considering the similar behavior in the present case of $\text{Mo}_{2.7}\text{V}_{1.3}\text{C}_3$ MXene, the low value of phase angle with K^+ and Mg^{2+} ions ($\sim 65^\circ$ and $\sim 50^\circ$, respectively) can also attribute with the diffusion limitation of K^+ and Mg^{2+} cations within the interlayer of $\text{Mo}_{2.7}\text{V}_{1.3}\text{C}_3$ MXene. Therefore, quasi-EDLC like behavior can be considered in case of K_2SO_4 and MgSO_4 electrolytes.

Whereas, in the case of acidified electrolytes, two cases are proposed:

- (i) In the positive electrochemical window, at 0.1 vs. Ag/AgCl, the phase angle of $\sim 70^\circ$ was observed for acidified Na_2SO_4 and Li_2SO_4 electrolytes. Whereas, $\sim 65^\circ$ was seen for acidified K_2SO_4 and MgSO_4 electrolytes.
- (ii) In the negative electrochemical window, -0.4 V vs. Ag/AgCl, the phase angle of $\sim 65^\circ$ seen with all acidified electrolytes (Na_2SO_4 , Li_2SO_4 , K_2SO_4 and MgSO_4).

Taking account of the non-rectangular CV curve in positive electrochemical potential of the acidified electrolyte, the prior case can be either related to diffusion limitation or redox couple peaks. As no diffusion limited related to phase angle was observed in case of non-acidified Na_2SO_4 and Li_2SO_4 . And, moreover, previously (Lukatskaya *et al.*, 2017) have shown a decrease of phase angle with the proton redox couple activity with Ti_3C_2 MXene in 1 M H_2SO_4 (Ti-O to Ti-OH redox couple). Therefore, the non-rectangular profile in the positive potential window can be considered as the redox couple peak. The redox couple takes place in the positive potential window when acidified electrolytes are used (acidified electrolytes: Na_2SO_4 , Li_2SO_4 , K_2SO_4 and MgSO_4 , **figure 4.3**; acidic electrolyte: 1 M H_2SO_4 , see also **figure 4.2**). Since features of redox couples are absent in non-acidified sulfate salts, the redox couple can be related to proton interaction with transition metal (M), forming a redox pair (M-O to M-OH) pair. Although further in-depth investigations are still required at this stage to quantify the type of transition metal involved in this redox reaction. On the contrary, considering the case

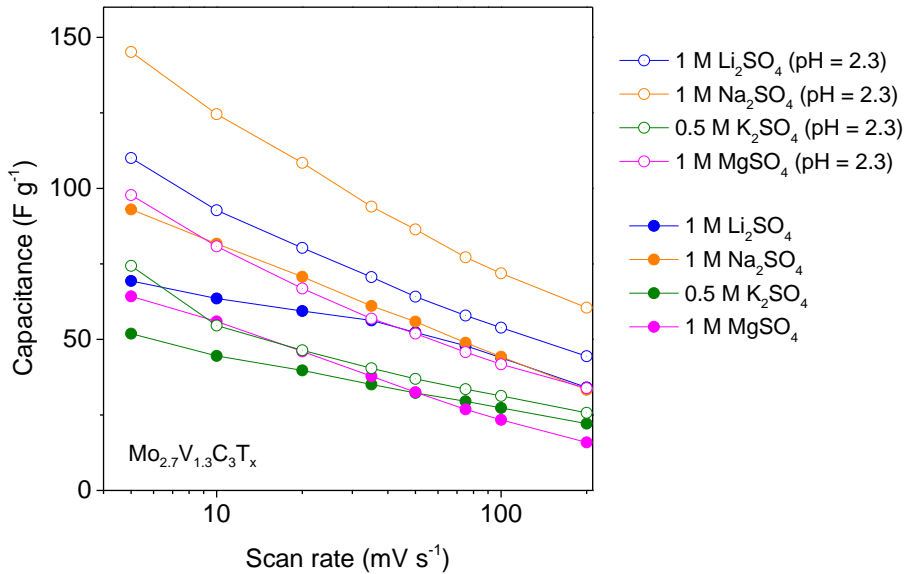


Figure 4. 4. Relationship between capacitance and scan rate

(ii), in which phase of $\sim 65^\circ$ was seen with all acidified electrolytes in the negative electrochemical potential and correlating it with the appearance of the redox peak in the negative potential window (0 and -0.55 V vs. Ag/AgCl) with 1 M H_2SO_4 (**Figure 4.2**), 1 M Na_2SO_4 pH 2.3 and 1 M Li_2SO_4 pH 2.3 (**Figure 4.3**). It can be deduced that the redox peak in the negative potential window is still witnessed with 1 M H_2SO_4 , 1 M Na_2SO_4 pH 2.3 and 1 M Li_2SO_4 pH 2.3. Previously, such redox peaks were seen in the negative potential window with Mo-based MXenes with 1 H_2SO_4 (MoO_{3-x} (Xiao *et al.*, 2014) and Mo_2C (Halim *et al.*, 2016)). Taking this into account, it can be considered that the redox peak on the negative potential window can be attributed to the Mo-O to Mo-OH redox pairs originated with the interaction of protons (H^+). However, with the electrolyte system based on acidified K^+ and Mg^{2+} based sulfate electrolyte, the redox couple related to the Mo-O to Mo-OH transition state disappears. Considering the lower values of phase angle and the absence of redox couples, once again it can be further supported that the Mg^{2+} and K^+ ion are hindered when they interact with $\text{Mo}_{2.7}\text{V}_{1.3}\text{C}_3$ MXene.

In term of performances, the $\text{Mo}_{2.7}\text{V}_{1.3}\text{C}_3$ film evolves from 50 to 95 F g^{-1} at 5 mV s^{-1} in non-acidified sulfate-based electrolytes (**Figure 4.5**). Among this, Na_2SO_4 shows the maximum value of capacitance within all the scan rates (5 to 100 mV s^{-1}), whereas, K_2SO_4 resulted in the lowest. Moreover, as described in the previous paragraphs, the acidification of the sulfate-based electrolyte exposes electrochemical storage *via* redox processes. In such cases, the value of capacitance at 5 mV s^{-1} , to rises to a value of 87 F g^{-1} (225 F cm^{-3}) in K_2SO_4 pH 2.3 to 150 F g^{-1} (410 F cm^{-3}) in Na_2SO_4 pH 2.3. Since Na-based electrolytes have shown higher values of charge storage, $\text{Mo}_{2.7}\text{V}_{1.3}\text{C}_3$ was coupled with Ti_3C_2 MXene in Na-based electrolytes (both non-acidic and acidic electrolytes).

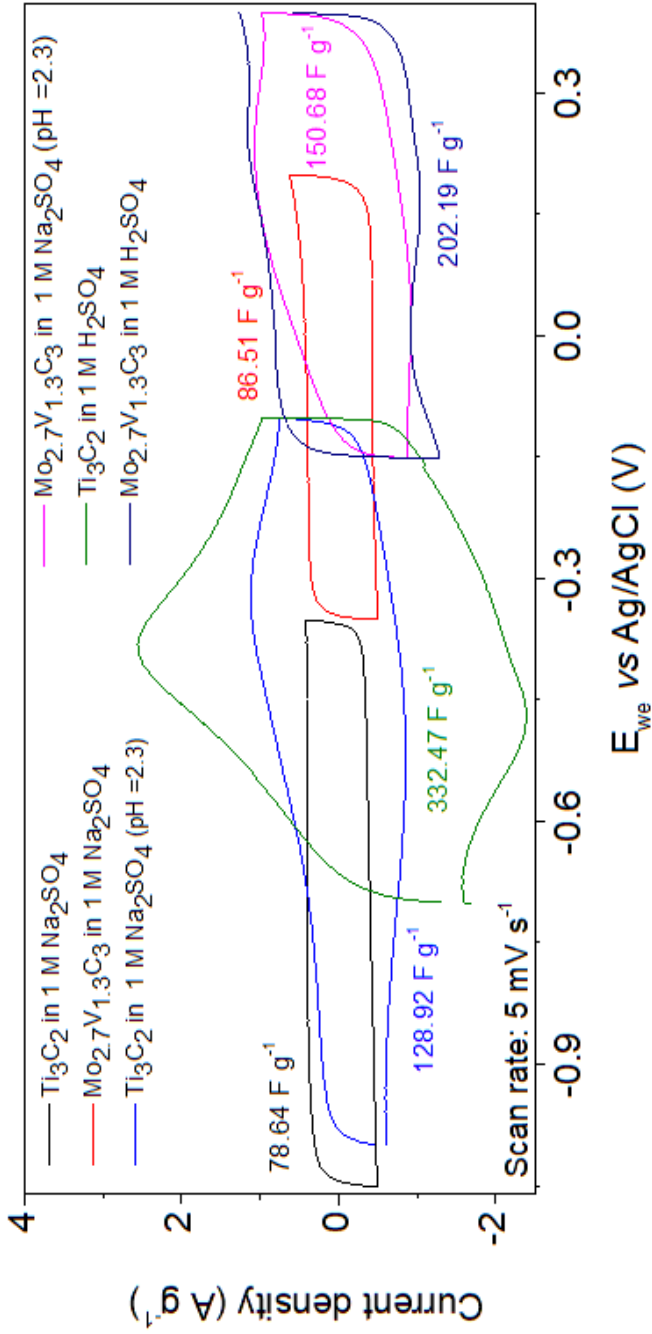


Figure 5.5. CV curves of Ti_3C_2 and $\text{Mo}_{0.7}\text{V}_{1.3}\text{C}_3$ MXene in non- and acidified Na-sulfate based aqueous electrolytes and as well as in sulfuric acid (in a three-electrode cell configuration)

4.4. Demonstration of all MXene pseudocapacitors using 2-D Titanium Carbide MXene and Molybdenum Vanadium Carbide MXene

Taking advantage of the negative electrochemical window of Ti_3C_2 MXene, $\text{Mo}_{2.7}\text{V}_{1.3}\text{C}_3$ is coupled with Ti_3C_2 electrode, as shown in **figure 4.5**. The mass-balancing approach was taken into account for the assembly of the asymmetric $\text{Ti}_3\text{C}_2//\text{Mo}_{2.7}\text{V}_{1.3}\text{C}_3$ cell, an occurrence of the uneven value of

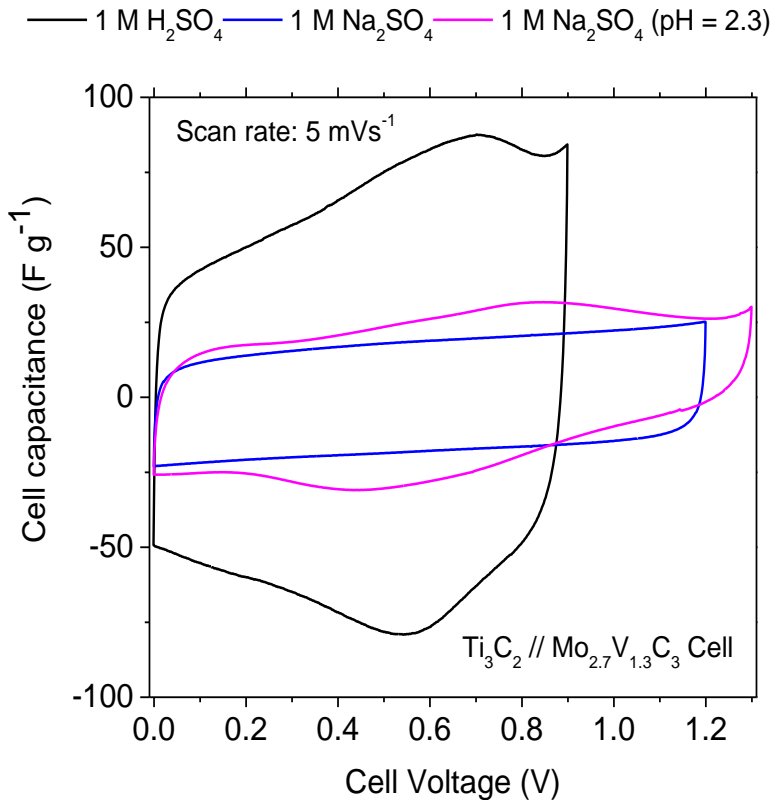


Figure 4. 6. CV curves of asymmetric $\text{Ti}_3\text{C}_2 // \text{Mo}_{2.7}\text{V}_{1.3}\text{C}_3$ MXene Cell in non- and acidified Na-sulfate based aqueous electrolytes and as well as in sulfuric acid (in two electrode cell configuration)

charge storage between the Ti_3C_2 and $\text{Mo}_{2.7}\text{V}_{1.3}\text{C}_3$ electrode was seen. This can be given by:

$$R = \left(\frac{m_+}{m_-} \right) = \left(\frac{C_- \Delta V_-}{C_+ \Delta V_+} \right), \quad (5.2)$$

where m_+ and m_- represent the mass, C_+ and C_- the capacitance, and ΔV_+ and ΔV_- the potential window of the positive and negative electrode, respectively. In the case of non-acidified and acidified 1 M Na_2SO_4 electrolyte, the value of R was 1.2 and 3.6, respectively. Although the values of the capacitance in both Ti_3C_2 and $\text{Mo}_{2.7}\text{V}_{1.3}\text{C}_3$ electrodes are lower in both non-acidified and acidified 1 M Na_2SO_4 electrolyte when compared with the capacitances obtained in 1 M H_2SO_4 electrolyte. The larger potential windows in non-acidified and acidified 1 M Na_2SO_4 electrolyte are a favorable parameter, as it results in the asymmetric cell with wider cell voltages. Therefore, cell assembly with non-acidified and acidified 1 M Na_2SO_4 electrolyte were still taken into account. Also, for electrochemical comparative purposes, $\text{Ti}_3\text{C}_2//\text{Mo}_{2.7}\text{V}_{1.3}\text{C}_3$ cell was also assembled with 1 M H_2SO_4 electrolyte. Considering the Eq. 5.2, the value of R was 1.3. The CV technique was also applied to observe the charge storage of the asymmetric $\text{Ti}_3\text{C}_2//\text{Mo}_{2.7}\text{V}_{1.3}\text{C}_3$ cell and the obtained curves are shown in **figure 4.6**. In the case of non-acidified Na_2SO_4 electrolyte, the CV curve shows a maximal cell voltage of 1.2 V with an EDLC-like charge response. While in acidic 1 M Na_2SO_4 electrolyte a maximum cell voltage of 1.3 V was obtained, with redox peak featuring between 0.4 and 0.9 V. Similarly, such redox peak was also observed in the case of H_2SO_4 electrolytes. Long term cycling studies of the $\text{Ti}_3\text{C}_2//\text{Mo}_{2.7}\text{V}_{1.3}\text{C}_3$ cell at a scan rate of 50 mVs^{-1} over 9,000 cycles, as shown in **figure 4.7**, indicates capacitance retention of 82 % in 1 M H_2SO_4 , whereas 92% and 94% for non- and acidified electrolytes, respectively. Although once

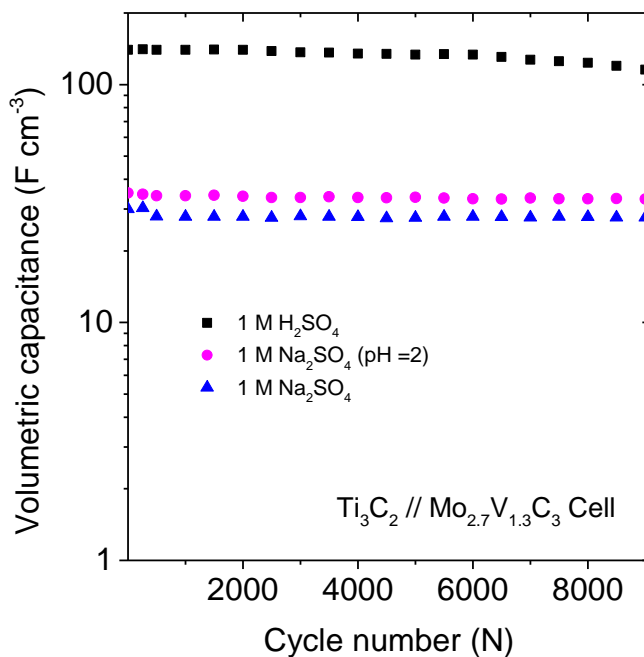


Figure 5. 7. Long term cycling of asymmetric $Ti_3C_2 // Mo_{2.7}V_{1.3}C_3$ MXene Cell in non- and acidified Na-sulfate based aqueous electrolytes and as well as in sulfuric acid (in two electrode cell configuration) at a scan rate of 50 mVs^{-1} .

again further in-depth studies are required to understand the degradation mechanism of the $Ti_3C_2 // Mo_{2.7}V_{1.3}C_3$ cell in $1 \text{ M H}_2\text{SO}_4$. But, we hypothesize that the lower value of capacitance retention in $1 \text{ M H}_2\text{SO}_4$, could be attributed to the structural instability of the vanadium at low pH ($1 \text{ M H}_2\text{SO}_4$ pH ~ 0), which was also seen during the long term cycling of the individual $Mo_{2.7}V_{1.3}C_3$ electrode (*see Appendix C*). Nevertheless, the capacitance values at the initial cycles during the cycling tests at 50 mVs^{-1} reveals that the $Ti_3C_2 // Mo_{2.7}V_{1.3}C_3$ cell shows a high value of volumetric capacitance of 140 F cm^{-3} in $1 \text{ M H}_2\text{SO}_4$, followed by 35 F cm^{-3} and 30 F cm^{-3} in acidified and non-acidified sodium based electrolytes. These volumetric capacitances are higher than the value usually observed with carbon-based supercapacitors ($< 25 \text{ F cm}^{-3}$). Such remarkable properties of the $Ti_3C_2 // Mo_{2.7}V_{1.3}C_3$ cell

indicate a promising use in the applications where volume energy densities of the supercapacitors device are critical.

4.5. Conclusions

In this chapter, the electrochemical properties of the $\text{Mo}_{2.7}\text{V}_{1.3}\text{C}_3$ MXene were studied in various non-acidified and acidified sulfate based electrolytes with an objective of choosing the best performing electrolyte system to assemble an asymmetrical cell of $\text{Ti}_3\text{C}_2//\text{Mo}_{2.7}\text{V}_{1.3}\text{C}_3$ MXene. Cyclic voltammetry reveals that the $\text{Mo}_{2.7}\text{V}_{1.3}\text{C}_3$ MXene show EDLC-like charge storage in non-acidified Li_2SO_4 and Na_2SO_4 based electrolytes. While quasi-EDLC-like electrochemical behavior with non-acidified K_2SO_4 and MgSO_4 electrolytes. Analysis through impedance spectroscopy indicates that, unlike in Li_2SO_4 and Na_2SO_4 based electrolytes, ions of K_2SO_4 and MgSO_4 electrolytes suffers from hindrance effect while interacting with $\text{Mo}_{2.7}\text{V}_{1.3}\text{C}_3$ MXene. This behavior was related to the large size of both K^+ and Mg^{2+} ions. Moreover, the absence of the redox activity related to the Mo-O to Mo-OH transition state of $\text{Mo}_{2.7}\text{V}_{1.3}\text{C}_3$ MXene in acidified K^+ and Mg^{2+} ions containing electrolytes also supported the hindrance effect K^+ and Mg^{2+} ions. Furthermore, due to the electrochemical charge storage of $\text{Mo}_{2.7}\text{V}_{1.3}\text{C}_3$ MXene in the potential windows, $\text{Mo}_{2.7}\text{V}_{1.3}\text{C}_3$ MXene was noted as a favorable material for the positive electrode. And, the coupling of $\text{Mo}_{2.7}\text{V}_{1.3}\text{C}_3$ (as a positive electrode) with the Ti_3C_2 (as a negative electrode) enables a first full MXene based cell. This symmetric $\text{Ti}_3\text{C}_2//\text{Mo}_{2.7}\text{V}_{1.3}\text{C}_3$ cell configuration shows an extended cell voltage (0.9 to 1.3 V) depending on the nature of aqueous electrolytes, with good capacitance retention from 82 to 98 % over 10,000 cycles. Besides this, $\text{Ti}_3\text{C}_2//\text{Mo}_{2.7}\text{V}_{1.3}\text{C}_3$ cell shows higher volumetric capacitances ($30\text{-}140\text{ F cm}^{-3}$) than carbon based EDLCs. However, it is worthy to note that the maximum cell voltages obtained with $\text{Ti}_3\text{C}_2//\text{Mo}_{2.7}\text{V}_{1.3}\text{C}_3$ cell

(0.9 to 1.3) were still lower than that of the organic electrolyte based supercapacitors (> 2.3 V) and further work in the direction of increasing the cell voltages are needed.

4.6 References

Anasori, B. *et al.* (2015) 'Two-Dimensional, Ordered, Double Transition Metals Carbides (MXenes)', *ACS Nano*, 9(10), pp. 9507–9516. doi: 10.1021/acsnano.5b03591.

Halim, J. *et al.* (2016) 'Synthesis and Characterization of 2D Molybdenum Carbide (MXene)', *Advanced Functional Materials*, 26(18), pp. 3118–3127. doi: 10.1002/adfm.201505328.

Handoko, A. D. *et al.* (2017) 'Tuning the Basal Plane Functionalization of Two-Dimensional Metal Carbides (MXenes) To Control Hydrogen Evolution Activity', *ACS Applied Energy Materials*, 1(1), pp. 173–180. doi: 10.1021/acsaem.7b00054.

Levi, M. D. *et al.* (2015) 'Solving the Capacitive Paradox of 2D MXene using Electrochemical Quartz-Crystal Admittance and In Situ Electronic Conductance Measurements', pp. 1–11. doi: 10.1002/aenm.201400815.

Li, Y. *et al.* (2018) 'Design and Mechanisms of Asymmetric Supercapacitors', *Chemical Reviews*. American Chemical Society, 118(18), pp. 9233–9280. doi: 10.1021/acs.chemrev.8b00252.

Lukatskaya, M. R. *et al.* (2017) 'Ultra-high-rate pseudocapacitive energy storage in two-dimensional transition metal carbides', *Nature Energy*, 6. doi: 10.1038/nenergy.2017.105.

Seh, Z. W. *et al.* (2016) 'Two-Dimensional Molybdenum Carbide (MXene) as an Efficient Electrocatalyst for Hydrogen Evolution', *ACS Energy Letters*, 1(3), pp. 589–594. doi: 10.1021/acsenerylett.6b00247.

Xiao, X. *et al.* (2014) 'Freestanding MoO_{3-x} nanobelt/carbon nanotube films for Li-ion intercalation pseudocapacitors', *Nano Energy*, 9, pp. 355–363. doi: 10.1016/j.nanoen.2014.08.001.

Chapter 5:
Building High-Voltage
aqueous pseudocapacitors
using water-in-salt electrolytes

5.1 Introduction

As highlighted in the *section 1.4.2* of the introduction, most known aqueous pseudocapacitors exhibit narrow nominal voltages (1.2 to 1.4 V) than organic electrolyte based carbon-based supercapacitor (2.3 to 2.7 V). Therefore, as mentioned in *section 1.4.2*, my approach to this issue was to implement super-concentrated solutions, like water-in-salt solution as an electrolyte media. As water-in-salt electrolytes exhibit wider stability in terms of electrochemical potential windows, thanks to this wider nominal voltage could be achieved in aqueous pseudocapacitors. This way, aqueous pseudocapacitors could exhibit high volumetric energy densities, which remains un-investigated. And thereafter, could allow aqueous pseudocapacitors to be used in applications where the size of the electrochemical device is crucial. Therefore, the main objective of this chapter is to use the water-in-salt electrolytes for building high-voltage supercapacitors.

5.1.1. Existing works

Towards this direction, in terms of the existing literature, (Gambou-Bosca and Bélanger, 2016) used an aqueous 21 m of Li-TFSI (a water-in-salt electrolyte) to the extent the electrochemical potential window of the pseudocapacitive materials like MnO_2 up to 1.4 V. According to (Gambou-Bosca and Bélanger, 2016), such potential window was previously limited to 1.0 V in standard aqueous solutions or salt-in-water electrolytes (5 M of aqueous LiNO_3). However, the main drawback of their results was related to the rate capability of MnO_2 , which is the capacitance observed at high to low charging or discharging rate. (Gambou-Bosca and Bélanger, 2016) mentions that the rate capability of MnO_2 was lower than 20% when 21 m of Li-TFSI (< 20%) was used as an electrolyte solution. Which, according to

(Gambou-Bosca and Bélanger, 2016) was lower than the values observed for MnO₂ in salt-in-water electrolytes (> 45%). (Gambou-Bosca and Bélanger, 2016) suggests that for MnO₂ electrode, such a fast decay is attributed to the lower ionic conductivity of 21 m Li-TFSI (< 3 mS cm⁻¹), over salt-in-water electrolytes (> 50 mS cm⁻¹). According to (Dou *et al.*, 2018; Wang *et al.*, 2018), the low ionic conductivity of 21 m Li-TFSI is endorsed to the strong electrostatic interaction between cation and anion in their cation-anion complex form, which is represented as Li⁺(H₂O)_{2.5} Li⁺(TFSI⁻)_x (with $x > 1$, also a possibility of $x = 2$, see **section 1.4.2** for further understanding about the cation-anion complex).

To resolve the low ionic conductivities of water-in-salt electrolytes, several research groups also carried out a new investigation in the direction of better water-in-salt electrolyte formulations. In this sense, investigation on new electrolyte formulations, such as hydrate melts of mixed cations (Suo *et al.*, 2016), organic co-solvent water-in-salts (Dou *et al.*, 2018; Wang *et al.*, 2018) and mixed cation water-in-salts (Lukatskaya *et al.*, 2018) have shown to reduce the strong interaction between the cation and anion. Therefore, the use of such new electrolyte formulation appears to be interesting for tackle the high capacitance fade of MnO₂ in water-in-salt electrolytes. However, in the view of (Dou *et al.*, 2018), the ionic conductivities of these newly formulated electrolytes are still lower than 10 mS cm⁻¹, indicating the need of new strategies in the electrolyte formulations, especially in the direction of having low interaction between cation and anions.

5.1.2. Potassium acetate as water-in-salt electrolyte

Very recently (Daniel P. Leonard *et al.*, 2018; Lukatskaya *et al.*, 2018) indicated a super-concentrated potassium acetate as a promising water-in-

salt electrolyte for Potassium ion batteries. According to (Daniel P. Leonard *et al.*, 2018; Lukatskaya *et al.*, 2018), a potassium acetate based water-in-salt electrolyte exhibits higher ionic conductivity ($> 20 \text{ mS cm}^{-1}$) than Li-TFSI organic co-solvent water-in-salt electrolytes (Daniel P. Leonard *et al.*, 2018). Although valid reasoning behind the rise of the ionic conductivity and as well as the formation of the SEI is unknown to date and further investigations in these directions are explored by several groups in the community. But (Daniel P. Leonard *et al.*, 2018) hypothesized that the weak Lewis acidity of potassium ions and/or the weak interaction of acetate anion in the potassium acetate based water-in-salt electrolytes could be a reason behind the high ionic conductivities of potassium acetate based water-in-salt electrolyte. Nevertheless, considering this discussion, the use of potassium acetate based water-in-salt electrolyte appears to be promising to improve the rate capability of pseudocapacitive materials like MnO_2 . Therefore, one of the objectives of this chapter is to use the potassium acetate solution as a water-in-salt electrolyte media. Moreover, according to (Van Der Sluys, 2009) it is also important to consider the lattice energy of the salt (ionic bonding interactions in the salt), as salts with lower lattice energies offer a higher amount of solubility. Taking this into account, as the lattice energy of potassium acetate salt (682 kJ mol^{-1}) is lower than other monovalent and divalent cation based acetate salts (such as sodium acetate = 763 kJ mol^{-1} , calcium acetate = 2294 kJ mol^{-1} , Zinc acetate = 2750 kJ mol^{-1} (Van Der Sluys, 2009)), only potassium acetate based water-in-salt electrolyte were taken into account for the investigation.

Apart from this, very recently (Lannelongue *et al.*, 2018) showed through Li-TFSI based water-in-salt electrolytes that the tradeoff between the ionic conductivity and concentration is an important parameter in water-in-salt

electrolytes to have to achieve high power and energy density. Therefore, beyond using the potassium acetate solution as a water-in-salt electrolyte, it is also important to select an appropriate concentration of potassium acetate based water-in-salt solutions in which high charge storage can be witnessed, in order to achieve both high power and energy densities.

5.1.3. Why tunnels structures of Manganese Oxide are interesting?

Beyond identifying the ideal formation for the water-in-salt electrolyte, the selection of a proper electrode material could be another way for achieving high rate capability in pseudocapacitors. So, far only MnO_2 was the first one to be reported to show pseudocapacitance in the water-in-salt electrolytes

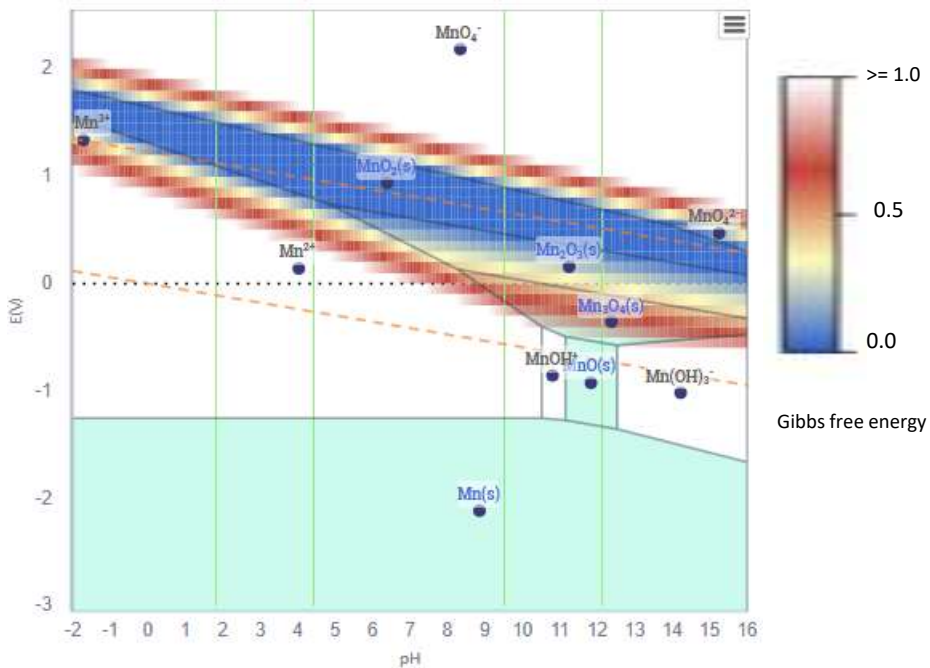


Figure 5. 1. Pourbaix Diagram of MnO_2 , generated using the database of Materialsproject.org. Pourbaix Diagram represents the potential/pH diagram which maps the possible stable equilibrium phases of materials in an aqueous electrochemical system

(Gambou-Bosca and Bélanger, 2016; Zhang *et al.*, 2018). According to (Young *et al.*, 2015), the electrochemical properties of MnO_2 varies significantly between the type of MnO_2 polymorph as well as with the

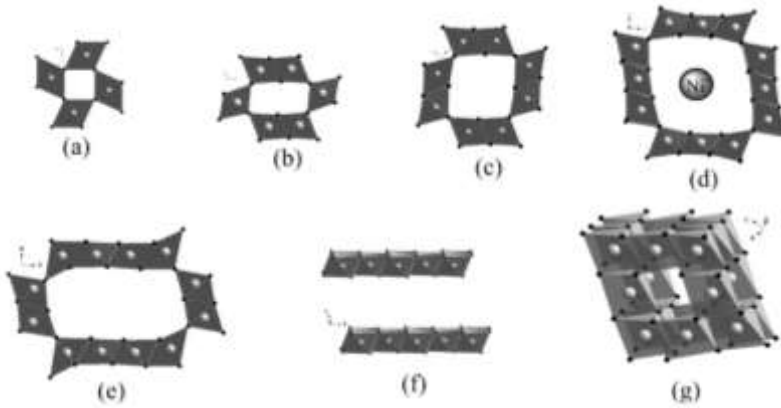


Figure 5. 2. Shows the crystallographic structures of MnO_2 pyrolusite (a), ramsdellite (b), cryptomelane (c), Ni-todorokite (d), OMS-5 (e), birnessite (f), and spinel (g). This figure is adapted from (Ghodbane, Pascal and Favier, 2009) with permission from American Chemical Society.

solution used as an electrolyte media. There are many polymorphs of MnO_2 whose crystal structures differ in the arrangement of MnO_6 octahedra. According to (Ghodbane, Pascal and Favier, 2009), a different arrangement of MnO_6 octahedra shows crystal structures in MnO_2 , such as tunnel and layered. Some examples are shown in **figure 5.1**. Among, layered and tunnel phases of MnO_2 , according to (Ghodbane, Pascal and Favier, 2009), tunnel phases can be adjusted in terms of the tunnel length and breath, which gives a degree of freedom to control the electrochemical properties. Since several polymorphs exist for tunnel MnO_2 , it also appears to be important to select a MnO_2 tunnel phase that can demonstrate high rate capability in potassium acetate based water-in-salt electrolyte. Considering this, apart from using potassium acetate as a water-in-salt electrolyte, electrochemical

screening of several tunnel polymorphs of MnO_2 in potassium acetate based electrolyte is also an objective of this chapter.

5.1.4. Why the use of 2-D Titanium Carbide MXene is interesting?

Although, MnO_2 is a promising candidate for the electrode material. The formation of dissolvable species (Mn^{2+}) within the negative potentials (vs NHE) (Young *et al.*, 2015), limits the usage of MnO_2 only in the positive electrochemical potential windows (vs NHE). The example of the formation of Mn^{2+} species is shown through Pourbaix Diagram (**figure 5.2**). Therefore, it is important to use a material which shows pseudocapacitive behavior in negative potentials, which would allow designing an asymmetric supercapacitor with an expanded voltage window. Considering this, a 2-D MXene such as Ti_3C_2 is a promising electrode material to pair with MnO_2 , as it demonstrates high electronic conductivity ($> 5,000 \text{ S cm}^{-1}$) and exhibits high volumetric capacitance in a negative electrochemical windows vs Ag/AgCl ($900\text{-}1,500 \text{ F cm}^{-3}$) (Naguib *et al.*, 2011; Naguib and Gogotsi, 2015; Alhabeab *et al.*, 2017). Besides this, electrode films made up of Ti_3C_2 MXenes exhibits electrode densities. For example, (Ghidui *et al.*, 2015) showed that a $5 \mu\text{m}$ thick film of Ti_3C_2 MXene possesses an electrode density between 3.6 and 3.8 g cm^{-3} . If such a high-density electrode material is used, the geometrical volume of the pseudocapacitor devices can also be reduced. Such shrinkage could allow pseudocapacitors to be used in the application where the volume of the device is critical (eg. hand drillers). Taking into account of these noteworthy properties, the use of Ti_3C_2 MXene as a negative electrode and coupling it with the positive MnO_2 electrode in a potassium acetate based water-in-salt electrolyte could facilitate a high-voltage pseudocapacitor, which remains, unexplored. Therefore, besides using potassium acetate water-in-salt electrolyte and selection of different

tunnel phases of MnO_2 , the use of 2-D Ti_3C_2 MXene as an electrolyte material is an objective of this chapter. Moreover, as such an electrochemical pseudocapacitive cell have not been shown before, it is also interesting to understand its electrochemical properties and compare its performances with the carbon-based double layer supercapacitors. Bearing this in mind, another objective of this chapter is also to evaluate the electrochemical performances of 2-D $\text{Ti}_3\text{C}_2//\text{MnO}_2$ pseudocapacitive cell ($//$ symbol indicates the cell configuration between negative and positive electrode) and compare its electrochemical performances with carbon-based double layer supercapacitors.

5.1.5. Objectives of this chapter

The following are the objectives of this chapter:

- (i) is to select an appropriate concentration of potassium acetate based water-in-salt electrolyte in which high charge storage properties can be achieved in the pseudocapacitive materials.
- (ii) after identifying an appropriate concentration of the potassium acetate based water-in-salt electrolyte from the objective (i), evaluate the charge storage performance of several tunnel-shaped polymorphs of MnO_2 .
- (iii) with a selection of the MnO_2 phase from the objective (ii), build an electrochemical cell with 2-D Ti_3C_2 MXene.
- (iv) is to evaluate the electrochemical performances of the 2-D Ti_3C_2 MXene// MnO_2 cell and compare it with carbon-based double layer capacitors.

5.2. Synthesis and characterization

5.2.1. Preparation of potassium acetate based water-in-salt electrolytes

As highlighted by (Lannelongue *et al.*, 2018), the tradeoff between ionic conductivity and concentration is an important parameter in water-in-salt electrolytes, therefore different concentrations of water-in-salt solutions were taken in account for the experimental analysis. Namely, 21, 25 and 30 m and their properties were compared with classical salt-in-water electrolytes (1 m). As shown by (Daniel P Leonard *et al.*, 2018) that huge shifts in the potential of hydrogen evolution reaction begin to occur below the molalities of 21 potassium acetate electrolytes, therefore, the electrolyte concentrations below 21 m were not accounted during this investigation. The stoichiometric amount of anhydrous potassium acetate salt was dissolved in Ar-bubbled deionized water via magnetic stirring until a homogeneous solution was obtained. The amount of anhydrous potassium acetate salt in the water is shown in **table 5.1**. This table indicates the content of the potassium acetate salt in 21, 25 and 30 m of potassium acetate water-in-salt electrolyte. By, reducing the molality from 21 to 30 m, the salt wt. % decreases from 74.71 to 71.12 % and 67.40 %, respectively. Whereas, the ratio of salt to water mass reduces from 2.95 to 2.46 and 2.06. As these solutions qualify the definition of water-in-salt, which is when the wt. % of salt is greater than 50 % or when the mass ratio of salt to water is greater than unity (Lannelongue *et al.*, 2018), the prepared solutions with 21, 25 and 30 m can be considered as the water-in-salt electrolytes.

Molality, m (mol kg ⁻¹)	Salt wt. %	Mass _{salt} /Mass _{water}
1	8.962	0.098
21	67.398	2.067
25	71.107	2.461
30	74.705	2.953

Table 5. 1. Salt concentration in water-in-salt solution

5.2.2 Synthesis and characterization of Manganese Oxide tunnel phases

As mentioned in the introduction, among known materials which store charges through a pseudocapacitive mechanism in the positive electrochemical potentials, only MnO₂ has been reported to show pseudocapacitance in the water-in-salt electrolytes (Gambou-Bosca and Bélanger, 2016), (Zhang *et al.*, 2018). As the tunnel size in MnO₂ plays a major role in capacitance storage and the rate decay (as discussed in the introduction of this chapter), three different tunnel dimensions were explored. For the explored tunnel phases, increasing tunnel sizes, 1 x 1, 2 x 2 and 3 x 3 tunnels which were labeled as β -MnO₂, α -MnO₂ and Todorokite-MnO₂ were taken into account. The size of the tunnels was expanded by a stabilizing cation 'A' following a hydrothermal route, which is described in the following section.

5.2.2.1. Material Synthesis¹

β -MnO₂: β -MnO₂ were synthesized following a previous report (Yao *et al.*, 2018). 11.5 mL of a mixed solution of 0.1M (NH₄)₂S₂O₈ and 0.1M MnSO₄·H₂O

¹ This work was carried out as a part of a collaboration with Prof. Pomerantseva Ekaterina group at Drexel University. These materials were prepared by Dr. Bryan Byles. To keep the reader in the context of this investigation, the synthesis route of the materials were described.

was added to a 23 mL Teflon-lined stainless steel autoclave (Parr Instruments) and hydrothermally treated for 12 h at 150 °C. The resulting product (β - MnO_2) was then filtered, washed, and dried at 100 °C for 12 h.

α - MnO_2 : α - MnO_2 were prepared via a previously described method (Byles *et al.*, 2016). 316 mg of KMnO_4 and 108 mg of NH_4Cl were dissolved in 100 mL of deionized water, and 20 mL of this solution was added to a 23 mL Teflon-lined stainless steel autoclave. The autoclave was placed in an oven at 150 °C for 48 h, after which the product (α - MnO_2) was filtered, washed, and dried at 100 °C for 12 h.

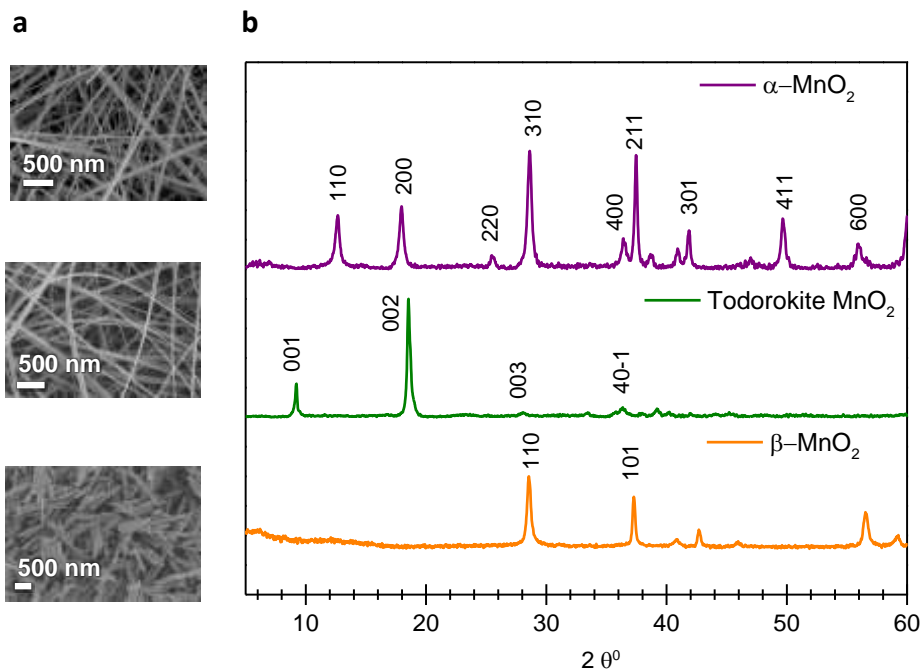


Figure 5. 3. (a) Scanning Electron Microscope images of: (top to bottom) α - MnO_2 (2 x 2 MnO_2), Todorokite- MnO_2 (3 x 3 MnO_2), β - MnO_2 (1 x 1 MnO_2) and their (b) XRD patterns.

Todorokite MnO₂: Manganese oxide with todorokite crystal structure was also synthesized via a previously described method (Byles *et al.*, 2018). Na-birnessite, the precursor material, was prepared via a precipitation reaction described elsewhere (Feng *et al.*, 2015). Then, a solution of 0.6 M NaOH and 2 M H₂O₂ (100 mL) was added dropwise to a 50 mL solution of 0.3 M Mn(NO₃)₂ under stirring. After washing and filtering, Na-birnessite was transferred in a 1 L 1 M MgCl₂ solution for ion exchange. After 24 h of stirring in solution, the product was filtered out and placed in a fresh 1 L solution of 1 M MgCl₂ for an additional 24 h, resulting in a total ion exchange time of 48 h, ensuring conversion of the Na-birnessite into Mg-buserite. After filtering out of solution, 50 mg of the Mg-buserite was added to 17 mL of 1M MgCl₂ in a 23 mL Teflon-lined stainless steel autoclave. The autoclave was placed in an oven at 220 °C for 96 h, and the resulting product (todorokite MnO₂) was then filtered, washed, and dried at 100 °C for 12 h.

5.2.2.2. Material Characterization²

The final composition of the hydrothermal reaction leads to an A_xMnO₂ chemical composition, where x represents the A: Mn ratio. Previously (Byles and Pomerantseva, 2016) used Energy-dispersive X-ray spectroscopy (EDS) on these tunnels phases to quantify the amount of A content in the A_xMnO₂ chemical composition. For the sake of clarification to the reader, this content is mentioned as follows: Magnesium ions (Mg²⁺) were used to produce the 3 x 3 MnO₂ structure forming biggest tunnels with a chemical composition of Mg_{0.20}MnO_{2-δ} (Byles and Pomerantseva, 2016) and,

² This work was carried out as a part of a collaboration with Prof. Pomerantseva Ekaterina group at Drexel University. The characterization data was provided by Dr. Bryan Byles of Prof. Pomerantseva Ekaterina group at Drexel University. However, the data analysis is carried out by the corresponding author of this manuscript. To keep the reader in the context of this investigation, the characterization data related the materials is added.

potassium ions (K^+) to form an intermediate tunnel of 2×2 size with a chemical composition of $K_{0.11}MnO_{2.8}$ (Byles and Pomerantseva, 2016). Whereas, the smallest tunnels size of 1×1 was achieved without stabilizing of cations (MnO_2). For the ease in comparison, 1×1 , 2×2 and 3×3 MnO_2 are denoted as β - MnO_2 , α - MnO_2 , and Todorokite- MnO_2 , respectively.

SEM images for all phases are shown in **figure. 5.3 a**. These images depict a morphology of nanowires for α - MnO_2 and Todorokite- MnO_2 , whereas nanorods for β - MnO_2 . XRD patterns of β - MnO_2 , α - MnO_2 , and Todorokite- MnO_2 are shown in **figure. 5.3 b**. The patterns of β - MnO_2 , α - MnO_2 and Todorokite- MnO_2 were indexed to tetragonal $I4/m$ phase (JCPDS card # 44-014), tetragonal $P4_2/mnm$ (JCPDS card # 24-0735), and monoclinic $P2/m$ phase (JCPDS card # 38-475), respectively. XRD pattern of β - MnO_2 was characterized by (110) and (101) reflections at $\sim 28^\circ$ and $\sim 39^\circ$ (2Θ), respectively. Such reflections imply a d-spacing of ~ 2.3 Å and a tunnel length equivalent to one MnO_6 octahedra. These results indicate the existence of 1×1 tunnel, with a dimension of $\sim 2.3 \times 2.3$ Å. Whereas α - MnO_2 shows (110) peak at $\sim 12.7^\circ$ (2Θ), designated to a d-spacing of ~ 7.0 Å. Such metrics are correlated to a length of two octahedra. Besides, non-existence of intense peaks below 12° (2Θ) suggests the absence of a tunnel side larger than two octahedra (Byles *et al.*, 2018). This observation refers to 2×2 tunnel with an aspect of $\sim 7.0 \times 7.0$ Å. Finally, in Todorokite- MnO_2 , (001) peak at $\sim 9.2^\circ$ (2Θ) shows a tunnel size identical to the three MnO_6 octahedra (d-spacing of ~ 9.6 Å), which point out the presence of 3×3 tunnels ($\sim 9.6 \times 9.6$ Å). These findings are in agreement with the previous works (Byles *et al.*, 2018). The above analysis stipulates the presence of three different phases, whose tunnels are in units of MnO_2 : 1×1 in (not stabilized)

β - MnO_2 , 2×2 in α - MnO_2 ($\text{K}_{0.11}\text{MnO}_{2-\delta}$), and 3×3 in Todorokite- MnO_2 ($\text{Mg}_{0.20}\text{MnO}_{2-\delta}$).

The above-mentioned phases of MnO_2 are used as an active material was mixed with a conductive carbon additive (AB, Acetylene Black) and binder (polytetrafluoroethylene, PTFE) in the mass ratio of 75:20:5, respectively. The mixture was mixed with a low volume of ethanol and the resulting

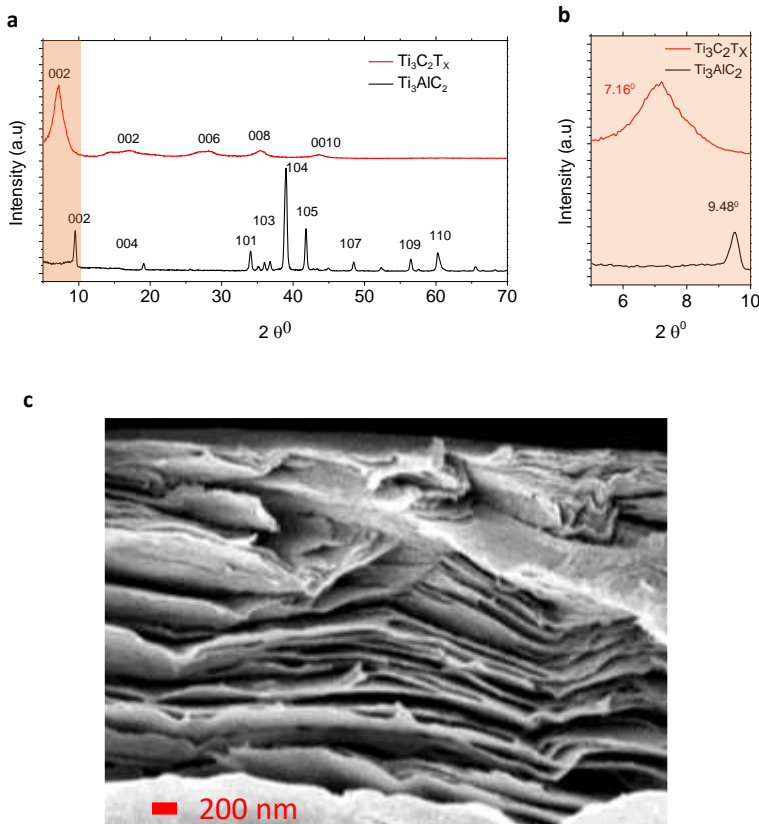


Figure 5. 4. (a) X-Ray Diffraction pattern of Titanium Aluminum Carbide (Ti_3AlC_2 MAX) grains and Titanium Carbide (Ti_3C_2 MXene) film. (b) Zoom of the highlighted X-Ray Diffraction pattern, indicating a shift of (002) reflection peak after etching Ti_3AlC_2 MAX phase (c) SEM image of a Ti_3C_2 MXene film after etching.

slurry was heated to 60 °C while magnetically stirred to evaporate the solvent. Finally, the paste was rolled to form a homogenous film. The thickness, weight loading and packing density of MnO₂ films were ~ 100 μm, ~ 12.5 mg cm⁻², and ~ 1.28 g cm⁻³, respectively. The films were punched into a circular disk shape of 3 mm in diameter and used as working electrodes. The weight of these electrodes was determined using PerkinElmer AD-6 microbalance.

5.2.3. Synthesis and characterization of 2-D Titanium Carbide MXene

5.2.3.1. Synthesis

2-D Ti₃C₂ MXene was synthesized by minimally intensive layer delamination method (MILD) (Alhabeab *et al.*, 2017). Briefly, 1 g of MAX phase powder of Titanium Aluminum Carbide MAX was added slowly to a mixture of 1 g of lithium fluoride in 20 ml of 9 M hydrochloric acid to chemically etch the aluminum from MAX phase. The reaction was stirred with a Teflon-bar for 24 h at 35 °C. The products were transferred to a 50 mL centrifugation tube and washed with deionized water by centrifugation at 3500 rpm (5 min per cycle) until the pH of the dark-green supernatant was > 5.5. The change in color indicates the beginning of delamination. After gathering the supernatant, settled and swollen sediment at the bottom of the centrifuge tube was collected and dispersed in deionized water (by shaking). Resulting black slurry was vacuum-filtered on a Celgard membrane 3501 (Celgard®) to form free-standing films which were dried in a vacuum oven at 120 °C overnight and then stored in a vacuum desiccator for further use. The films were punched into a circular disk shape of 3 mm in diameter and used as working electrodes. The thickness, weight loading

and packing density of Ti_3C_2 films were $\sim 8 \mu\text{m}$, $\sim 2.2 \text{ mg cm}^{-2}$, and $\sim 2.75 \text{ g cm}^{-3}$, respectively. 4.2.3.2. Material Characterization

The XRD pattern of Ti_3AlC_2 grains and Ti_3C_2 film were shown by **figure. 5.4 a-b**. Whereas, the SEM image of the Ti_3C_2 film is shown by **figure. 5.5 b**. The shift of the (002) peak from 9.48° to 7.16° in XRD patterns specifies the etching of Ti_3AlC_2 MAX. Besides, disappearing of MAX peaks (noticeably, (104)) to the benefit of (00l) peak demonstrates efficient leaching of Al from the Ti_3AlC_2 MAX precursor, leading to its conversion into $\text{Ti}_3\text{C}_2\text{T}_x$ MXene. Also, shifting of (002) peak in Ti_3C_2 XRD pattern, as well as the presence of high order diffraction peak (0010), agrees with the restacked film structure observed in SEM images and with the previous reports (Alhabebe *et al.*, 2017), suggesting the removal of Al from Ti_3AlC_2 MAX (Alhabebe *et al.*, 2017).

5.3. Selection of the electrolyte concentration

The selection criteria for the appropriate water-in-salt concentration was based on the analogous electrochemical potential window. To observe this

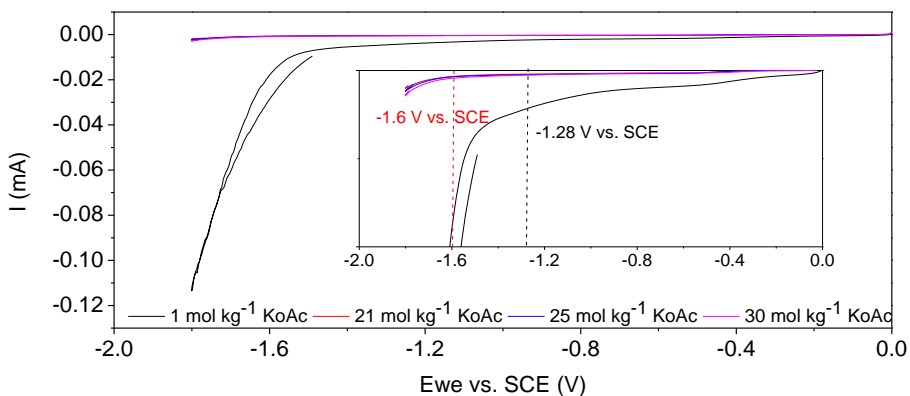


Figure 5. 5. CV curves of electrolyte solutions on a glassy carbon electrode. The scan rate for the analysis was about 2 mV s^{-1} .

criterion, the cyclic voltammetry technique at a scan rate of 2 mVs^{-1} was used to measure the electrochemical potential windows. This analysis was carried out in a three-electrode cell configuration. The CV curves are depicted in **figure 5.5**. For 1 m of potassium acetate electrolyte solution, the on-set potential for HER occurs at -1.28 V vs. SCE . This on-set potential

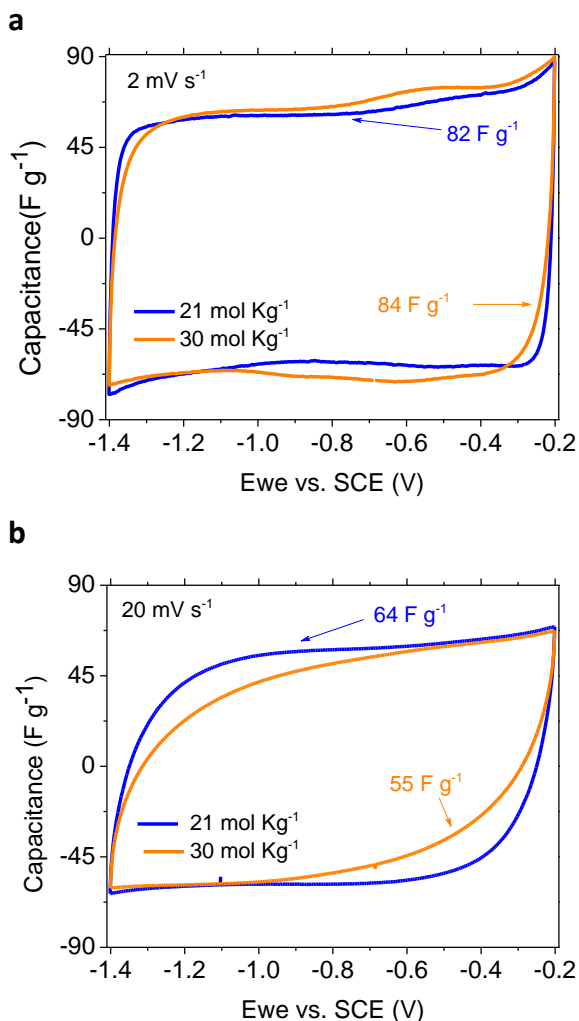


Figure 5. 6. Cyclic voltammogram of Ti_3C_2 MXene films in a 21 and 30 m of potassium acetate solution at a (a) low (2 mVs^{-1}) and (b) moderate scan rate (20 mVs^{-1}).

shifts by 320 mV when the electrolyte concentrations were increased to 30 m (-1.6 V vs. SCE), these observations are in agreement with the results recently reported by (Daniel P. Leonard *et al.*, 2018) with potassium acetate water-in-salt electrolytes for potassium ion batteries. Interesting, by decreasing the salt concentration from 30 to 21 m, similar onset potentials of ~ -1.6 V vs. SCE for HER were seen. As, these results reflect a similar behavior of the HER potentials within the molality of 30 and 21, these two extreme concentrations of the electrolyte were considered for further analysis. These two electrolyte concentrations were applied to observe the electrochemical charge storage properties in 2-D Ti_3C_2 MXene electrode film. 2-D Ti_3C_2 MXene was selected as it exhibits high electrical conductivities and volumetric capacitance. Besides this, the 2Θ peak at 7.16° in XRD pattern specifies a d-spacing of 12.38 \AA . Considering the minimal to maximal solvation of potassium ions, the ionic radii of a $\text{K}(\text{H}_2\text{O})_{7-x}^+$ ion (potassium ion surrounded by water ligands) varies from 1.37 \AA (K^+ ion without solvation shell (Haynes, Lide and Bruno, 2018)) to 2.80 \AA (solvated $\text{K}(\text{H}_2\text{O})_7$ ion (Tian *et al.*, 2017)). The d-spacing of 12.38 \AA is relatively a large interlayer space to facilitate the intercalation of large K^+ ions within its interlayer, as also highlighted by (Levi *et al.*, 2015).

Electrochemical properties of 2-D Ti_3C_2 Mxene films were examined in a three-electrode cell configuration. The CV at a scan rate of 2 mV s^{-1} is shown in **figure 5. 6a**. This CV profile is attributed to the intercalation of solvated K^+ ions within the interlayers spacing of Ti_3C_2 , as previously shown by (Levi *et al.*, 2015). The calculated capacitance for this CV profile is about 83.5 F g^{-1} . Interestingly, increasing the scan rate to a value of 20 mV s^{-1} evolves the CV profile from a rectangular to quasi-rectangular-like behavior. The degradation of the rectangular CV into a quasi-rectangular loop implies a

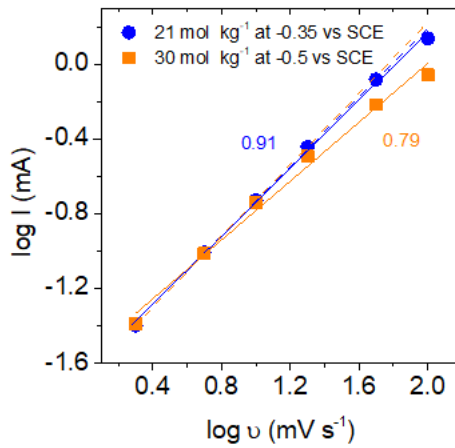


Figure 5. 7. Log plot of observed current verses. Scanning rate of the cyclic voltammogram. Linear Square Fitting of the plot depicts the kinetic behavior of the electrolytes ions in Ti_3C_2 MXene films. Dashed lines represents a capacitance independence over rate with a reversible behavior.

diffusion limitation of $K(H_2O)_{1.8}^+$ ions within the Ti_3C_2 MXene interlayers (for 30 m, K^+ has about 1.8 water ligands (Tian *et al.*, 2017)). Whereas, for 21 m, at the scan rate of 2 mV s^{-1} , the CV indicates a rectangular-like behavior (**figure 5. 6a**), a trend similar to that of 30 m. The calculated capacitance from this profile corresponds to a capacitance of 81.8 F g^{-1} (2 mV s^{-1}), which is in fact close to the value obtained in 30 m (83.5 F g^{-1}). Increasing the scan rate to a value of 20 mV s^{-1} , shows a less quasi-rectangular shape than the observed CV curve of 30 m. In the case of 20 mV s^{-1} , the capacitance attributes to a value of 63.46 F g^{-1} , which was higher than the capacitance of 30 m (54.98 F g^{-1}). These values in terms of capacity translate to 21.5 and 18.33 mAh g^{-1} , respectively. Considering the surface termination of Ti_3C_2 with -OH group and with a possible stoichiometry of $Ti_3C_2(OH)_2$, as mentioned by (Xie *et al.*, 2014; Levi *et al.*, 2015), the values in capacity translates to a K^+ insertion level of $\sim x$ or $Ti_3C_2O_2K_x$, where $x = 1$ corresponds to $\sim 140 \text{ mAh g}^{-1}$ (Levi *et al.*, 2015). Taking this into consideration, in the case of 21 m, the adsorption of K^+ ions was reached to ~ 0.16 or to a chemical

formula of $\text{Ti}_3\text{C}_2\text{O}_2\text{K}_{0.16}$. Whereas, an insertion value of ~ 0.13 or chemical formulae of $\text{Ti}_3\text{C}_2\text{O}_2\text{K}_{0.13}$ was achieved in 30 m. This electrochemical analysis indicates low adsorption of K^+ ions in 30 m when compared to that of 21 m. So, this way the use of 21 m seems stills reasonable and was selected as electrolyte concentration for further electrochemical evaluations. **Hypothesis:** *The low electrochemical charge storage in Ti_3C_2 MXene for 30 m of potassium acetate water-in-salt electrolyte could be related to the insertion hindrance of K^+ ion within the interlayers of Ti_3C_2 MXene electrodes.*

To validate this hypothesis, kinetic insertion analysis was carried out by plotting *Log* scheme of current observed during the scan rate. The plot is shown in **Figure 5. 7. Least Squares Fitting** for 21 m of potassium acetate water-in-salt electrolyte in this plot indicates a linear dependence with a slope close to a value of 0.91. Whereas, for 30 m, this slope decreases to 0.79. Though, the slope in both electrolytes is higher than 0.5, which is attributed to a diffusion limitation. The slope of 21 m being closer to 1, represents capacitance independence over rate with a reversible behavior, such behavior was as previously discussed by (Levi *et al.*, 2015) in non-water-in-salt based aqueous electrolytes. Previously, (Daniel P Leonard *et al.*, 2018) showed that the ionic conductivity of 30 m is lower than over 21 m of potassium acetate electrolyte. Therefore, the slow kinetic insertion effect in 30 m can be attributed to the low ionic conductivity of 30 m over 21 m.

Limitations: Although a high insertion value for K^+ ions were reached in 21 m of potassium acetate electrolytes, the trend of quasi-rectangular-like behavior is still seen in the CV curve, which is in contradiction with the previous electrochemical observations of Ti_3C_2 films in traditional aqueous or salt-in-water electrolytes, as reported by several authors like (Lukatskaya *et al.*, 2013; Levi *et al.*, 2015). In salt-in-water electrolytes (Lukatskaya *et al.*,

2013; Levi *et al.*, 2015) reported having CV profiles to be rectangular even at scan rates higher than 20 mV s^{-1} . In such cases, the high ionic conductivity of classical aqueous electrolytes ($50 - 250 \text{ mS cm}^{-1}$ (Gambou-Bosca and Bélanger, 2016)) is responsible for rapid insertion of electrolyte cations in the interlayers spacing of Ti_3C_2 , which makes the CV curves to be rectangular. Although, this discussion indicates a favorable direction of electrochemical investigation using classical aqueous electrolytes. Yet, the benefit of having extended electrochemical potential windows in water-in-salt (nearly 1.2 V , this work see **Figure 5.6**) over classical aqueous electrolytes ($< 0.8 \text{ V}$, (Lukatskaya *et al.*, 2013)) still appears to be promising. Therefore, further electrochemical investigation in regard to the selection of MnO_2 tunnel phase was taken into consideration using water-in-salt electrolytes (21 m).

5.4. Electrochemical properties of tunnel polymorphs of Manganese Oxide in potassium acetate base water-in-salt electrolyte

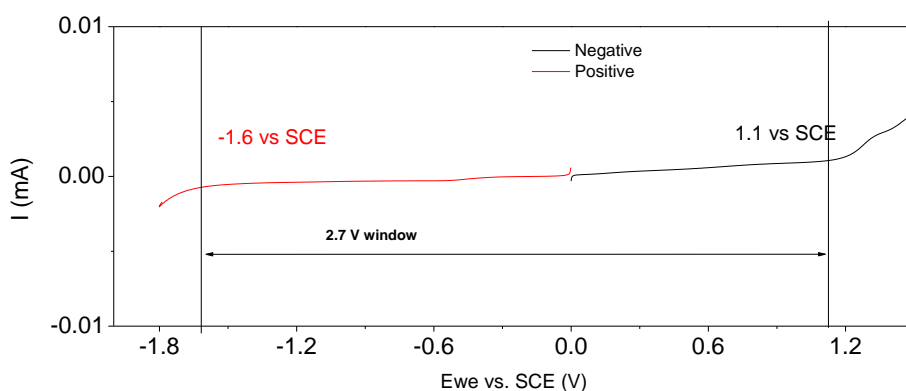


Figure 5. 8. CV curve of 21 m of potassium acetate electrolyte on a glassy carbon electrode. The scan rate used during the analysis was 2 mVs^{-1} .

Understanding the co-relation between tunnel size and storage of charge was carried out by performing CVs in a three-electrode cell configuration. As, the molality of 21 m potassium acetate showed the best compromise between high charges storing and insertion kinetics for the negative electrode (Ti_3C_2 , see the previous section), it was selected as electrolyte concentration for analyzing the electrochemical properties of the MnO_2 -based positive electrode. A background study was done to know the positive potential limits of the MnO_2 -based electrode SPW for a 21 m potassium acetate electrolyte. CV curves indicate an occurrence of oxygen evolution reaction from 1.1 vs SCE (**figure 5.8**). Considering this, the MnO_2 electrodes were evaluated within a maximum vertex potential of 1.1 vs SCE.

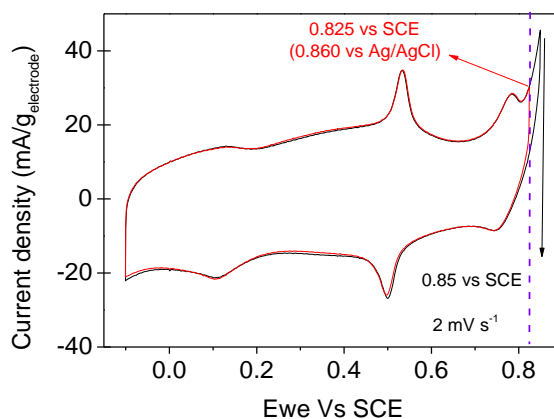


Figure 5. 9. CV curves of $\beta\text{-MnO}_2$ at a scan rate of 2 mVs^{-1} , black color indicates extended window where oxidative tails occurs

5.4.1. Influence of tunnel widening and its charge storage behavior

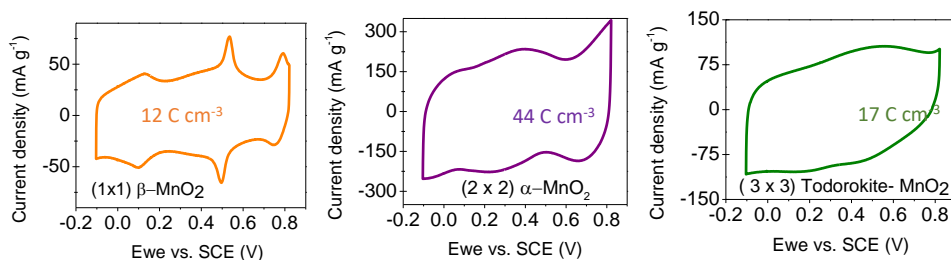


Figure 5. 10. Cyclic voltammogram of (left) β - MnO_2 ($1 \times 1 MnO_2$), (middle) α - MnO_2 ($2 \times 2 MnO_2$) and (right) Todorokite - MnO_2 ($3 \times 3 MnO_2$). All electrochemical measurements were conducted in 21 m potassium acetate electrolyte at a scanning rate of $5 mV s^{-1}$.

Initially, the smallest tunnel size of MnO_2 (1×1 , β - MnO_2) was selected to understand the electrochemical response. The CV curve in a three-electrode configuration is shown in **figure 5.9**. The curve indicates that beyond 0.825 V vs SCE irreversible oxidative tail occurs. Therefore, the SPW for all MnO_2 electrodes were considered within -0.1 to 0.825 V vs SCE. The CV of β - MnO_2 is performed with a scan rate of $5 mV s^{-1}$ and the results are depicted by **figure 5.10 (left)**. The CV profile is composed of two distinct redox peaks, which corresponds to a total volumetric charge of $11.99 C cm^{-3}$. It is noteworthy that MnO_2 CV profiles are a combination of double layer and redox reactions. Therefore, the calculation of capacitance or capacity was not considered. Also, to avoid confusion and overestimations of values (Brousse, Bélanger and Long, 2015), only the charge was calculated in the current discussion. Expanding the tunnel size from β - MnO_2 (1×1) to an α - MnO_2 (2×2), via stabilization of the tunnels using K^+ ions, results in a significant modification of the CV profile from sharp and narrow redox peaks to broad and less reversible redox reactions (**Figure 5.10 (middle)**).

Besides, broad redox peak at higher positive potential was also seen. However, a total charge of 44.22 C cm^{-3} was achieved by increasing the tunnel size to an $\alpha\text{-MnO}_2$ (2×2) structure, a value almost 4 times higher than that of $\beta\text{-MnO}_2$ (11.99 C cm^{-3}). Further increase of tunnel size to Todorokite - MnO_2 (via Mg^{2+} stabilization, $3 \times 3 \text{ MnO}_2$), shows an even more rectangular like CV profile (**Figure 5.10, right**), which collaborates to a charge of 16.74 C cm^{-3} . This charge was lower than the value of $\alpha\text{-MnO}_2$ (44.22 C cm^{-3}). The occurrence of the above-mentioned trend can be supported by the interaction of electrolyte ions with the crystallographic structure of MnO_2 .

Proposed mechanism of charge storage values in MnO_2 in potassium acetate water-in-salt electrolyte: Previously according to (Young *et al.*, 2015), the origin of the charge storage mechanism in tunnel structures of MnO_2 was suggested to be either one or a combination of both (i) insertion of cations and proton in tunnels (interstitial sites) and (ii) redox reactions (charge-switching states). In case of $\beta\text{-MnO}_2$ (1×1 tunnels), the maximal ion radii to be able to access the tunnel structure is 0.40 \AA (based on the distance between oxygen-oxygen atoms in 1×1 tunnel site of $\beta\text{-MnO}_2$ (Young *et al.*, 2015)). Considering the minimal to maximal solvation, the ionic radii of a $\text{K}(\text{H}_2\text{O})_{7-x}^+$ ion (potassium ion surrounded by water ligands) varies from 1.37 \AA (K^+ ion without solvation shell (Haynes, Lide and Bruno, 2018)) to 2.80 \AA (solvated $\text{K}(\text{H}_2\text{O})_7^+$ ion (Tian *et al.*, 2017)). Since the size of the $\text{K}(\text{H}_2\text{O})_{7-x}^+$ ion is larger than the size of the 1×1 tunnel of $\beta\text{-MnO}_2$ (0.40 \AA), the charge storage mechanism in $\beta\text{-MnO}_2$ is only limited to proton insertion. Besides, according to (Young *et al.*, 2015) the protons in the 1×1 tunnel sites reduces to form hydroxyl groups giving the redox reactions profile in the CV curve, which can be also seen through the CV curves of $\beta\text{-}$

MnO₂ of this work. The highest charge storage in α -MnO₂ over β -MnO₂ in our results is originated because of the dual charge storage coming from the intercalation of protons and potassium ions in the tunnels sites (Young *et al.*, 2015). Besides this, the presence of broad redox peak in α -MnO₂ attributes to a change in the oxidation state of Mn (from 3⁺ to 4⁺ (Ghodbane, Pascal and Favier, 2009; Young *et al.*, 2015)), which has risen due to cation induced charge switching states (Young *et al.*, 2015). Besides,

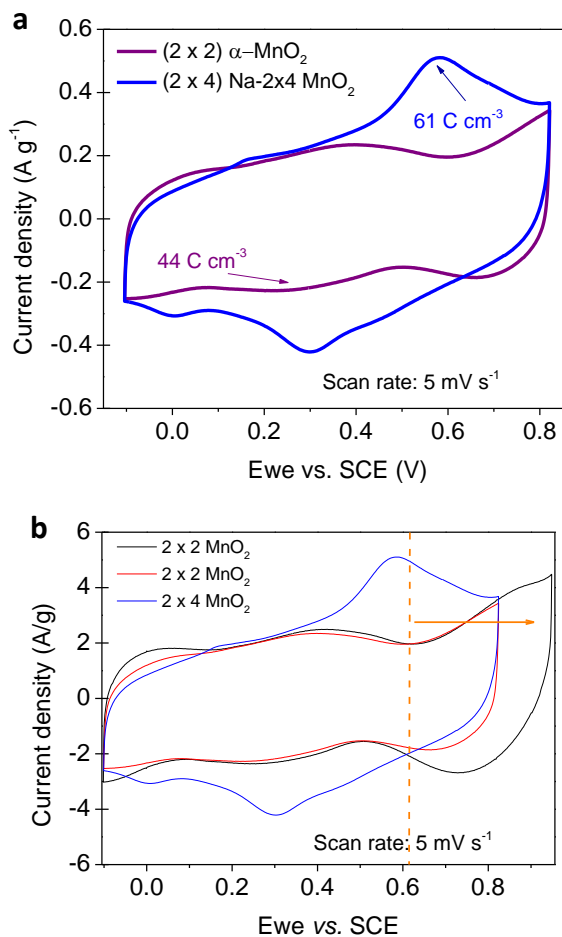


Figure 5. 11. (a) Cyclic voltammogram of α -MnO₂ and Na-2x4 MnO₂ electrodes in 21 m of potassium acetate solution at low rates (5 mV s⁻¹). (b) Cyclic voltammogram indicating a redox peak with the extension of potential window for α -MnO₂.

substantially lower value of charge response in Todorokite-MnO₂ over α -MnO₂ is due to the hindrance of electrolyte ions for insertion in the tunnel sites (interstitial insertion). Such hindrance, according to (Ghodbane, Pascal and Favier, 2009; Byles *et al.*, 2018), is caused by the strong hydrogen bonding between oxygen of Mn site with the oxygen atoms in the hydration shell of magnesium ion (Ghodbane, Pascal and Favier, 2009; Byles *et al.*, 2018).

At this stage of the investigation, the above-mentioned discussions indicate that in order to achieve enhanced charge storage, an increase of tunnel size is required, in which tunnel stabilization should be achieved with the moderate size of cations, which was found to be for α -MnO₂ (2 x 2 MnO₂).

4.3.2. Influence of tunnel widening and its charge storage behavior

Considering these new insights of using α -MnO₂, another phase of MnO₂ is used where the tunnel width has four MnO₆ octahedra (*See Appendix B.1*). The agenda behind using this tunnel phase was to increase the charge storage value in MnO₂ tunnel phase. To achieve such tunnel sizes, Na⁺ ions are used as stabilizing cations to form a chemical formula of Na_{0.21}MnO_{2- δ} (*See EDS, Appendix B figure 1*). The SEM images of Na-2x4 MnO₂ showed the morphology of nanowires (*Appendix B, figure 2*), an observation similar to that of α -MnO₂ and Todorokite-MnO₂ (*See section 5.3.2*). The 2 Θ peak at $\sim 6.8^\circ$ and $\sim 12.3^\circ$ in the XRD pattern indicates the presence of two and four octahedra structures, respectively (*Appendix B, figure 3*). Such a result indicates a 2 x 4 tunnel with a dimension of 4.6 by 9.2 Å. The CV performed on Na-2x4 MnO₂ electrode in three-electrode cell configuration is shown by *figure 5.11 a*, which indicates a capacitive envelope, along with a distant oxidative peak at ~ 0.57 V vs SCE. This charge profile accounts for

60.86 C cm⁻³, a value higher than that of α -MnO₂ (44.22 C cm⁻³, **figure 5.11 a**). This increase of charge is attributed to the redox peak (blue curve, **figure 5.11 a**). This redox peak might be attributed to a change in the oxidation state of Mn with the intercalation of cations (Ghodbane, Pascal and Favier, 2009; Young *et al.*, 2015). Besides, the presence of such redox a peak in α -MnO₂ (Ghodbane, Pascal and Favier, 2009), can be clearly seen with the extension of potential towards the positive window (-0.95 V vs SCE, **figure 5.11 b**). Such shifts have also been previously reported by (Ghodbane, Pascal and Favier, 2009). A shift in the potential of this redox peak indicates an alteration of charging switching states, which can be correlated with the *Average Oxidation State (AOS)* of Mn in MnO₂. The AOS of Mn in α -MnO₂ and Na-2x4 MnO₂ was determined by Iodometric titration (*see chapter 2 for methods*) and the results were shown in **table 5.2**. Unlike X-ray photoelectron spectroscopy technique, where only the surface of the electrode material is probed, the AOS value provided by Iodometric titrations depicts the bulk value of the materials. Such bulk AOS can be directly correlated with the electrochemical measurements, as the electrode is considered to be a bulk material. As shown in **table 5.2**, the AOS of Mn in α -MnO₂ (3.79) is higher than for Mn in a Na-2x4 MnO₂ (3.72). This higher AOS value in α -MnO₂ indicates the alteration of charge switching states (change in the oxidation state of Mn) which can be correlated to the results in a shift of redox potential in CV, as shown in **figure 5.11**.

Tunnel structure of MnO ₂	A.O.S
α -MnO ₂	3.79
Na-2x4 MnO ₂	3.72

Table 5. 2. Average oxidation state (AOS) of Manganese from Iodometric titrations

Proposed Mechanism: The difference of the high AOS value and the shift of peaks in the CV curve can be hypothesized with the influence of the stabilizing cations in the interstitial tunnel structures of the tunnel MnO_2 phase. Since, $\text{Na-}2\times 4 \text{ MnO}_2$ and $\alpha\text{-MnO}_2$ are stabilized with different cations, K^+ and Na^+ , respectively. The ionic radii of these cations can alter the Mn [3d] orbitals (primary d-p π^* anti-bonding orbitals of Mn-O (Young *et al.*, 2015)) with a different amplitude, depending on the atomic radii. Here, the ionic radii of K^+ (~ 1.37 (Haynes, Lide and Bruno, 2018)) is ~ 1.4 times larger than Na^+ ion (0.99 \AA (Haynes, Lide and Bruno, 2018)). According to (Young *et al.*, 2015), the interstitial K^+ ions causes a larger shift of Mn [3d] orbitals from the conduction band, which results in a larger shift in charge-switching state towards higher electrochemical potential. Considering this, the shift of redox potential in the CV (as shown by **Figure 5.11**), can be hypothesized to the alteration in charge-switching states (change in the oxidation state of Mn) caused by the stabilizing cations in the interstitial tunnel sites.

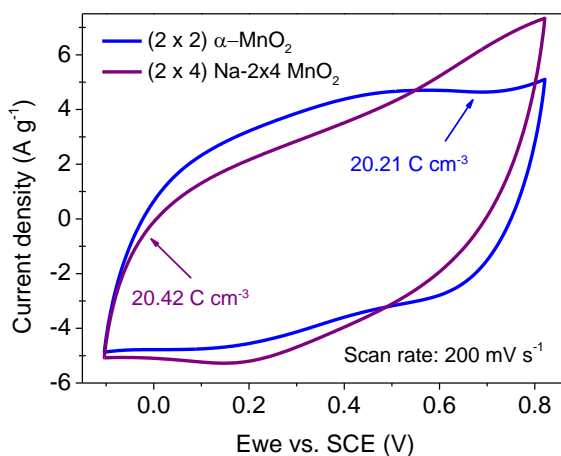


Figure 5. 12. Cyclic voltammogram of $\alpha\text{-MnO}_2$ and $\text{Na-}2\times 4 \text{ MnO}_2$ electrodes in 21 m of potassium acetate solution at high rates (200 mV s^{-1}).

Limitations of using Na-2x4 MnO₂ tunnel structure for the Ti₃C₂(-)//MnO₂(+) cell: Since, Na-2x4 MnO₂ can store higher charge than α -MnO₂ (60.86 vs. 44.22 C cm⁻³), it could be selected as a promising candidate for the positive electrode in the asymmetric cell of Ti₃C₂(-)//MnO₂(+). Yet, the capacitance over scan rate (implying the rate behavior), challenges the Na-2x4 MnO₂ for this spot. The rate decay of Na-2x4 MnO₂ was $\sim 33\%$ at 200 mV s⁻¹ ($C_{5\text{ mV s}^{-1}}/C_{200\text{ mV s}^{-1}}$, **figure 5. 12**). Under the same potential window (between -0.1 to 0.825 V vs. SCE), this rate decay of Na-2x4 MnO₂ was higher compared to that of α -MnO₂ ($\sim 45.27\%$). This trend is accounted for the kinetic shift of redox peaks with the increase in scan rate (**figure 5.7**). The lower rate decay of α -MnO₂ over Na-2x4 MnO₂, can be explained by the highest electronic conductivity of α -MnO₂ (9×10^{-3} S.cm⁻¹), almost ~ 24 times higher than that of Na-2x4 MnO₂ (3.8×10^{-4} S.cm⁻¹)(Ghodbane, Pascal

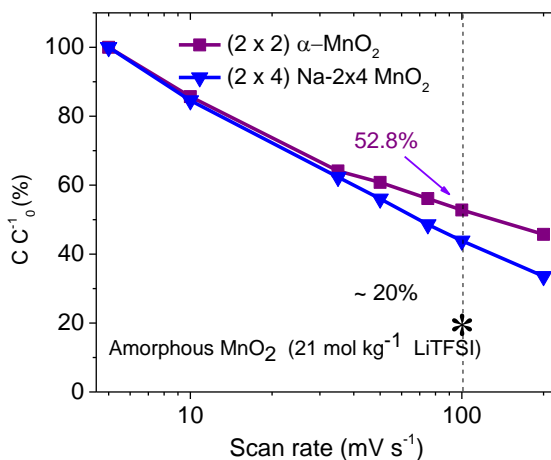


Figure 5. 13. Comparison of the rate decay behavior between Na-2x4 MnO₂ and α -MnO₂. Rate decay value, at 100 mV s⁻¹, of amorphous MnO₂ in 21 m of Li-TFSI from the literature was also compared and represented by an asterisk (*). **Composition-** MnO₂:binder:conductive additive – 60:10:30, active material loading 2.9 mg cm⁻³ (Gambou-Bosca and Bélanger, 2016). The thickness, mass loading and packing density of the MnO₂ electrodes was ~ 100 μ m, ~ 11 mg cm⁻² and ~ 1.3 g cm⁻³, respectively. **Composition-** MnO₂: binder: conductive additive – 75:5:20.

and Favier, 2009) which is responsible for the enhanced redox kinetics of α - MnO_2 . For comparison with existing reports, the rate decay $\sim 53\%$ in α - MnO_2 with 21 m potassium acetate was lower than the amorphous MnO_2 in 21 m of Li-TFSI based water-in-salt electrolyte (Gambou-Bosca and Bélanger, 2016) ($\sim 20\%$, $C_{5\text{ mV s}^{-1}}/C_{100\text{ mV s}^{-1}}$, where C=charge or capacitance, **Figure 5.13**). As a whole, this discussion also implies that the electrochemical potential window of MnO_2 must be chosen in which redox reactions are either absent or a higher electronically conductive phase of MnO_2 should be nominated, in order to have enhanced kinetics of redox pair in the SPW. Considering this understanding, thanks to the low rate decay of α - MnO_2 over Na-2x4 MnO_2 and its reasonable charge at low rates, α - MnO_2 was selected as a positive electrode in the asymmetric cell of $\text{Ti}_3\text{C}_2(-)//\text{MnO}_2(+)$. The assembly and the electrochemical behavior of this asymmetric cell are discussed in the following section.

5.5. Asymmetric cell of 2-D Titanium carbide MXene and Manganese Oxide in potassium acetate based water-in-salt electrolyte

Based on the previously accumulated knowledge and selection of water-in-salt potassium acetate molality (21 m) as well as the electrodes material (*see previous sections*), an asymmetric cell was proposed to be assembled. The configuration of this cell includes Ti_3C_2 MXene and α - MnO_2 ($2 \times 2 \text{ MnO}_2$) as a negative and positive electrode material, respectively. The electrochemical properties of this asymmetric cell in terms of stability and self-discharges are discussed in the following sections and valid reasoning is providing about the favorable use of this asymmetric cell configuration

($\text{Ti}_3\text{C}_2//\text{MnO}_2$) in the applications where a volume of the electrochemical energy storage device is critical.

5.5.1. Assembly of asymmetric cell

The CV curves, as shown in **figure 5.14**, specify that the vertex negative potential for Ti_3C_2 MXene can be close to -1.6 V vs. SCE. Whereas, $\alpha\text{-MnO}_2$ can perform up to 0.95 V vs. SCE. The SPW of both electrodes gives a possibility to operate the cell with a voltage of 2.55 V. In order to sanction or regulate this voltage as the nominal cell voltage, Voltage-Hold test at

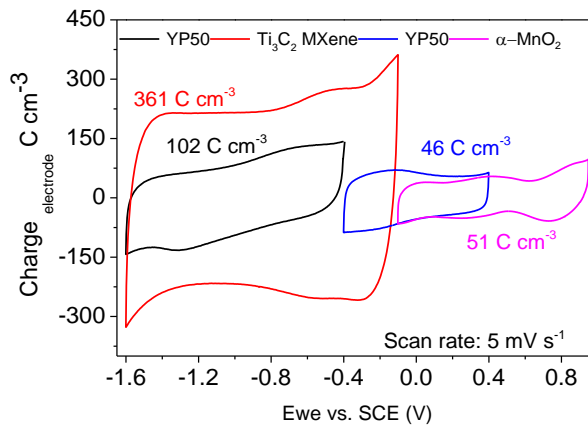


Figure 5. 14. Cyclic voltammogram of Ti_3C_2 MXene films, YP-50 and $\alpha\text{-MnO}_2$ (2×2 MnO_2) in a three electrode cell configuration. All electrochemical measurements were carried in the 21 m potassium acetate electrolyte solution.

several cell voltages are conducted and corresponding leakage currents are taken in account. According to (Goubard-Bretesché *et al.*, 2016; Laheäär, Arenillas and Béguin, 2018; Lannelongue *et al.*, 2018), during the Voltage-Hold test, the observance of unstable leakage current will specify the breakdown of the cell, whereas stable current will indicate the safe operating voltage of the cell. Besides this, previously several authors like (Demarconnay, Raymundo-Piñero and Béguin, 2011; Goubard-Bretesché *et al.*, 2016), reported to carry out mass balancing approach with carbon-based

EDLCs when there is an occurrence of the uneven value of charge storage between the positive and negative electrode. This can be given by:

$$R = \left(\frac{m_+}{m_-}\right) = \left(\frac{C_- \Delta V_-}{C_+ \Delta V_+}\right), \quad (4.1)$$

where m_+ and m_- represent the mass, C_+ and C_- the capacitance, and ΔV_+ and ΔV_- the potential window of the positive and negative electrode, respectively. Since, the Ti_3C_2 MXene shows higher values of charges (361 C cm^{-3}) than $\alpha\text{-MnO}_2$ (51 C cm^{-3} , as shown in **Figure 5.14**). The mass balancing approach is conceded to equilibrate the charge storage between Ti_3C_2 MXene and $\alpha\text{-MnO}_2$, before performing the Voltage-Hold tests. The R -value in Eq. (4.1) between $\alpha\text{-MnO}_2$ and Ti_3C_2 was ~ 3.6 . After the mass balancing approach, both electrodes are polarized with a similar OCV, which was close to -0.2 vs. SCE . Voltage-Hold tests of $\text{Ti}_3\text{C}_2//\text{MnO}_2$ cell are measured from 1.5 to 2.5 V and the corresponding leakage current is shown in **figure 5.15**. This figure demonstrates a stable leakage current within 2.2 V , implying safer operational voltage limits for the cell (as indicated by green shade in the figure). Whereas, beyond 2.2 V , the leakage current is unstable, which indicates the breakdown of the cell (as indicated with orange and red shades). To understand this failure, the potential windows of the individual electrodes are observed before and after the Voltage-Hold test at 2.5 V . The result, in terms of the CV curve is shown in **figure 5.16 a-c**. This curve shows that with an increase of cell voltage, the potential window of $\alpha\text{-MnO}_2$ widens, notably in the negative windows. Such an increase in the electrochemical windows, especially below -0.3 vs SCE , leads to the formation of Mn^{2+} species (Young *et al.*, 2015), which are dissolvable with the electrolyte, causing the breakdown of the $\text{Ti}_3\text{C}_2//\text{MnO}_2$ cell.

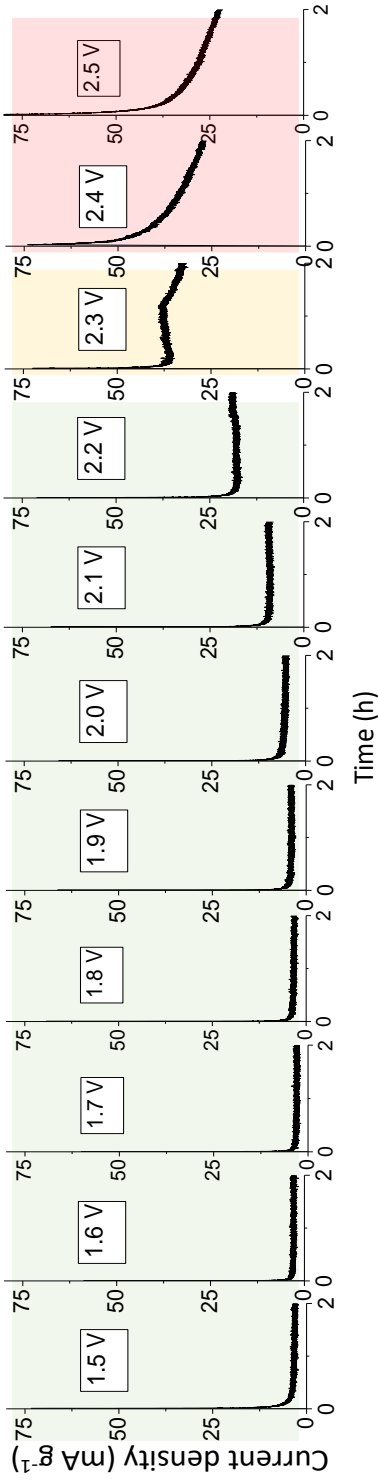


Figure 5.15. Voltage-hold tests in an asymmetric cell, $\text{Ti}_3\text{C}_2 // \alpha\text{-MnO}_2$. Voltage-Hold tests indicate an unstable leakage current at 2.2 V. Beyond that, leakage current start to decrease, which implies the breakdown of cell.

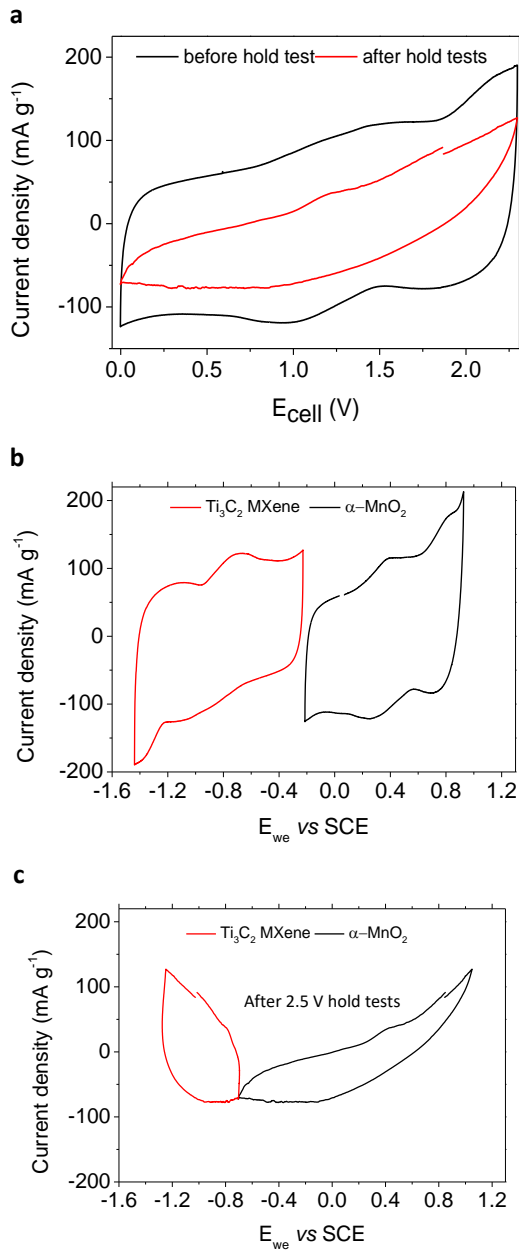


Figure 5. 16. Cyclic voltammogram of (a) Ti_3C_2 vs $\alpha\text{-MnO}_2$ cell before and after hold tests (b) potential windows of individual electrodes before hold test (c) potential windows of individual electrodes after hold tests at 2.5 V. Extension of the cell voltage widens the MnO_2 electrochemical potential window.

Since the voltage hold tests recognize 2.2 V as a safe operational cell voltage, CVs are performed within the nominal voltage of 2.2 V for $\text{Ti}_3\text{C}_2//\text{MnO}_2$ cell. This way, the electrochemical properties can be observed and can be later compared to a traditional YP-50 activated carbon-based supercapacitor.

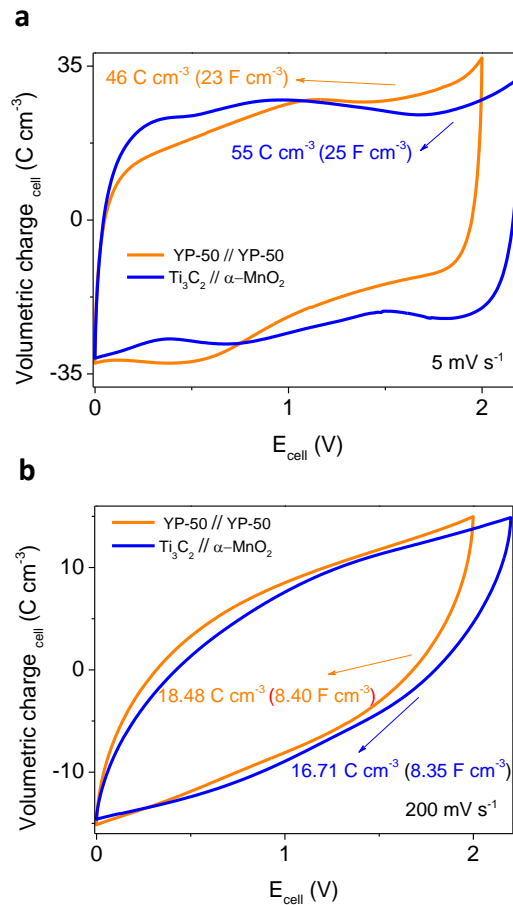


Figure 5. 17. Cyclic voltammogram of the activated carbon based supercapacitor cell (YP-50//YP-50) and asymmetric cell of $\text{Ti}_3\text{C}_2//\alpha\text{-MnO}_2$ (a) at low rate (5 mV s^{-1}) and (b) high rate (200 mV s^{-1}). All electrochemical measurements were carried in the 21 m potassium acetate electrolyte solution.

From the previously reported values (Tian *et al.*, 2017), 2.0 V was taken as a safe operational window for this activated carbon cell (YP-50 // YP-50 cell). The CV curves for $\text{Ti}_3\text{C}_2//\alpha\text{-MnO}_2$ cell, as shown by **figure 5.17 a**, indicates a rectangular-like current response, demonstrating a capacitance-like profile. This response corresponds to a capacitance value of 24.9 F cm^{-3} or charge of $\sim 54.8 \text{ C cm}^{-3}$. This value is similar to that of YP50 // YP50 cell, where the capacitance and charge are $\sim 23.0 \text{ F cm}^{-3}$ or $\sim 46 \text{ C cm}^{-3}$, respectively. CV curves at a high rate, such as 200 mVs^{-1} , as shown by **figure 5.17 b**, shows a volumetric capacitance of $\sim 8.4 \text{ F cm}^{-3}$ for both YP-50 // YP-50 cell and as well as for the $\text{Ti}_3\text{C}_2//\text{MnO}_2$ cell. This value of capacitance is similar for both cells, indicating they behave similarly at high rates.

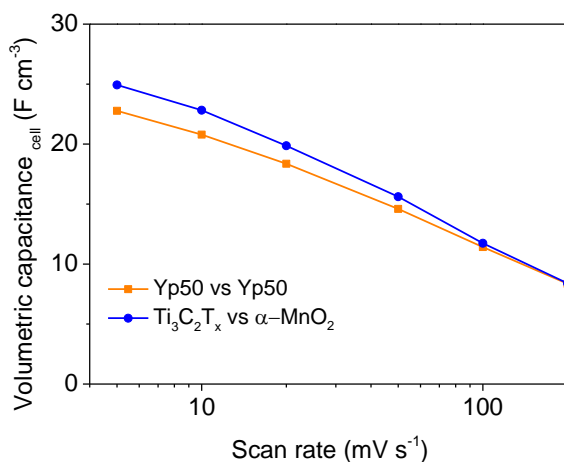


Figure 5.18. Capacitance over scanning rate performance of the EDLC (YP50 // YP50) and pseudocapacitor ($\text{Ti}_3\text{C}_2 // \alpha\text{-MnO}_2$). All electrochemical measurements were carried in the 21 m potassium acetate electrolyte solution.

To understand the rate decay, the relationship between charge and scan rate is plotted which is shown in **figure 5.18**. Analysis of the rate decay indicates a similar decay value of $\sim 30 \%$ for both, cells. Comparing these values with the literature, rate decay of the $\text{Ti}_3\text{C}_2//\text{MnO}_2$ cell was $\sim 48 \%$ for

$C_{5\text{ mV s}^{-1}}/C_{100\text{ mV s}^{-1}}$, which is significantly lower than the previously reported Carbon-MnO₂ cell in 21 m Li-TFSI water-in-salt electrolyte (~ 17.6 %)(Gambou-Bosca and Bélanger, 2016).

Hypothesis: *The resulting low rate-decay in Ti₃C₂//MnO₂ cell compared to existing Carbon-MnO₂ cell in 21 m Li-TFSI water-in-salt electrolyte could be endorsed to the synergic effect of using conductive 2-D Ti₃C₂ Mxene and appropriate concentration of water-in-salt electrolyte (allowing higher charge storage kinetics) as well as the moderate tunnel size and electronically conducting phase of MnO₂.*

5.5.2. Self-discharge analysis

Self-discharge is a crucial property in supercapacitors. The self-discharge is the decay of open circuit voltage over the time interval after the charging of the cell. In classical aqueous electrolytes based ELDCs, such self-discharges are quick and happens in a span of few minutes. Origin of this behavior is credited to the quick re-distribution of charges at the interface of electrode and electrolyte, which is also called as the Fluid-solid interface, FSI (Forse *et al.*, 2016). To the best of my knowledge, the narrative of such properties in water-in-salt electrolytes for electrochemical supercapacitors has not been reported so far (Gambou-Bosca and Bélanger, 2016; Tian *et al.*, 2017; Dou *et al.*, 2018; Lannelongue *et al.*, 2018), which also makes it significant to discuss here. Self-discharges of YP-50//YP-50 and Ti₃C₂//MnO₂ cell is shown in **figure 5.19 a**. The use of water-in-salt electrolyte with carbon electrodes slows down the self-discharge of in YP-50 // YP-50 cell (> few mins), which seems related to limited diffusion of charges at the FSI. Such hindrance of re-distribution or to a diffusion limitation is categorized by non-linear decay of voltage with a function in $t^{-1/2}$ (Laheäär, Arenillas and Béguin, 2018). The non-linear decay of voltage to $t^{-1/2}$ in YP-50 // YP-50 cell,

as shown by **Figure 5.19 b**, approves an ion-diffusion limitation. Origin of such diffusion occurs due to the higher viscosity of water-in-salt electrolyte

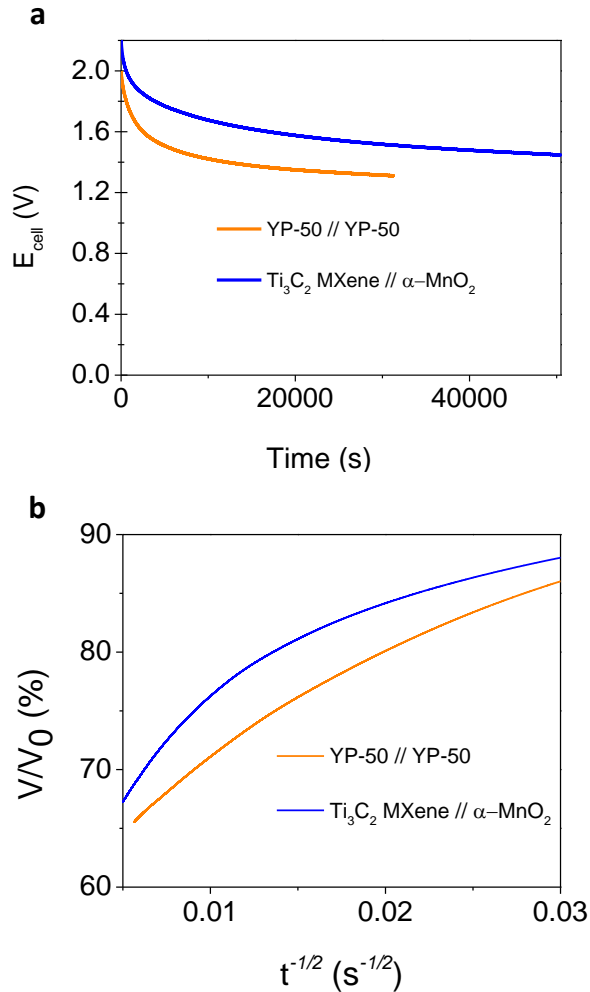


Figure 5.19. (a) Self-discharge characteristics: Voltage decay behavior at open circuit voltage of asymmetric cell of the electrochemical double layer capacitor, YP-50//YP-50, and asymmetric pseudocapacitor, Ti₃C₂//α-MnO₂. Cells were polarised at the maximum voltage for 2 h. **(b)** Shows the decay behaviour with the function of $t^{-1/2}$, where t represents the decay time in open circuit conditions. All the cells were charged to its maximum voltage with a current density of 10 mA g⁻¹.

when compared to that of classical aqueous electrolytes (Lukatskaya *et al.*, 2018).

Constraints in the redistribution of charges at the FSI with high viscous electrolytes. Such behavior has been recently reported with ionic liquids based electrolytes in carbon-based supercapacitors by (Mourad *et al.*, 2016; Laheäär, Arenillas and Béguin, 2018). As voltage also decays non-linearly with $t^{-1/2}$ for the $\text{Ti}_3\text{C}_2//\text{MnO}_2$ cell, it can be settled that a diffusion limitation also occurs in $\text{Ti}_3\text{C}_2//\text{MnO}_2$ cell. In terms of the voltage retention, in the initial 30,000 s of self-discharge, the $\text{Ti}_3\text{C}_2//\text{MnO}_2$ cell shows a voltage decay from 2.2 V to ~ 1.5 V. Whereas, in the YP-50//YP-50 cell, this voltage decays from 2.0 V to ~ 1.3 V. These voltage decays can be quantified to $\sim 68\%$ and 65% for $\text{Ti}_3\text{C}_2//\alpha\text{-MnO}_2$ and YP-50//YP-50 cell, respectively. Interestingly, in order to reach the analogous self-discharge of YP-50//YP-50 cell ($\sim 65\%$), the $\text{Ti}_3\text{C}_2//\alpha\text{-MnO}_2$ cell takes another 20,500 s. This tendency indicates a lower self-discharge for the $\text{Ti}_3\text{C}_2//\alpha\text{-MnO}_2$ cell, which also specifies an altered mechanism of charge storage in the configuration of $\text{Ti}_3\text{C}_2//\alpha\text{-MnO}_2$ cell, unlike known different ion sorption mechanisms for EDLCs, which is known occur at the FSI between porous carbon and electrolyte in EDLCs (Forse *et al.*, 2016).

Further understanding of this behavior is done by observing the potential decay of individual electrodes in the $\text{Ti}_3\text{C}_2//\alpha\text{-MnO}_2$ cell configuration. The results, as shown by **figure 5. 20 a**, designate that during the initial 10,000 s of self-discharge, the voltage decays of Ti_3C_2 is quicker than $\alpha\text{-MnO}_2$. Which, Later ($t > 10,000$ s) slows down and is lesser than that of $\alpha\text{-MnO}_2$. Though, diffusion limitation occurs in both electrodes, as shown with the non-linearly of voltage decay along $t^{-1/2}$ by **figure 5. 20 b**. This dissimilar voltage decay could be due to the altered charge re-distribution

mechanisms occurring in both electrodes. Though the phenomenon is still unclear at this stage of investigation and additional studies are required in this direction and therefore following is the proposed hypothesis to the uneven self-discharges between Ti_3C_2 and $\alpha\text{-MnO}_2$ electrodes in $\text{Ti}_3\text{C}_2//\alpha\text{-MnO}_2$ cell.

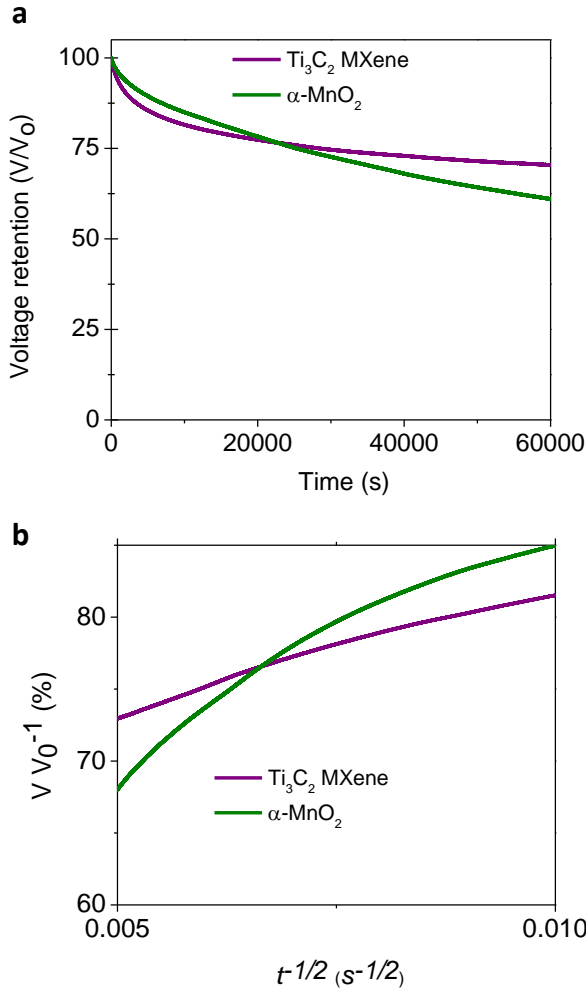


Figure 5. 20. (a) Potential decay behavior at an open circuit voltage of the Ti_3C_2 and $\alpha\text{-MnO}_2$ in the asymmetric cell configuration of $\text{Ti}_3\text{C}_2//\alpha\text{-MnO}_2$. The cell was polarised at the maximum voltage for 25 h. (b) shows the decay behaviour with the function of $t^{-1/2}$, where t represents the decay time in open circuit conditions.

Hypothesis: Based on the recent experiments, (Levi et al., 2015; Ren et al., 2018) showed the occurrence of faster electrolyte ion desorption from Ti_3C_2 surface sites, followed by slower desorption of trapped ion within the shallow adsorption sites of Ti_3C_2 Mxene. Therefore, it can be hypothesized that the difference of desorption rates at the surface and shallow sites allow Ti_3C_2 MXene to show a two-trend voltage decay during the self-discharge test. Whereas, recent experiments by (Byles et al., 2018) during the desalination process with $\alpha-MnO_2$, showed the fast ion removal capacity test of K^+ ions from the $\alpha-MnO_2$. Therefore, it can be hypothesized that the fast removal capacity of K^+ ions from the $\alpha-MnO_2$ could be the reason for high voltage decay in $\alpha-MnO_2$ during the self-discharge analysis.

5.5.3. Electrochemical stability tests

Long term cycling tests are performed to determine the stability of the $Ti_3C_2//\alpha-MnO_2$ cell. Galvanostatic charge and discharge at a current density of 1 A g^{-1} over cycling reveal the capacitance retention, which is shown in **figure 5. 21 a**. The observed capacitance retention of $\sim 96\%$ over 5,000 cycles is exceptional when compared with the existing reports in water-in-salt electrolytes (Gambou-Bosca and Bélanger, 2016),(Zhang et al., 2018). This cell is stable when compared with the existing Carbon- MnO_2 asymmetric cell based in fluorinated-imide water-in-salt electrolytes. In such cells, the rapid capacitance decays are observed within 5000 cycles (Gambou-Bosca and Bélanger, 2016),(Zhang et al., 2018) (**table 5. 3**).

Moreover, this asymmetric cell is even stable up to 10,000 cycles, where the value of capacitance retention $\sim 93\%$. Stability of the presented asymmetric supercapacitor is promising and is achieved thanks to the selection of safer operational limits *via* Voltage-Hold tests. Besides cycling, the columbic efficiency over cycling, as shown in **figure 5. 21 b**, varies between 99.5 to

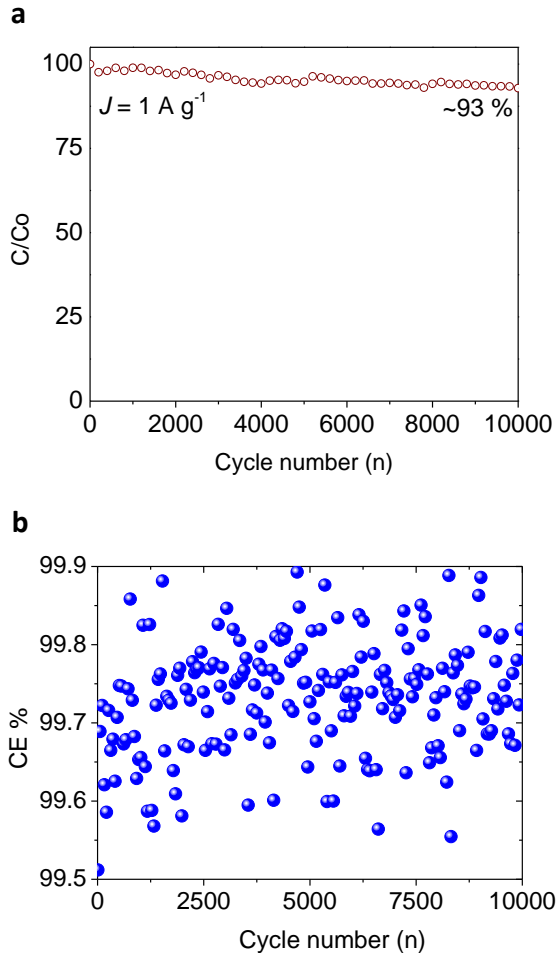


Figure 5. 21. Stability analysis of the asymmetric cell, $\text{Ti}_3\text{C}_2/\alpha\text{-MnO}_2$ (a) Long term galvanostatic charge discharge at 1 A g^{-1} . Current density applied is considered with respect to the mass of both electrodes. (b) Columbic efficiency during long term cycling.

99.9%. Such a narrow change in columbic efficiency indicates a good insertion and extraction capability of charges in the cell.

Cell type	Charging Mechanism (-)/(+)	Electrolyte salt ##	Capacitance Decay (Cycles)	Ref.
C-MnO ₂ *	EDLC /Pseudocapacitor	Li-TFSI	~ 50% (5,000)	(Gambou-Bosca and Bélanger, 2016)
Li-MnO ₂ **	Plating-deplating /Pseudocapacitor	Li-TFSI	< 25% (5,000)	(Zhang <i>et al.</i> , 2018)
Ti ₃ C ₂ - α -MnO ₂ #	Pseudocapacitive/ Pseudocapacitive	KoAc	~ 96% (5,000) ~ 92.94% (10,000)	Present work

Table 5. 3. Comparison of stability results of the present asymmetric cell with other hybrid-pseudocapacitors implied in a water-in-salt electrolyte.

***Black pearl carbon** (active material: 9.7 mg cm⁻²)/amorphous MnO₂ (active material: 2.9 mg cm⁻²).

** **Lithium** (unknown weight)/ **MnO₂** (active material: 200 μ g cm⁻²).

Ti₃C₂ (loading ~ 3.0 g cm⁻², ~ 10 μ m thick, density ~ 3.0 g cm⁻³) and **α -MnO₂** (loading ~ 9 mg cm⁻², density ~ 1.6 g cm⁻³, ~ 55 thick).

concentration : 21 m (mol kg⁻¹); Li-TFSI: Lithium bis(Trifluoromethane)-Sulfonimide; KoAc: Potassium Acetate

5.6. Conclusions

This chapter deals with problem-related to the low nominal cell voltages of aqueous pseudocapacitors. To tackle this issue, a high-voltage asymmetric cell is assembled with 2D Titanium Carbide MXene (a negative electrode)

and Manganese oxide (a positive electrode) in a water-in-salt electrolyte. A high-voltage of 2.2 V was achieved because of the wider scanning potential windows of both materials in potassium acetate based water-in-salt electrolytes, as water splitting reactions are shifted due to a high concentration of salt in the aqueous electrolyte. This is achieved by a step by step approach taken with the construction of the supercapacitor cell, which is described as following:

Selection of electrolyte concentration: Among three different concentrations of potassium acetate water-in-salt electrolytes; namely 21, 25 and 30 m. Two electrolyte concentrations were selected due to their analogous potentials for hydrogen evolution reactions. Electrochemical analysis of highly concentrated electrolyte solution (30 m) has shown a low cation insertion in 2-D Ti_3C_2 MXene interlayers compared to moderate electrolyte concentration (21 m). In effect, it is hypothesized and validated that Ti_3C_2 electrodes demonstrate a kinetic limitation for ions diffusion in highly concentrated electrolytes (30 m) over moderate electrolyte concentration (21 m). Therefore, 21 m of potassium acetate was selected as an electrolyte solution for evaluating the positive electrode.

Selection of tunnel MnO_2 polymorph: Several tunnel polymorphs are electrochemically evaluated in 21 m of potassium acetate based water-in-salt electrolyte. Electrochemical investigations of several tunnels phase of Manganese oxide, reveals that $\beta\text{-MnO}_2$ (1 x 1 tunnel) is unable to store a high amount of charge, as the radii of 1 x 1 tunnel (0.40 Å) is significantly smaller than the radii solvated ions of water-in-salt electrolyte (1.37 Å – 2.80 Å). While, Todorokite- MnO_2 phase where tunnels stabilized with larger cations (3 x 3 tunnels), create hindrance to the insertion of solvated cations. Both $\beta\text{-MnO}_2$ and Todorokite- MnO_2 exhibited low storage of charges. However, the charge storage performance was increased by a factor of 4 by

employing an intermediate tunnel phase of α - MnO_2 (2×2 tunnels) structure is used. Although further widening of the tunnels with Na- 2×4 MnO_2 phase (2×4 tunnels) enhances the values of charge storage. But lower electronic conductivity of Na- 2×4 MnO_2 phase over α - MnO_2 has led to higher charge decays at high rates (loss of charge at moderate to high cycling rate). Therefore, by considering the reasonable charge storage value and low rate decay of α - MnO_2 over other tunnel phases of MnO_2 (β - MnO_2 , Na- 2×4 MnO_2 , and Todorokite- MnO_2), α - MnO_2 was chosen as a potential candidate for the positive electrode.

Full cell: Thanks to the selection of water-in-salt electrolyte concentration (21 m), and polymorph of MnO_2 (α - MnO_2), an asymmetric cell of 2-D Ti_3C_2 and α - MnO_2 is assembled. Although electrochemical analysis of 2-D Ti_3C_2 and α - MnO_2 in three electrolyte cell configuration indicates a possibility of having 2.55 V as a nominal cell voltage for the Ti_3C_2 MXene and α - MnO_2 cell. Yet, the Voltage-Hold test indicates a stable operational limit up-to a voltage of 2.2 V. Because, it is shown that beyond the cell voltage of 2.2 V, α - MnO_2 initiates to extend the electrochemical potential windows, especially in the negative potentials, where it could form dissolvable Mn^{2+} species. Thanks to the selection of an appropriate cell voltage (2.2 V) via Voltage-Hold test, the 2-D Ti_3C_2 and α - MnO_2 cell shows high electrochemical stability over the existing water-in-salt electrolytes based hybrid-supercapacitors.

Besides this, it is proposed that the synergic effect of using conductive 2-D Ti_3C_2 Mxene and appropriate concentration of water-in-salt electrolyte (allowing higher charge storage kinetics) as well as the moderate tunnel size and electronically conducting phase of MnO_2 , allows not only a similar rate decay to that of carbon double layer capacitors, but also exhibits low

rate decays when compared to existing hybrid cells based on water-in-salt electrolytes.

Additionally, with analogous values in volumetric capacitances between activated carbon-based double layer capacitors and the 2-D Ti_3C_2 and $\alpha\text{-MnO}_2$ cell, the size of the Ti_3C_2 and $\alpha\text{-MnO}_2$ cell was condensed by a factor of 3. This remarkable behavior is achieved thanks to the higher packing densities of 2-D Ti_3C_2 and MnO_2 over activated carbon electrodes. Moreover, the non-double layer charge storage mechanisms in both electrodes (negative and positive) allows the 2-D Ti_3C_2 and $\alpha\text{-MnO}_2$ cell to exhibits slower discharges than activated carbon-based supercapacitors. This way, the configuration of 2-D Ti_3C_2 and $\alpha\text{-MnO}_2$ in water-in-salt electrolyte also resolves the important issue of quicker self-discharges in the field of aqueous electrochemical supercapacitors. The above-mentioned electrochemical properties of Ti_3C_2 and $\alpha\text{-MnO}_2$ cell are remarkable, thanks to this, the presented Ti_3C_2 and $\alpha\text{-MnO}_2$ cell in potassium acetate water-in-salt electrolyte is more favorable for the applications in which the volume and energy density (high voltage) are important and required.

5.7. References

Alhabeb, M. *et al.* (2017) 'Guidelines for Synthesis and Processing of Two-Dimensional Titanium Carbide ($\text{Ti}_3\text{C}_2\text{T}_x$ MXene)', *Chemistry of Materials*, 29(18), pp. 7633–7644. doi: 10.1021/acs.chemmater.7b02847.

Brousse, T., Bélanger, D. and Long, J. W. (2015) 'To Be or Not To Be Pseudocapacitive?', *Journal of The Electrochemical Society*, 162(5), pp. A5185–A5189. doi: 10.1149/2.0201505jes.

Byles, B. W. *et al.* (2016) 'The role of electronic and ionic conductivities in the rate performance of tunnel structured manganese oxides in Li-ion batteries', *APL Materials*. AIP Publishing LLC, 4(4), p. 046108. doi: 10.1063/1.4948272.

Byles, B. W. *et al.* (2018) 'Tunnel structured manganese oxide nanowires as redox active electrodes for hybrid capacitive deionization', *Nano Energy*. Elsevier Ltd, 44(June 2017), pp. 476–488. doi: 10.1016/j.nanoen.2017.12.015.

Byles, B. W. and Pomerantseva, E. (2016) 'Effect of manganese oxide crystal tunnel size on Li-ion and Na-ion battery performance', *Proc. of SPIE Vol.*, 9924, p. 992406. doi: 10.1117/12.2238638.

Demarconnay, L., Raymundo-Piñero, E. and Béguin, F. (2011) 'Adjustment of electrodes potential window in an asymmetric carbon/MnO₂ supercapacitor', *Journal of Power Sources*, 196(1), pp. 580–586. doi: 10.1016/j.jpowsour.2010.06.013.

Dou, Q. *et al.* (2018) 'Safe and high-rate supercapacitors based on an "acetonitrile/water in salt" hybrid electrolyte', *Energy and Environmental Science*. Royal Society of Chemistry, 11(11), pp. 3212–3219. doi: 10.1039/c8ee01040d.

Feng, X. *et al.* (2015) 'Transformation from phylломanganates to todorokite under various conditions: A review of implication for formation pathway of natural todorokite', in *ACS Symposium Series*, pp. 109–134. doi: 10.1021/bk-2015-1197.ch006.

Forse, A. C. *et al.* (2016) 'New perspectives on the charging mechanisms of supercapacitors', *Journal of the American Chemical Society*. American Chemical Society, 138(18), pp. 5731–5744. doi: 10.1021/jacs.6b02115.

Gambou-Bosca, A. and Bélanger, D. (2016) 'Electrochemical characterization of MnO₂-based composite in the presence of salt-in-water and water-in-salt electrolytes as electrode for electrochemical capacitors', *Journal of Power Sources*, 326, pp. 595–603. doi: 10.1016/j.jpowsour.2016.04.088.

Ghidiu, M. *et al.* (2015) 'Conductive two-dimensional titanium carbide "clay" with high volumetric capacitance', *Nature*. Nature Publishing Group, 516(7529), pp. 78–81. doi: 10.1038/nature13970.

Ghodbane, O., Pascal, J. L. and Favier, F. (2009) 'Microstructural effects on charge-storage properties in MnO₂-based electrochemical supercapacitors', *ACS Applied Materials and Interfaces*, 1(5), pp. 1130–1139. doi: 10.1021/am900094e.

Goubard-Bretesché, N. *et al.* (2016) 'Electrochemical study of aqueous asymmetric FeWO₄/MnO₂ supercapacitor', *Journal of Power Sources*, 326, pp. 695–701. doi: 10.1016/j.jpowsour.2016.04.075.

Haynes, W. M., Lide, D. R. and Bruno, T. J. (2018) *Handbook of Chemistry and Physics*. 93rd edn, *CRC Handbook of Chemistry and Physics*. 93rd edn. Edited by W. M. Haynes. Boca Raton: CRC Press. doi: 10.1201/9781315380476.

Laheäär, A., Arenillas, A. and Béguin, F. (2018) 'Change of self-discharge mechanism as a fast tool for estimating long-term stability of ionic liquid based supercapacitors', *Journal of Power Sources*. Elsevier, 396(February), pp. 220–229.

doi: 10.1016/j.jpowsour.2018.06.009.

Lannelongue, P. *et al.* (2018) “Water-in-Salt” for Supercapacitors: A Compromise between Voltage, Power Density, Energy Density and Stability’, *Journal of The Electrochemical Society*, 165(3), pp. A657–A663. doi: 10.1149/2.0951803jes.

Leonard, D. P. *et al.* (2018) ‘Water-in-Salt Electrolyte for Potassium-Ion Batteries’, *ACS Energy Letters*, 3(2), pp. 373–374. doi: 10.1021/acsenergylett.8b00009.

Levi, M. D. *et al.* (2015) ‘Solving the Capacitive Paradox of 2D MXene using Electrochemical Quartz-Crystal Admittance and In Situ Electronic Conductance Measurements’, pp. 1–11. doi: 10.1002/aenm.201400815.

Lukatskaya, M. R. *et al.* (2013) ‘Cation Intercalation and High Volumetric Capacitance of Two-Dimensional Titanium Carbide’, *Science*, 341(September), pp. 1502–1506. doi: 10.1126/science.1243494.

Lukatskaya, M. R. *et al.* (2018) ‘Concentrated Mixed Cation Acetate “Water-in-Salt” Solutions as Green and Low Cost High Voltage Electrolytes for Aqueous Batteries’, *Energy & Environmental Science*. doi: 10.1039/C8EE00833G.

Mourad, E. *et al.* (2016) ‘Biredox ionic liquids with solid-like redox density in the liquid state for high-energy supercapacitors’, *Nature Materials*. Nature Research. doi: 10.1038/nmat4808.

Naguib, M. *et al.* (2011) ‘Two-dimensional nanocrystals produced by exfoliation of Ti_3AlC_2 ’, *Advanced Materials*. 2011/08/24, 23(37), pp. 4248–4253. doi: 10.1002/adma.201102306.

Naguib, M. and Gogotsi, Y. (2015) ‘Synthesis of two-dimensional materials by selective extraction’, *Accounts of Chemical Research*, 48(1), pp. 128–135. doi: 10.1021/ar500346b.

Ren, C. E. *et al.* (2018) ‘Voltage Gated Ions Sieving Through 2D MXene $\text{Ti}_3\text{C}_2\text{Tx}$ Membranes’. doi: 10.1021/acsnm.8b00762.

Van Der Sluys, W. G. (2009) *The Solubility Rules: Why Are All Acetates Soluble?*, *Journal of Chemical Education*. doi: 10.1021/ed078p111.

Suo, L. *et al.* (2016) ‘Advanced High-Voltage Aqueous Lithium-Ion Battery Enabled by “Water-in-Bisalt” Electrolyte’, *Angewandte Chemie - International Edition*, 55(25), pp. 7136–7141. doi: 10.1002/anie.201602397.

Tian, Z. *et al.* (2017) ‘Superconcentrated aqueous electrolyte to enhance energy density for advanced supercapacitors’, *Functional Materials Letters*, 10(06), p. 1750081. doi: 10.1142/S1793604717500813.

Wang, F. *et al.* (2018) ‘Hybrid Aqueous/Non-aqueous Electrolyte for Safe and High-

Energy Li-Ion Batteries', *Joule*. Elsevier Inc., 2(5), pp. 927–937. doi: 10.1016/j.joule.2018.02.011.

Xie, Y. *et al.* (2014) 'Role of surface structure on Li-ion energy storage capacity of two-dimensional transition-metal carbides', *Journal of the American Chemical Society*, 136(17), pp. 6385–6394. doi: 10.1021/ja501520b.

Yao, W. *et al.* (2018) 'Energy-driven surface evolution in beta-MnO₂ structures', *Nano Research*. Tsinghua University Press, 11(1), pp. 206–215. doi: 10.1007/s12274-017-1620-5.

Young, M. J. *et al.* (2015) 'Charge storage in cation incorporated α -MnO₂', *Chemistry of Materials*, 27(4), pp. 1172–1180. doi: 10.1021/cm503544e.

Zhang, M. *et al.* (2018) 'High-performance hybrid supercapacitors enabled by protected lithium negative electrode and "water-in-salt" electrolyte', *Journal of Power Sources*. Elsevier, 396(April), pp. 498–505. doi: 10.1016/j.jpowsour.2018.06.037.

General conclusions

This thesis is devoted to enhance the electrochemical performances of supercapacitors. The development was addressed to storing more charges facilitating the response time and/or extending the cell voltages of the supercapacitors in the context of aqueous based electrolytes. This way, as the energy in a supercapacitor is proportional to its charge stored and voltage, the problem of its low energy densities can be tackled. Following is the briefing of the investigation can be summarized in three main blocks:

1. 3-D Fe/Fe₂O₃ porous carbon as electrodes materials for the high rate supercapacitors

Investigation of using Fe/Fe₂O₃ embedded in porous carbon nanofibers as supercapacitor electrodes reveals that the concentration of the metal precursor plays an important role

- i) in the capacitance value as the density of porous and its distribution is modified by the Fe concentration and the applied thermal process.
- ii) in the resistance value associated to the electrode as the carbon nanofibers have different conductivities according to the distribution of Fe/Fe₂O₃ nanoparticles embedded.
- iii) in the time response as the decay of charge during fast charging is dependent on the associated electrical resistance and capacitance values.

So, although increasing the concentration of the metal precursor improves the surface area related to the micropores region (pores < 2nm) and the ability of the resulting electrodes to store more charges, the fiber morphology and structure modification causes the carbon electrode to lose its electrical conductivity. Because of this, the electrodes fabricated with the high

concentration of the metal precursor diminish its capability to charge the carbon surface during the condition of fast charging, showing a longer response time constant in the charge decay. Consequently, while designing the supercapacitors based on metal/metal oxide embedded in porous 3-D carbon nanofibers, a trade-off between the metal precursor's concentration and its electrochemical performance needs to be taken under deliberation. Consideration of this tradeoff would help the community in designing EDLCs performing with better energy and power capabilities.

2. Electrochemical properties of 2-D molybdenum vanadium carbide MXene in various monovalent and a bivalent cation

The charge storage in 2-D molybdenum vanadium carbide MXene has the dependence on the type of electrolyte cations. For the case in point, small size monovalent cations, such as lithium and sodium ions, demonstrate lower hindrance to the charge storage, while large size monovalent potassium ions and bivalent magnesium ions suffer from hindrance effect, causing them to have lower charge storage than lithium and sodium ions. Therefore, the selection of appropriate electrolyte ions especially in the case of MXene based materials, appears to be important, which is here found to be with the protonic and sodium ion based electrolytes. Moreover, using these electrolytes to couple 2-D molybdenum vanadium carbide with other MXenes, like titanium carbide, has allowed to us to enable a reliable full MXenes based pseudocapacitor with high volumetric capacitances.

3. Building high-voltage aqueous pseudocapacitors using water-in-salt electrolytes

The use of super-concentrated solutions as an electrolyte media for the assembly of a cell composed of 2-D titanium carbide MXene and tunnel manganese oxide has been verified and assessed. It reveals that:

- The concentration of the salt electrolyte plays a significant role in the values of charge storage in 2-D titanium carbides. Although an extremely high concentration of salt electrolytes widens the potential window, the electrolyte ions in such high concentration face difficulty to insert within the 2-D layers of titanium carbide MXene. On the contrary, the use of low concentrated salt solutions is not recommended, as they provide narrow potential windows. Consequently, during the cell assembling using super-concentrated electrolytes, a moderate concentration of salt electrolyte needs to be taken into attention. On this way, both, wider potential window and high charge storage, can be achieved with pseudocapacitive materials like 2-D titanium carbides MXenes.
- The crystallographic tunnel size of manganese oxide plays a vital role in the charge storage. For instance, tunnel structures, both smaller and larger than the size of the electrolyte ions store fewer charges. As both of these tunnel phases of manganese oxide face difficulty for the insertion of the electrolyte ions. Therefore, manganese oxide with adequate tunnel size needs to be taken into account. Besides this, it is also essential to consider the electronic conductivity of the manganese oxide phase, as high electronic conductivity allows it to store more charges during the condition of fast charging.
- In regards of the cell assembly, after considering the above-mentioned understanding the practice of applying the voltage-hold test to determine the realistic cell voltage is helpful, as the cell assembled with such realistic voltages permits the cell to have long cycle life. Furthermore, the use of pseudocapacitors is more favorable than EDLCs in applications where cell volume is critical, as pseudocapacitors provide lower cell volume and slower self-discharges than EDLCs.

As a whole, supercapacitor technology developed in the laboratory through this thesis exhibits remarkable performances, such as:

- (i) the carbon-based EDLCs developed in chapter 3 exhibits a response time of 88 ms, which was lowest among the known 3-D carbon-based EDLCs.
- (ii) the pseudocapacitive cell developed in chapter 4 is the first exhibition of an all-MXene cell performing with high voltages of 1.3 V. This was previously limited to only 0.6 V with 2-D titanium carbide MXene based supercapacitors.
- (iii) the pseudocapacitive cell developed in chapter 5 operates in an aqueous electrolyte with a high voltage of 2.2 V. This cell voltage is in-fact closer to that of the organic electrolyte based supercapacitors (2.3 V).

Future Works

Though several strategies were employed to enhance the electrochemical performances of the supercapacitors in this thesis, there are still more works needs to be completed. Some of the challenges and their following works to further studies are:

1. **To extend the cell voltage of 3-D Fe/Fe₂O₃ porous carbon electrodes based supercapacitors based on carbon nanofibers.**

Although the supercapacitor cell composed of 3-D Fe/Fe₂O₃ porous carbon electrodes shows high-rate behavior, the assembled cell exhibits a cell voltage of 1 V. This cell voltage is still narrow when compared to that of the supercapacitor cells based on organic electrolytes. One strategy could be to deploy super-concentrated solutions as water-in-salt electrolytes, as water-in-salt electrolytes extend the nominal voltage of the supercapacitor cells (as shown in *chapter 5* of this thesis with Ti₃C₂//MnO₂ cell).

2. **To improve the volumetric capacitance of Ti₃C₂//MnO₂ cell based on aqueous based electrolyte**

Although the Ti₃C₂//MnO₂ cell shows a high voltage (2.2 V) close to that of the organic electrolyte based supercapacitors, their volumetric capacitance (15 F cm⁻³ at 50 mV s⁻¹, *chapter 5*) is still lower than that of Ti₃C₂//Mo_{2.7}V_{1.3}C₃ cell (> 35 F cm⁻³ at 50 mV s⁻¹, *chapter 4*). Further work in the direction of using new 2-D Mo_{2.7}V_{1.3}C₃ MXene (as shown in *chapter 4*) along with Ti₃C₂ MXene and as well as with the cell assembly strategy followed in *chapter 5* can be employed to build a pseudocapacitive cell. This way, both wider cell voltages and volumetric capacitances can be achieved.

3. To develop supercapacitor technology as energy storage integrated in fully autonomous systems.
4. To enhance the properties of supercapacitor using graphene and its hybrid materials.
5. To establish a protocol for the material production and processing for high volume production of the supercapacitors.
6. Formulation of new electrolytes containing redox species in order to increase the energy density values.
7. Design and fabrication of stacks cells.

A. Characterization of Fe precursor based carbon nanofibers

A.1. Selection of catalyst precursor

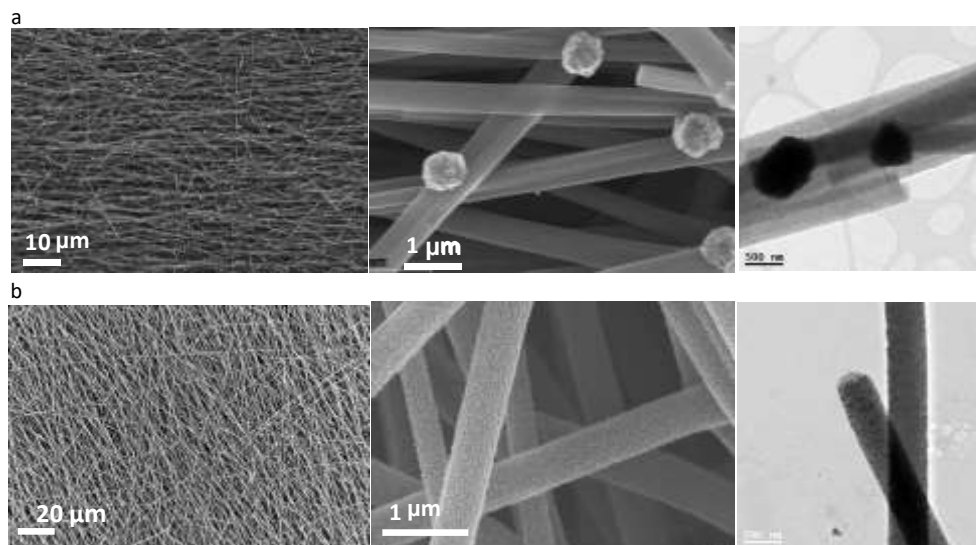


Figure A. 1: a, CNFs prepared with 4.7 wt.% iron chloride: left, Large scale and middle, small scale FE-SEM and right, HR-TEM images showing that non-homogenous distribution of oxide structures, which are formed as a consequence of coalescence small nanostructures to form large structures, when iron chloride was used as precursor. b, CNFs prepared with 4.7 wt. % iron acetylacetonate: left, Large scale and middle, small scale FE-SEM and right, HR-TEM images showing that homogenous distribution of oxide structures when iron acetylacetonate was used as a precursor.

Having non-homogeneous scattering or bulky nanostructures on the carbon nanofiber matrix, reduces the grain contact with carbon. This kind of decoration shows lower kinetics in carbothermal reduction (Hoekstra *et al.*, 2016), causing non-homogeneity towards catalytic graphitization and in turn textural properties of CNFs (Oya and Marsh, 1982). Therefore, homogenous distribution of nanostructures in CNFs is essential, which

could be influenced with type of precursor. Such identification is granted by selecting two commonly used precursor in the field of electrospinning (Avireddy, Morante and Flox, 2016; Hoekstra *et al.*, 2016; Zhang *et al.*, 2016), namely: (i) iron acetylacetonate and (ii) iron chloride. Both differs within their anion radical group, as $\text{CH}_3\text{COCHCOCH}_3^-$ and Cl^- , respectively. FE-SEM and TEM images of the CNFs prepared from Cl^- and $\text{CH}_3\text{COCHCOCH}_3^-$ radical containing precursor are shown by **Figure A.1.a** and **b**, respectively. Cl^- shows non-homogeneous distribution of bulk and nano-sized structures on carbon matrix. Whereas, $\text{CH}_3\text{COCHCOCH}_3^-$ shows homogeneity. This tendency is an effect of the iron chloride's property of being deliquescent and volatile, which causes migration of small iron species to bulky structures via Ostwald ripening (Hoekstra *et al.*, 2016). While, being less deliquescent and air stable iron acetylacetonate shows homogeneous distribution.

A.2. Selection of carbothermal atmosphere

Atmosphere of carbothermal reaction can also play an important role in the formation of pores and it is important to understand and select atmosphere. In this regards, two different atmospheres, inert (i.e. Ar) and reducing (i.e., Ar/H₂ (5 %)) are implied during carbonization. Following which, their textural properties are observed. FE-SEM image of carbon matrix carbonized in inert and reducing atmosphere is shown by **Figure A.2.a** and **b**, respectively. Carbon matrix in inert atmosphere show granular nanostructures with scarce concentration of large size porous pores. Whereas, reducing atmosphere shows a significant distribution of large porous. It is noteworthy that nanostructures are seen inside the pores. Whereas, no such pores are observed in the case of samples treated in inert atmosphere. Textural studies via BET specific surface area shows a three-

fold increase difference between reducing ($440 \text{ m}^2 \text{ g}^{-1}$) and inert atmosphere ($161 \text{ m}^2 \text{ g}^{-1}$). Besides, DFT pore volume and size distributions, as shown by **Figure A**, indicates higher differential pore volume in reducing atmosphere than inert. The trend of higher surface area, is related to the faster kinetics of carbothermal reduction in reducing atmosphere, as carbon reacts with hydrogen to form methane, which in turn, reduces iron oxide and forms CO/CO₂ (Dang *et al.*, 2013), causing further etching of carbon to form pores. Such textural features are significant to have more capacitance via sorption of electrolyte ions at the FSI (Dyatkin *et al.*, 2016; Forse *et al.*, 2016; Salanne *et al.*, 2016).

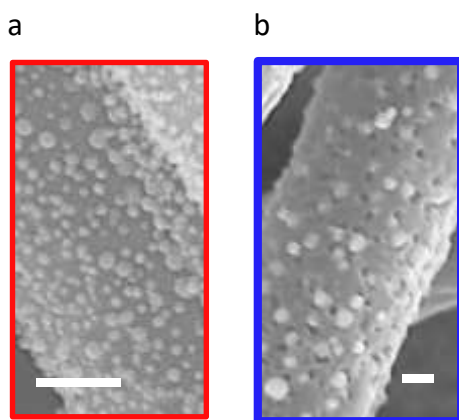


Figure A. 2 FE-SEM images of the carbon matrix in a, Ar (image, scale 100 nm) and b, Ar/H₂ (image, scale 100 nm).

A.3 Characterization of different concentrations of Fe precursor

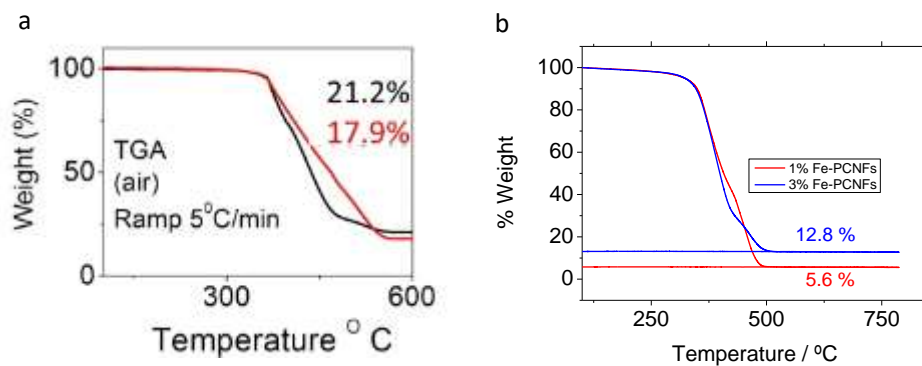


Figure A.3. TGA analysis showing the difference of iron oxide content in fibers **a**, 4.7 wt. % prepared by using iron chloride (shown by red color) and iron acetylacetonate (shown by black color). **b**, 1 wt. % and 3 wt. % of iron acetylacetonate.

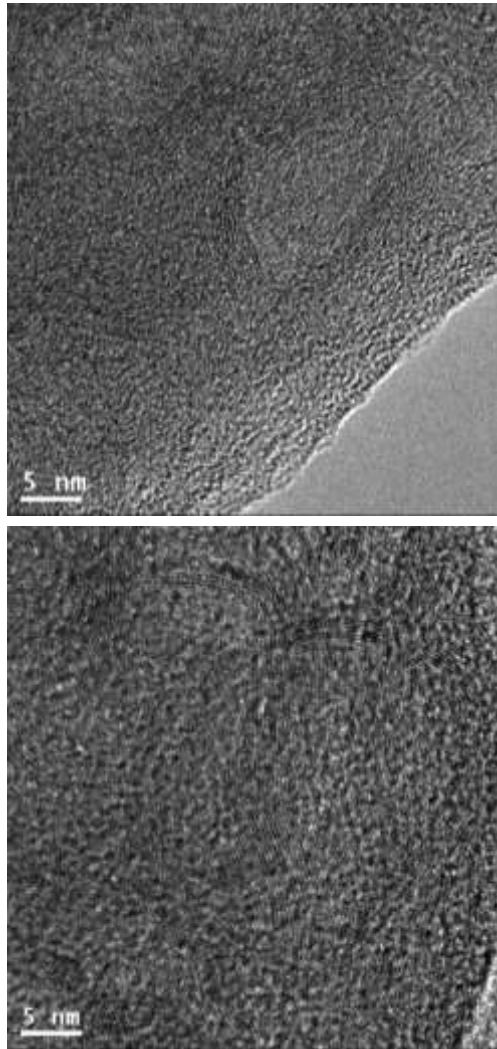


Figure A.4 HRTEM images showing the graphitic ordering in the carbon matrix at different locations when iron /iron oxide nanoparticles are present.

References:

- Avireddy, H., Morante, J. R. and Flox, C. (2016) 'A Perspective: Could Carbon Current Collectors Improve the Energy Density of Aqueous Alkaline Symmetric Supercapacitors?', *Energy Harvesting and Systems*, 3(4), pp. 1–10. doi: 10.1515/ehs-2016-0015.
- Dang, J. *et al.* (2013) 'Reduction kinetics of metal oxides by hydrogen', *Steel Research International*. WILEY-VCH Verlag, 84(6), pp. 526–533. doi: 10.1002/srin.201200242.
- Dyatkin, B. *et al.* (2016) 'Influence of Surface Oxidation on Ion Dynamics and Capacitance in Porous and Nonporous Carbon Electrodes', *Journal of Physical Chemistry C*. American Chemical Society, 120(16), pp. 8730–8741. doi: 10.1021/acs.jpcc.6b01204.
- Forse, A. C. *et al.* (2016) 'New perspectives on the charging mechanisms of supercapacitors', *Journal of the American Chemical Society*. American Chemical Society, 138(18), pp. 5731–5744. doi: 10.1021/jacs.6b02115.
- Hoekstra, J. *et al.* (2016) 'The effect of iron catalyzed graphitization on the textural properties of carbonized cellulose: Magnetically separable graphitic carbon bodies for catalysis and remediation', *Carbon*, 107, pp. 248–260. doi: 10.1016/j.carbon.2016.05.065.
- Oya, A. and Marsh, H. (1982) 'Phenomena of catalytic graphitization', *Journal of Materials Science*. Kluwer Academic Publishers, 17(2), pp. 309–322. doi: 10.1007/BF00591464.
- Salanne, M. *et al.* (2016) 'Efficient storage mechanisms for building better supercapacitors', *Nature Energy*. Nature Publishing Group, 1(6), p. 16070. doi: 10.1038/nenergy.2016.70.
- Zhang, B. *et al.* (2016) 'Recent advances in electrospun carbon nanofibers and their application in electrochemical energy storage', *Progress in Materials Science*. Elsevier Ltd, 76, pp. 319–380. doi: 10.1016/j.pmatsci.2015.08.002.

B. Material characterization of Na-2x4 MnO₂

B.1 Synthesis of Na-2x4 MnO₂

Na-2x4 nanowires were synthesized following a previous report (Shen *et al.*, 2005). First, Na-birnessite was synthesized by dropwise addition of a 50 mL solution containing 2.81 g Mn(Cl)₂·4H₂O into a 50 mL solution containing 0.79 g of KMnO₄ and 6.0 g of NaOH. The dropwise addition was performed in an ice bath. After mixing, the solution and precipitate were allowed to age under ambient conditions for 24 h. The precipitate (Na-birnessite) was then filtered out of solution and washed thoroughly until the pH dropped below 10 when the material was dispersed in 500 mL of DI water. The product was then dried at 100 °C for 12 h. 500 mg of the Na-birnessite and 11.5 mL of 1 M NaOH were added to a 23 mL Teflon-lined stainless steel autoclave and placed in an oven at 220 °C for 48 h. The final product (Na-2x4) was filtered, washed, and dried at 100 °C for 12 h.

B.2. Material characterization of Na-2x4 MnO₂

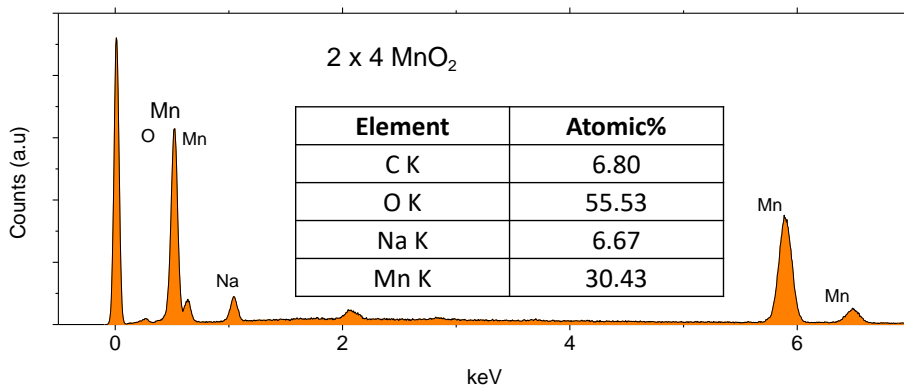


Figure B. 1. EDS spectrum of Na-2 x 4 MnO₂, showing a chemical formula of Na_{0.21}MnO_{2-x}

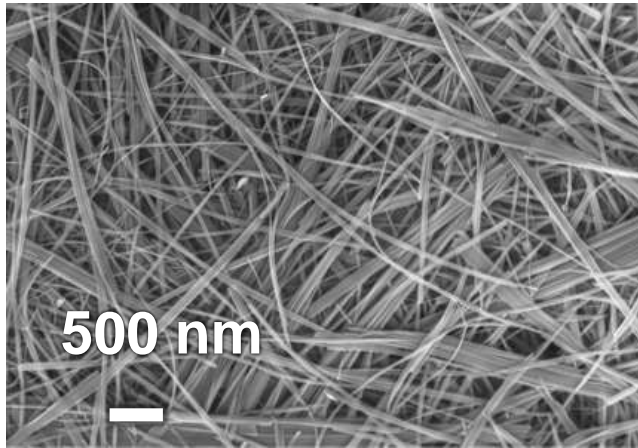


Figure B. 2. SEM images of $\text{Na-}2 \times 4 \text{ MnO}_2$, depicting a morphology of nanowires

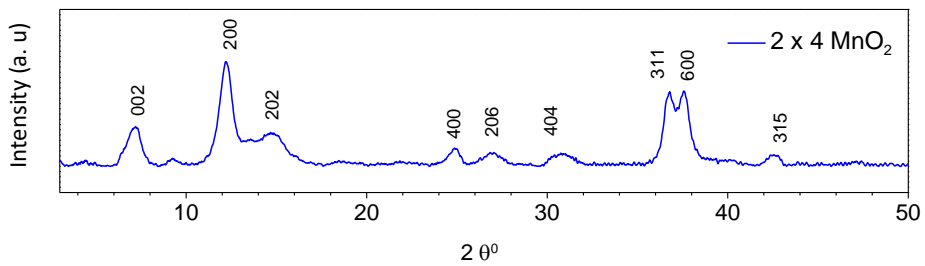


Figure B. 3. XRD pattern of $\text{Na-}2 \times 4 \text{ MnO}_2$

References

Shen, X. F. *et al.* (2005) 'Control of nanometer-scale tunnel sizes of porous manganese oxide octahedral molecular sieve nanomaterials', *Advanced Materials*. Wiley-Blackwell, 17(7), pp. 805–809. doi: 10.1002/adma.200401225.

C. Cyclic Voltammetry and long term studies cycling studies of 2-D Molybdenum Vanadium Carbide MXene

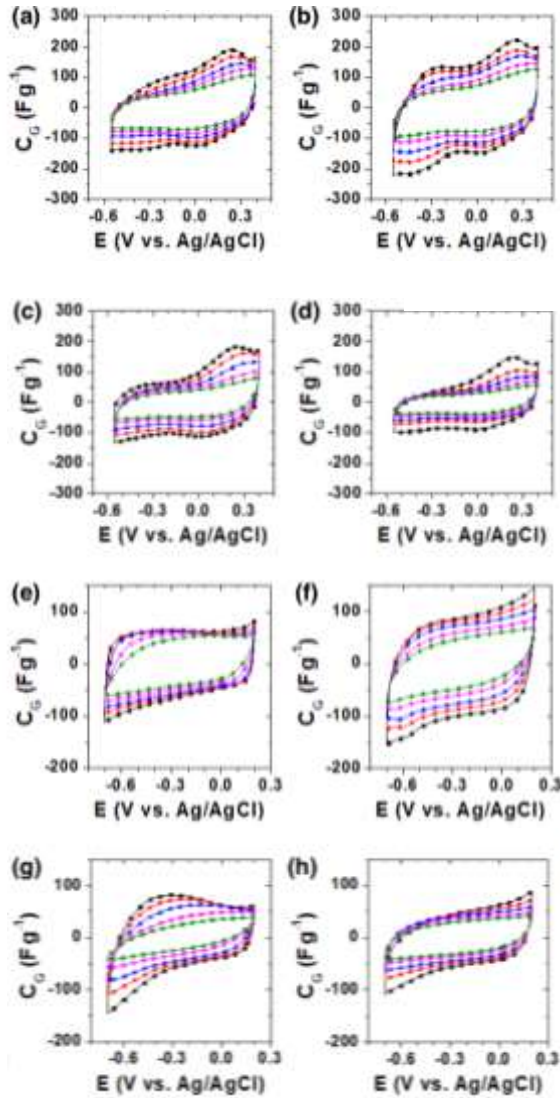


Figure C. 1. CV curves of $Mo_{2.7}V_{1.3}C_3$ MXene in a three electrode cell configuration in acidified (a) Li_2SO_4 , (c) Na_2SO_4 , (e) $MgSO_4$, (g) K_2SO_4 electrolytes with H_2SO_4 ($2.19 \leq pH \leq 2.36$), non-acidified (e) Li_2SO_4 , (f) Na_2SO_4 , (g) $MgSO_4$, (h) K_2SO_4 electrolytes and, (i) acidic $1\text{ M } H_2SO_4$ electrolytes. The scan rate were 5 mV s^{-1} (black squares), 10

$mV s^{-1}$ (red circles), $20 mV s^{-1}$ (blue triangles), $50 mV s^{-1}$ (pink reverse triangles) and $100 mV s^{-1}$ (green diamonds)

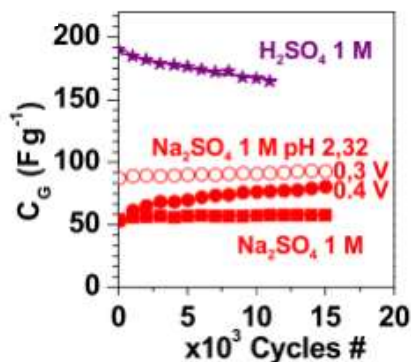


Figure C. 2. Long term cycling studies indicating the capacitance fade of $Mo_{2.7}V_{1.3}C_3$ MXene in a three electrode cell configuration. The electrolytes (with electrochemical windows): 1 M H_2SO_4 (between -0.4 and 0.4 V vs. Ag/AgCl), 1 M Na_2SO_4 (neutral pH between -0.7 and 0.2 V vs. Ag/AgCl) and, 1 M Na_2SO_4 (pH 2.32 between -0.5 V and 0.3 V or 0.4 V vs. Ag/AgCl). All the cycling studies were carried out at a current density of $3 A g^{-1}$.

Figure 2.2 indicates that the $Mo_{2.7}V_{1.3}C_3$ MXene have low capacitance fade in non- and acidified sodium sulfate-based electrolytes. Whereas, in acidic electrolytes such as 1 M H_2SO_4 system slight capacitance fade (90 %). Previously, (Rahman and Skyllas-Kazacos, 1998) suggested that structure forming vanadium oxide and vanadyl species are soluble in solution with low pH value. Considering this and the low pH value of 1 M H_2SO_4 (0-0.1), we hypothesize that the vanadium species might dissolve over cycling in 1 M H_2SO_4 , because of this high capacitance fade was observed in 1 M H_2SO_4 , when compared to non- and acidified sodium sulfate-based electrolytes.

References

Rahman, F. and Skyllas-Kazacos, M. (1998) 'Solubility of vanadyl sulfate in concentrated sulfuric acid solutions', *Journal of Power Sources*, 72(2), pp. 105–110. doi: 10.1016/S0378-7753(97)02692-X.

Hemesh Avireddy

Nationality : Indian

D.O.B : 15th Nov, 1992 (26 years)

Address: IREC, Jardins de les dones de Negre 1
08930 Sant Adrià del Besos, Barcelona, Spain

Mobile : (+34) 602674947

E-mail : ahemesh@irec.cat

Interests	R&D and Technology Transfer (Energy storage devices - Supercapacitors and Batteries; Nanosensors)
Education	Ph.D , Nanosciences and Nanotechnology [March, 2016 – Present] Faculty of Physics, University of Barcelona, Spain <i>Thesis Title</i> – Enhancing electrochemical performances of supercapacitors <i>Supervisors</i> – Dr. Cristina Flox and Prof. Joan Ramon Morante Associate Ph.D , Business Innovation (InnoEnergy) [March, 2017 – Present] European Institute of Innovation & Technology (EIT)- European Union, Budapest (Hungary) <i>Courses</i> Energy Economics 3 ECTS, Grenoble School of Management (France) [2017] Innovation Bootcamp on [2018] Entrepreneurship 5 ECTS, Eindhoven University of Technology (Netherlands) Communication in Teamwork and Leadership 3 ECTS, AGH University of Science and Technology (Poland) [2019] ICGM- AIME – CNRS – UMR 5253, Université Montpellier , France [Jan – July, 2015] Joint Master Thesis - Pole Balard Total foundation Scholarship [CGPA: 10.0/10.0] <i>Thesis Title</i> – Development of nanocomposite electrode materials for supercapacitors based on reduced-graphene oxide/metal-oxide <i>Supervisors</i> – External - Prof. Patrice Simon and Dr. Frédéric Favier

SASTRA University, Thanjavur, India [July, 2010 – Aug, 2015]
Master in Technology - Power Systems (Integrated 5-Years)
[GPA: 7.44/10.0]

Publications

Hemesh Avireddy, Bryan Byles, David Pinto, Xuehang Wang, Cristina Flox, Oliver Crosnier, Jordi Jacas Biendicho, Thierry Brousse, Ekaterina Pomerantseva, Joan Ramon Morante, Yury Gogotsi, Stable high-voltage pseudocapacitive energy storage with low self-discharges (*under submission for Journal of Power Sources*)

David Pinto, Babak Anasori, Hemesh Avireddy, Christopher Shuck, Kanit Hantanasirisakul, Joan Ramon Morante, William Porzio⁴, Husam N. Alshareef, Yury Gogotsi, Molybdenum Vanadium Carbide, a New Tailorable Double Transition Metal MXene for Electrochemical Applications (*Under submission for Journal of Materials Chemistry A*)

Hemesh Avireddy, Cristina Flox, PengYi Tang, Jordi Jacas Biendicho, Jordi Arbiol, Joan Ramon Morante, Role of Fe precursor concentration in axially controlled 3-D electrospun Fe/Fe₂O₃ carbon nanofibers as high-rate supercapacitor electrodes (*Under submission for ACS Applied Energy Materials*)

Hemesh Avireddy, Bryan Byles, David Pinto, Xuehang Wang, Cristina Flox, Oliver Crosnier, Jordi Jacas Biendicho, Thierry Brousse, Ekaterina Pomerantseva, Joan Ramon Morante, Yury Gogotsi, Correlating tunnels structure and electrochemical properties of MnO₂ in water-in-salt electrolyte for high-rate charge storage (*in progress*)

Jordi Jacas Biendicho, Hemesh Avireddy, Cristina Flox, PengYi Tang, Jordi Arbiol, Joan Ramon Morante, New sulphur phase with solid-phase transformation for Li-S batteries (*In progress*)

Jordi Jacas Biendicho, Victor Izquierdo, Hemesh Avireddy, Cristina Flox and Joan Ramon Morante, Limitations of Semi-Solid Flow

Batteries; Degradation and Cation Mixing in Vulcan-based Slurry with $\text{LiNi}_{1/3}\text{Co}_{1/3}\text{Mn}_{1/3}\text{O}_2$ as redox-active material (*In progress*)

Hemesh Avireddy, Harikishan Kannan, Prabakaran Shankar, Ganesh Kumar Mani, and John B B Rayappan, “Non-mutually exclusive dual role of hexamethylenetetramine on the growth of ZnO nanostructures and their sensing footprints” *Materials Chemistry and Physics*, 212 (2018) 394-402

Hemesh Avireddy, Cristina Flox, Joan Ramon Morante, “A Perspective: Could Carbon Current Collectors Improve the Energy Density of Aqueous Alkaline Symmetric Supercapacitors? Energy Harvesting and Systems, 3 (2016) 287–296.

Invited Talk “Electrospinning as Nanoengineering tool for energy storage devices” Materials Day Conference, Polytech-University of Montpellier, France (Feb, 2017)

Oral Presentations Hemesh Avireddy, Bryan Byles, Babak Anasori, Javier Vazquez Galvan, David Pinto, Jose Miguel Delgado Galindo, Xuehang Wang, Cristina Flox, Oliver Crosnier, Jordi Jacas Biendicho, Thierry Brousse, Ekaterina Pomerantseva, Yury Gogotsi, Joan Ramon Morante, High volumetric electrochemical energy storage for autonomous IOT devices, EMRS spring meeting 2019.

Hemesh Avireddy, Bryan Byles, David Pinto, Jose Miguel Delgado Galindo, Xuehang Wang, Cristina Flox, Oliver Crosnier, Jordi Jacas Biendicho, Thierry Brousse, Ekaterina Pomerantseva, Joan Ramon Morante, Yury Gogotsi, Stable high-voltage pseudocapacitive energy storage with low self-discharges. International Symposium on Enhanced Electrochemical Capacitors (ISEECap), Nantes (May, 2019).

Hemesh Avireddy, Cristina Flox, PengYi Tang, Jordi Arbiol, Joan Ramon Morante,” Nanoengineered electrodes for ultra-high charge-discharge supercapacitors (>8 V/s)”, Spring 2017 meeting, European Material Research Society, France.

Hemesh Avireddy, Cristina Flox, PengYi Tang, Jordi Arbiol, Joan Ramon Morante,” Rational tailoring of Fe/Fe₂O₃ incorporated porous CNFs electrodes towards ultra-high charge-discharge behavior”, Spring 2017 meeting, European Material Research Society, France.

Jordi Jacas Biendicho, Cristina Flox, hemesh Avireddy, Joan Ramon Morante,” Nanoengineering carbon cathodes for Lithium Sulphur batteries”Lithium Sulfur: Mechanisms, Modelling & Materials, London, 2017

Hemesh Avireddy, Cristina Flox, Joan Ramon Morante,”Active material incorporated electrospun porous carbon nanofibers as electrodes for supercapacitors” ELEN 2016: Electrospinning for energy conference. Montpellier, France.

Hemesh Avireddy, Cristina Flox, Joan Ramon Morante,” Electrospun metal doped CNFs as supercapacitor electrodes: From electrode fabrication to application to prototype cell” Spring 2016 meeting, European Material Research Society, Lille, France.

Research Experience

Pre-Doctoral Researcher, IREC, Barcelona (Spain)

[Sept, 2015 – Present]

Electrospun carbon nanofibers and their hybrids for supercapacitors (Metal Oxides/CNFs) New carbon slurries for flow supercapacitors (from prototype to stack application) Electrospun carbon nanofibers for Li-S batteries

Visiting Researcher, Drexel University, Philadelphia (USA)

[Feb – May, 2018]

Supervisor: Prof. Yury Gogotsi

Pseudocapacitive 2-D metal carbides based MXenes

Visiting Researcher, IMN (UMR CNRS 6502) Polytech Nantes (France)

[May – June, 2017]

Supervisors: Dr. Olivier Crosnier Prof. Thierry Brousse

- Pseudocapacitive metal tungsten oxides, High voltage Na-ion capacitors
Visiting Research Scholar, ICGM-CNRS, Montpellier (France) [June – July, 2014]
Supervisors - Prof. Patrice Simon and Dr. Frédéric Favier
- Nanocarbon/Metal-oxides as Electrode Materials for Supercapacitors & Batteries New and effective electrode fabrication techniques
Science Academies' Summer Research Fellow[#], CSIR-NCL, Pune (India) [April – May, 2014]
Supervisor - Dr. Sarika M Bhattacharyya
- Molecular Dynamics Simulations of Graphene Polyaniline Materials
Graduate Student Researcher, CeNTAB, SASTRA University (India) [Jan – March, 2014]
Supervisor - Dr. Suresh Kumar P
- Electrochemical Synthesis of Graphene using different Surfactants for Supercapacitors
Graduate Student Researcher, CeNTAB, SASTRA University (India) [Sept – Nov, 2013]
Supervisors - Prof. R. John Bosco Balaguru
- Solution Grown ZnO Nanorods -Effect of Molar Concentration Synthesis and Analysis of Graphene oxide for Room Temperature Gas Nanosensors
Science Academies' Summer Research Fellow[#], IISER, Pune (India) [May – July 2013]
Supervisors - Prof. Sulabha K Kulkarni
- Synthesis and Analysis of Graphene Encapsulated Hollow SnO₂ Nanoparticles
 Synthesis and Analysis of Graphene Encapsulated Hollow Cu₂O Nanoparticles

EU/National Funded projects (Participation)	HELIS: High energy lithium sulphur cells and batteries INFLIUNCE: FP7- Interfaces of Fluid Electrodes: New Conceptual Explorations eCUB: Emmagatzematge eficient d'energia –ACCIÓ	
Scholarships Fellowships/ Grants (Selected)	InnoEnergy Mobility Grant- 6000 € Best Poster Award- EMRS 2017- European Materials Research Society and International Society of Electrochemistry Young Scientist Award - European Materials Research Society Best Poster Award – ELEN 2016 - International Society of Electrochemistry Pole Balard Total foundation – Masters Trainee Scholarship Prestigious Indian Science Academies' Summer Research Fellowship Desh-Videsh Scholarship – Semester Abroad Program Prestigious Indian Science Academies' Summer Research Fellowship Consecutive Merit Scholarships by Army Welfare Education Society (AWES) Awards in student symposiums: International Symposiums – 7 National Symposiums – 22	[2018] [2017] [2016] [2016] [2015] [2014] [2014] [2013] [2010 -12]
Positions of Responsibility	<i>Organizing Committee Member, EMRS spring meeting</i> <i>Local Organising Committee Member, 4th International Symposium on Enhanced Electrochemical Capacitors (ISEECap), Montpellier, France</i> <i>Chair - IEEE Student Professional Awareness Conference, SASTRA University</i> <i>Chair, IEEE SASTRA University Student Branch</i>	2016 2015 2014 2013-14

Vice - Chair, Electra, Association of Electrical and
Electronics Engineering, SASTRA

2012-13

Memberships ISE-Battery Division (2017-present), ISE (2016-Present), EMRS
(2016-present), Bat-flu Network (2016-present), IEEE-(2013-2016) .

References Available on request